Cuffless Blood Pressure Measurement: Comparison and Validation Study of the Arterial Waveforms

Ghalib Muhammad Waqas Janjua

M.Sc. (Electrical Engineering)

B.E. (Electrical Engineering)

School of Engineering

Ulster University

Thesis submitted for the Degree of Doctor of Philosophy

December 2020

I confirm that the word count for this thesis is less than 100,000 words

Dedication

An effort to understand and admire the creator’s (Allah the Almighty) creation…

and

In dedication of my love for my family.

Acknowledgement

In the name of Allah, the Almighty, who is the most beneficent and the most merciful.

I would like to thank my supervisor, Prof. Jim McLaughlin, for his advice, encouragement, discussion, endless support, and great companionship. I would also like to thank Prof. Dewar Finlay, Dr Atta-ul-Haq, and my colleagues at the university, for their help, support, and guidance.

I would like to thank my family and friends for their love and prayers and for making this joyous journey memorable. I would like to thank all of the subjects who volunteered for the data collection portion of this research.

I would like to thank the funding agency, European Union's Horizon 2020 Research, and Innovation Programme, under the Marie Skłodowska-Curie grant, for this amazing research opportunity, and all the consortium partners.

Summary

Hypertension is a silent killer, and one-third of its sufferers are unaware of its presence. Earlier hypertension detection can control cardiovascular morbidity and mortality, and interventions associated with changes in daily lifestyle can cure this disease. The non-invasive assessment of arterial stiffness has great significance for the monitoring of hypertension and related cardiovascular diseases (CVDs). However, the accuracy of current non-invasive assessments is usually poor due to the imprecise sensing of arterial waveforms. This study investigated non-invasive arterial stiffness assessment methods, using a piezoelectric sensor [ballistic pulse pressure (BPP)], compared with the use of the current state-of-the-art sensor, the photoplethysmogram (PPG) sensor, and further validated the BPP sensor against existing gold-standard devices and techniques.

In this study, the viability of a low-cost alternative to tonometric devices was demonstrated, using a BPP sensor that was validated against the current gold-standard tonometric device, with an r^2 value of *0.86*. The BPP sensor does not require an operator and is a wearable, low-cost sensor that can accurately assess arterial stiffness, and these advantages are discussed, in detail. Furthermore, this study demonstrated the trackability and responsiveness of BPP arterial waveforms compared with electrocardiogram (ECG) waveforms, using the heart rate variability (HRV) technique. The surrogacy of the BPP waveforms for ECG waveforms was also established when using the HRV technique, with an r^2 value of *0.97*. Another significant contribution of this study was the improvement of the pulse transit time (PTT) technique, which is conventionally used during cuffless blood pressure (BP) measurements. PTT measurements based on in-line BPP sensors were found to be more consistent for tracking fiducial parameters than current state-of-the-art in-line PPG sensors.

Finally, the combination of both the BPP and PPG arterial waveforms resulted in the development of a novel, single-location estimation of arterial stiffness. The co-location of PPG and BPP sensors generated a pressure-volume loop, and the outcomes were reinforced by the phase-lag estimation between waveforms. This study was validated against the SphygmoCor carotid augmentation index, with an r^2 value of *0.71,* which may advance modern technology for the early detection of CVD.

Publications

1- G. M. W. Janjua, D. D. Finlay, D. Guldenring, A. U. Haq and J. A. D. Mclaughlin, "A Low-Cost Tonometer Alternative: A Comparison Between Photoplethysmogram and Finger Ballistocardiogram and Validation Against Tonometric Waveform," in IEEE Access, vol. 7, pp. 142787-142795, 2019, doi: 10.1109/ACCESS.2019.2944212.

2- G. M. W. Janjua, D. D. Finlay, D. Guldenring and J. A. D. McLaughlin, “Independent measurement of high blood pressure changes in cuff-less blood pressure monitoring,” in Journal of Electrocardiology, vol 50, Issue 6, pp 866, 2017, https://doi.org/10.1016/j.jelectrocard.2017.08.063.

3- G. M. W. Janjua, R. Hadia, D. Guldenring, D. D. Finlay and J. A. D. McLaughlin, “Heartrate Variability Comparison Between Electrocardiogram, Photoplethysmogram and Ballistic Pulse Waveforms at Fiducial Points,” in Precision Medicine Powered by pHealth and Connected Health, ICBHI, IFMBE Proceedings, vol 66, 2018. https://doi.org/10.1007/978-981-10-7419-6_29.

4- G. M. W. Janjua, D. D. Finlay, D. Guldenring, R. Hadia and J. A. D. McLaughlin, "Novel non-invasive pressure-volume loop measurement for local pulse wave velocity estimation," Computing in Cardiology (CinC), pp. 1-4, 2017, doi: 10.22489/CinC.2017.217-385.

5- G. M. W. Janjua, D. Guldenring, D. D. Finlay and J. A. D. McLaughlin, "Wireless chest wearable vital sign monitoring platform for hypertension," 39th Annual International Conference of the IEEE Engineering in Medicine and Biology Society (EMBC), Seogwipo, 2017, pp. 821-824, 2017, doi: 10.1109/EMBC.2017.8036950.

Abbreviations

AAMI	American Association for the Advancement of Medical Instrumentation
AI	Aging index
AIx	Augmentation index
APG	Accelerated plethysmogram
AS	Arterial Stiffness
AT	Applanation tonometry
B2BI	Beat-to-beat intervals
BCG	Ballistocardiogram
BHS	British Hypertension Society
BP	Blood pressure
BPP	Ballistic pulse pressure
BPP_1D	BPP first derivative peak
BPP_2D	BPP second derivative peak
BPP_P	BPP Peak
C&F	Carotid and femoral
CVD	Cardiovascular diseases
DRI	Dicrotic reflection index
DBP	Diastolic blood pressure
DUT	Device under test
ECG	Electrocardiogram
EEI	Cardiac ejection elasticity index

EHS	European Hypertension society
EI	Elasticity index
HF	High frequency
HR	Heartrate
HRV	Heart rate variability
JNC	Joint National Committee
LA	Left Atrium
LF	Low frequency
LV	Left ventricle
LV	Left ventricle
MAP	Mean arterial pressure
mmHg	Millimetre mercury
PAT	Pulse arrival time
PEP	Pre-ejection period
PPG	Photoplethysmogram
PPG_1D	PPG first derivative peak
PPG_2D	PPG second derivative peak
PPG_P	PPG Peak
PSD	Power spectral density
PTT	Pulse transit time
PU-Loop	Pressure volume loop
PVDF	Polyvinylidene fluoride
PWV	Pulse wave velocity
RA	Right atrium

RI	Reflection index
RV	Right Ventricle
SBP	Systolic blood pressure
SD1	Poincaré plot standard deviation perpendicular the line of identity
SD2	Poincaré plot standard deviation along the line of identity
SI	Stiffness index
SPH	Tonometric waveform using SphygmoCor device
ULF	Ultra-low frequency
VLF	Very low frequency
WHO	World Health Organization
WK	Windkessel
WKA	Weighted Kappa analysis

Table of Contents

List of Figures

List of Tables

Chapter 1

Introduction and Background to Arterial Waveform Analysis

1.1 Motivation and Background

Hypertension, which describes persistently elevated blood pressure (BP), is a curable, silent killer and has been reported to have a prevalence of 1.13 billion people, worldwide [1]. One-third of hypertension sufferers are unaware of their condition. Over the last two decades, arterial stiffness has emerged as an indicator of hypertension progression and cardiovascular disease (CVD) [2]. The European Society of Hypertension, in 2007, documented the importance of assessing arterial stiffness, which can be measured non-invasively [3]. The early detection of hypertension can control cardiovascular morbidity and mortality, and interventions, such as minor changes in daily lifestyle, can cure hypertension without requiring further medical interventions, like prescribed medications [4]. Arterial stiffness results in hypertension and CVD and can be measured non-invasively. The primary sources and associated signals used for the non-invasive assessment of arterial stiffness are as follows.

- Arterial volumetric flow waveform
- Arterial distension waveform
- Arterial pressure waveform

These signals can be clinically measured, using either invasive sensors or sophisticated non-invasive sensors, which are often limited by high costs and the lack of operational accuracy. These waveforms have been extensively researched for their use during the assessment of arterial stiffness [5][6]; however, currently, no clinically approved method is available.

Arterial waveforms can be captured using various methodologies and the data corresponding to each method have different properties and provide different information, depending on the nature of the sensor assessment. The

photoplethysmogram (PPG) uses optical technology to obtain a volumetric blood flow waveform, based on light absorption by blood cells [7] and is commonly deployed in wearable technology for fitness tracking applications. Ultrasound devices can be used to measure the distension waveform, which describes arterial wall movement due to blood flow, particularly for larger arteries, such as the carotid and femoral arteries [8]. Tonometer devices, such as SphygmoCor and Compilor, can be used to measure pulse pressure, by partially occluding arterial blood flow [9].

Although many studies have examined the non-invasive assessment of arterial stiffness during the last two decades, no method has been established that is cheap, user friendly, and can be used in wearable settings to provide data with clinical prognostic value. Although many previous studies have shown promising results for the non-invasive assessment of arterial stiffness, many methods lack performance accuracy. The current study describes a non-invasive and wearable solution for arterial stiffness measurements that can be used in clinical settings and home environments, with acceptable accuracies.

The research gaps are as follows**:**

1. Heart rate variability (HRV) has not been tested and compared for distention waveforms and electrocardiogram (ECG) R-peaks.
2. Arterial waveform analysis has not been compared, for arterial indexes, between distension waveforms and PPG-sensing technology.
3. The pulse transit time (PTT) has not been compared across different sensing methodologies, such as arterial volumetric flow and arterial distension waveforms.
4. The relationship between the arterial pressure waveform and the arterial volumetric flow waveform has not been evaluated in aspect waveforms data fusion.

1.2 Aims and Objectives

The primary aims of this study are to investigate non-invasive, arterial-stiffness-assessment methods, by comparing the use of a piezoelectric sensor with the currently utilised state-of-the-art sensor, PPG, and to validate the piezoelectric sensor

against the tonometric gold standard, to evaluate the clinical feasibility of utilising this new sensor to monitor arterial stiffness.

The main objectives of this work are listed below, based on the methodology used to compare the non-invasive sensor with the current state-of-the-art sensor and to validate the non-invasive sensor against the gold standards.

- To test and validate the trackability of the arterial waveforms measured by the sensor, with respect to HRV of gold standard ECG sensor.
- To test and validate the spatial and temporal haemodynamic indexes of arterial waveforms of gold standard tonometric sensor.
- To compare the fiducial point of the arterial waveforms, for the analysis of PTT.

Methodological comparisons and validations raise the question of whether information from various sensors can be combined (fused) to obtain additional information. Therefore, the last objective of the research was established:

- To measure pulse wave velocity (PWV) and phase lag, from the fusion between arterial waveforms and their quantisation, against the SphygmoCor sensor.

Background of Principles, Techniques, and Devices for Blood Pressure Measurement

1.3 Hypertension

Hypertension is a silent killer and represents the most significant challenge to public health, worldwide [1]. Hypertension morbidity increased dramatically, from 600 million to 1 billion patients, between 1980 and 2008; almost 40% of adults older than 25 years have been diagnosed with hypertension, worldwide, in 2008, according to the World Health Organization (WHO), 1 in 5 adults were hypertensive, and complications associated with hypertension cause 9.4 million deaths each year [1], which represents 55.3% of all CVD deaths. A significant number of impediments identified in CVD are caused by hypertension. The most common complications include myocardial infarction, stroke, renal failure, and death, particularity if hypertension is not diagnosed and treated correctly [2]. The Joint National Committee (JNC), in its 8th edition, reported over 30% of hypertension-afflicted patients are unaware of their affliction and 40% of hypertensive patients do not receive proper treatment for their conditions [3].

The force exerted by blood against the arterial walls during beat-to-beat blood flow is referred to as BP and is measured in units of millimetres of mercury (mmHg). The maximum pressure exerted during heart contraction referred to as systolic BP (SBP), whereas the minimum pressure exerted when the heart is at rest is referred to as diastolic BP (DBP). An example of a BP waveform is shown in Figure 1.1.

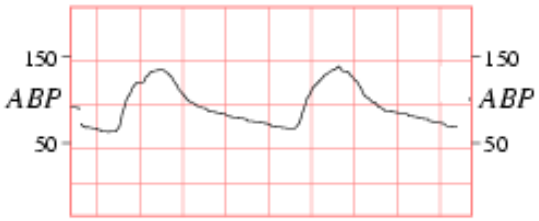

Figure 1.1: Representative Blood Pressure Waveform [10]

Hypertension, or high BP, is a stressed arterial condition, during which the blood flow waveform exerts persistently high pressure against the vessel walls. In healthy adults, the average SBP value is 120 mmHg and the average DBP value is 80 mmHg. The hypertensive condition increases health risks, especially for the heart and blood vessels in the kidney and brain.

Current non-invasive BP measurement devices/systems are limited to systems that intermittently record snapshot BP measurements. Using these devices, measurements are not only burdensome but are also insufficient to evaluate dynamic parameters, which are vital for CVD treatment. The hypertension classifications are shown in Table 1.1.

Table 1.1: Hypertension categories [11]

Systolic (mmHg)		**Diastolic (mmHg)**	**Categories**
Below 120	And	Below 80	Normal Blood Pressure
120–139	OR	80–89	Prehypertension
140–159	OR	90–99	Stage 1 hypertension
160 or more	OR	100 or more	Stage 2 hypertension

1.4 AAMI, BHS, and IEEE BP Device Standards

The American Association for the Advancement of Medical Instrumentation (AAMI) standard states that a BP monitoring device under test (DUT) must not differ from the mercury standard by a mean difference > 5 mmHg or a standard deviation > 8 mmHg relative to a calibration device. The British Hypertension Society (BHS) standards for BP monitoring DUTs are given in Table 1.2.

The Institute of Electrical and Electronics Engineers (IEEE) Std 1708-2014 is an IEEE Standard (under development) for wearable, cuff-less BP measuring devices, in compliance with the AAMI [12], BHS, and European Society for Hypertension (ESH) standards for DUT, as shown in Figure 1.2.

Table 1.2: BHS classification level for BP Monitors [13]

	The absolute difference between DUT and Standard Device (%)		
Grade	≤ 5	≤ 10	≤ 15
A	60	85	95
B	50	75	90
C	40	65	80
D	Worse than C		

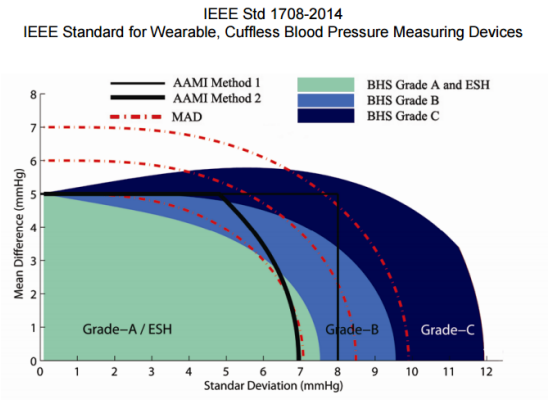

Figure 1.2: IEEE Std 1708-2014 [14]

1.5 Arterial Stiffness

Arterial stiffness is a predominant factor in CVD and PWV analysis can provide great insight into CVD-related conditions [15]. Arterial stiffness in hypertensive patients [16], [17] results in higher SBP and lower DBP, which can eventually cause an increase in the left ventricle (LV) afterload and alter coronary perfusion [18]. Radial SBP and pulse pressure becomes higher than the pressure in the ascending aorta due to pulse wave reflection [19], and central pressure is strongly related to vascular diseases [20]. Circadian rhythms and the BP cycle in response to sleep show BP variability of BP during the 24-h BP profile in daily life. BP tends to increase during the day, compared with that at night [21]. PWV is the gold-standard measurement for arterial stiffness, and a typical PWV value among healthy individuals is 7.6 m/s [22]. A PWV value of 12 m/s is a fixed threshold for hypertension diagnosis, as stated in the 2007 ESH/European Society for Cardiology (ESC) hypertension guidelines [23][24].

1.6 Invasive Systems

1.6.1 Gold Standard: Invasive BP Measurements - Arterial Line

The arterial line is the most accurate and continuous BP measurement method [17]. This technique has been practised since the early 19th century and continues to be considered the gold standard for BP measurements. A thin catheter is inserted into an artery, which can be the radial, carotid, femoral, dorsal pedal, or brachial artery, attached to a cannula needle, with an electronic pressure transducer that is connected to a fluid fill system that interfaces with a computer to calculate the BP waveform [25]. An arterial line can measure BP continuously, but its use is limited to the intensive care unit because of the delicate nature of its operation. A representative system is shown in Figure 1.3.

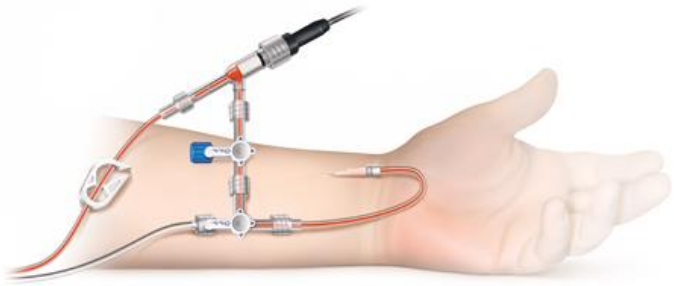

Figure 1.3: Arterial Line [26]

1.7 Non-invasive System

1.7.1 Snapshot Non-invasive Measurements

Various methods can be used to measure BP from the brachial artery, by observing sounds during the forced closure of the artery, mediated by a cuff, followed by the controlled release of blood flow to normal conditions.

1.7.1.1 Sphygmomanometer

The sphygmomanometer method is an ancient method that was introduced during the last quarter of the 17th century. Since then, it has evolved to take different forms and shapes and relies on counterpressure measurements. At the time of its invention, a fluid-filled chamber was sealed around the wrist and submerged into a container. BP produced pressure changes in the chamber, which could be measured. Later, a waterfilled bag was attached to a mercury manometer and pressed against the wrist, to observe the arterial pulsation. SBP could be determined when sufficient pressure was exerted on the bag to halt the arterial pulsation in the hand. The hydraulic system, such as the Gibson apparatus shown in Figure 1.4, was subsequently replaced with a pneumatic pressure system, which was the predecessor of the cuff-based system that is currently used in clinical practice.

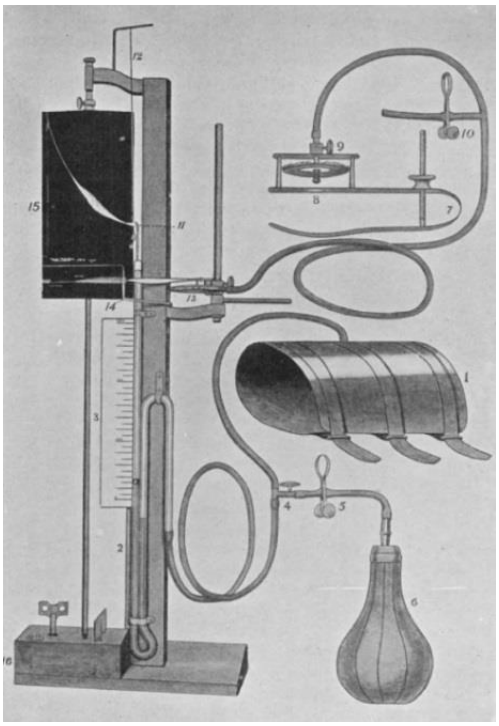

Figure 1.4: Gibson BP measurement apparatus [27]

1.7.1.2 Auscultatory Method

An auscultatory method is the most widely used method for measuring BP in the current clinical environment. At the start of the 19th century, Nikolai Korotkoff presented the measurement of BP in animals, using the Riva-Rocci sleeve, a manometer, and a stethoscope. This technique utilised an inflatable rubber cuff, which was strapped to the left arm, on the upper side. The device worked on collapse and controlled the release of blood flow in the brachial artery under the control of a pressurised hand pump cuff, as shown in Figure 1.5. The pump is connected to a mercury-filled scaled column or mechanical manometer, to measure the corresponding pressure. The cuff pressure is raised to stop the blood flow and then is gradually deflated, in a controlled manner, so that accompanying sounds of "beating" can be heard through a stethoscope placed onto the brachial artery by an observer, as shown in Figure 1.6. The first "beating" sound corresponds to SBP, and the pressure at which the "beating" stops indicates the DBP [28]. It is the easiest and the most efficient method to measure BP in clinics and the home environment.

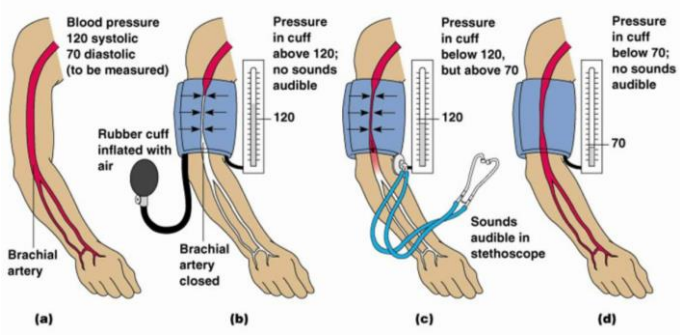

Figure 1.5: Sphygmomanometer [29]

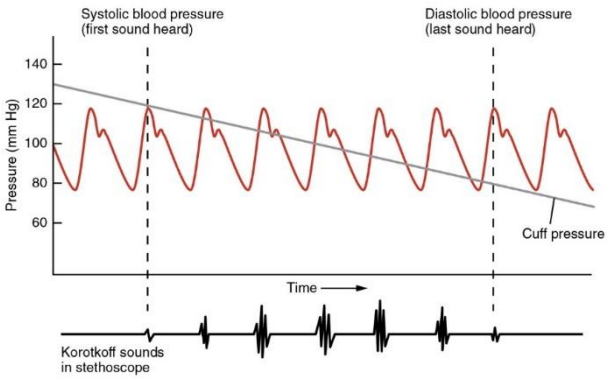

Figure 1.6: Korotkoff sounds observed during the controlled release of cuff pressure [29]

1.7.1.3 Oscillometric

An oscillometric BP monitoring device uses an electronic pressure transducer, an automatic/semi-automatic cuff inflation and deflation system, and a controlled valve connected to an LCD screen to display the measured values. These devices remove the necessity of an observer during measurements. The cuff is strapped onto the left arm at the brachial artery, with the subject in the seated or supine position. Oscillometric BP monitors use the same principals as the auscultatory sphygmomanometer, but the cuff inflates using an electronic pump, to a pressure above SBP, and then deflates below DBP, through controlled release. The pneumatic values measure the mean arterial pressure (MAP), with the aid of an electronic transducer. A representative device is shown in Figure 1.7. An algorithm is used to make indirect measurements of SBP and DBP, as shown in Figure 1.8. Oscillometric devices that can be worn on the wrist are placed at the radial artery, which must be elevated to the heart level, although measurements taken at the upper arm tend to have higher accuracy. When oscillometric devices are compared against auscultatory devices using the AAMI standard a bias of 5 mmHg were found and oscillometric are prone to error in subjects with arterial stiffness, atrial fibrillation, and pre-eclampsia [30].

Figure 1.7: Oscillometer device [31]

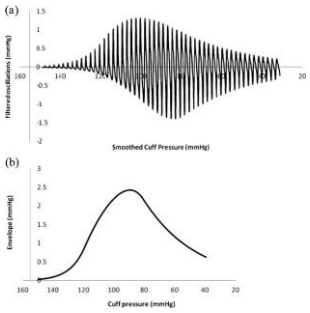

Figure 1.8: BP measurement under the oscillometric principle [32]

1.8 Supervised, Cuffless Non-invasive Continuous BP Measurement

1.8.1 Arterial Tonometry

In 1862, Von Graefe developed the indentation tonometer, to measure the pressure of the eyeball, and, in 1867, his pupil, Weber, developed the applanation tonometer [10]. The principle of the Goldmann applanation tonometry states that when an artery is flattened against the bone through force, the internal pressure becomes equal to the externally applied pressure [11].

Tonometric devices use a manometer-tipped probe (pressure sensor) to measure the BP flow waveform, by flattening the artery against the bone. Tonometric devices follow the Laplace transformation principal, which states that when a circular tube, such as an artery, is flattened, so that radius increases to infinity, the internal pressure becomes the external pressure. The most suitable location for this measurement is the radial artery, which provides precise and reproducible waveform results. The radial artery applanation tonometry (AT) algorithm was established by the Food and Drug Administration of the USA [33].

In the clinical environment, devices such as the sphygmomanometer and oscillometer utilise the peak and trough of the arterial waveform to assess CVD. To better assess the arterial waveform, an arterial tonometer can be used. When the carotid to radial transfer function is applied to the radial AT, the central BP can be determined. Central BP has been demonstrated to be a better predictor of CVD then to radial BP [34]. Representative, commercially available systems are shown in Figures 1.9 and 1.10.

Figure 1.9: SphygmoCor tonometer [35]

Figure 1.10: TL300 by Tensys medicals tonometer [36]

1.8.2 Ambulatory Systems

1.8.2.1 Volume Clamp Method

Volume clamps use a pressurised optical cuff that wraps around the index finger. The pressure of the cuff varies, based on PPG waveforms, to maintain a constant optical sensor signal, which provides feedback for pressure uniformity. Because the blood volume and the light signal remain constant over time, the intra-arterial pressure is equal to the cuff pressure. VERIFI or PhysioCal algorithms are used to calculate BP. However, this non-invasive technology is sensitive to changes in vascular tone caused by the vasodilation and vasoconstriction of the smooth muscles of minor arteries, starting from arteria radialis moving to the periphery. In addition, the conventional cuff-based oscillometric device continuously calibrates the device [37].

Penaz et. al. [38] developed a method for measuring the PPG waveform under a controlled cuff pressure, can remove motion-related artefacts. The pressure wave is frequently calibrated by cuff BP devices [39]. Two commercially popular devices are shown in Figures 1.11 and 1.12.

Figure 1.11: CNAP Monitor 500 by cnsystems [40]

Figure 1.12: Finapres Nova by Finapres [41]

1.8.2.2 Ambulatory Arm Cuff-based BP Monitor

In the clinical environment, especially in an intensive care unit, frequent BP measurements are necessary. Programmable devices are often used to measure the BP, based on the oscillometer principle. These devices can measure BP, with a minimum gap of 5 minutes, and generate a report for a 24-36-hour period. These machines can be accompanied by other diagnostic devices, such as ECG monitors and oximeters, as shown in Figure 1.13. The form factors of these BP monitors depend on their intended use, and some are built into wearable devices designed to measure hypertension and observe circadian rhythm, such as the device is shown in Figure 1.13.

Figure 1.13: (Left) Bedside ambulatory BP monitor [42] and (Right) Wearable BP monitor [43]

1.9 Cuffless Blood Pressure Systems

Various systems have been developed to measure BP without the use of a cuff, and researchers have shown great interest in this area since 2000. These devices aim to measure arterial stiffness, which can be used to estimate BP. Enormous research efforts and device development have occurred, with a few examples provided in Figures 1.14 to 1.18. The measurement principles for these devices are discussed in later sections. The use of these devices is limited because they lack the necessary precision and accuracy to meet the standards for BP measurements.

Figure 1.14: Scanadu Scout [44]

Figure 1.15: SOMNOtouch [46]

Figure 1.16: Visi Mobile [45]

Figure 1.17: BPro [47]

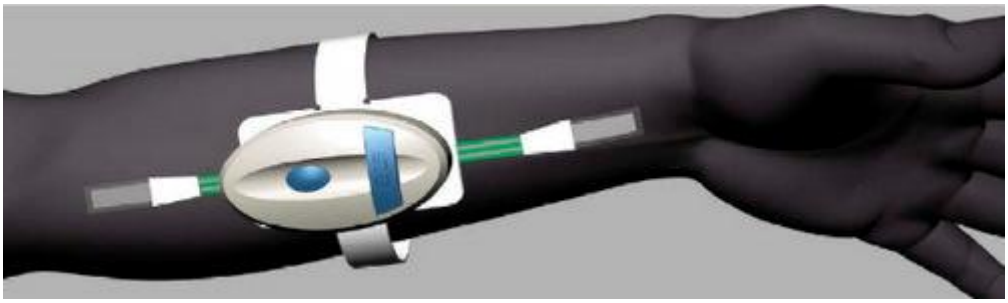

Figure 1.18: PWV device Intelesens [48]

1.10 Review of Cuffless BP Techniques

1.10.1 Pulse Arrival Time

During the pulse arrival time (PAT) technique, the proximal signal is captured using an ECG sensor, and the distal signal is captured using a PPG sensor, which can be placed on the index finger, forehead, ear, or carotid artery. PAT refers to the time difference between the ECG R-Peak and the PPG foot, or systolic peak, or peak of first derivative or second derivative, as shown in Figure 1.19. PAT is a combination of the PTT and the pre-ejection period (PEP) [49]. The PEP is determined based on the electromechanical heart delay and isovolumic contraction period [50], where the PEP represents 10%-35% of the PTT [50]. BP estimations based on PAT are not precise because of the additional PEP delay, as demonstrated in clinical trials [51] - [74]. PAT is the most desirable parameter because it is an easy to obtain and robust measurement. PAT correlates more closely with SBP then with DBP [75]. SBP has been demonstrated to have a higher range than DBP during exertion-type interventions. In an invasive study, PAT was less correlated with SBP then DBP [49][76].

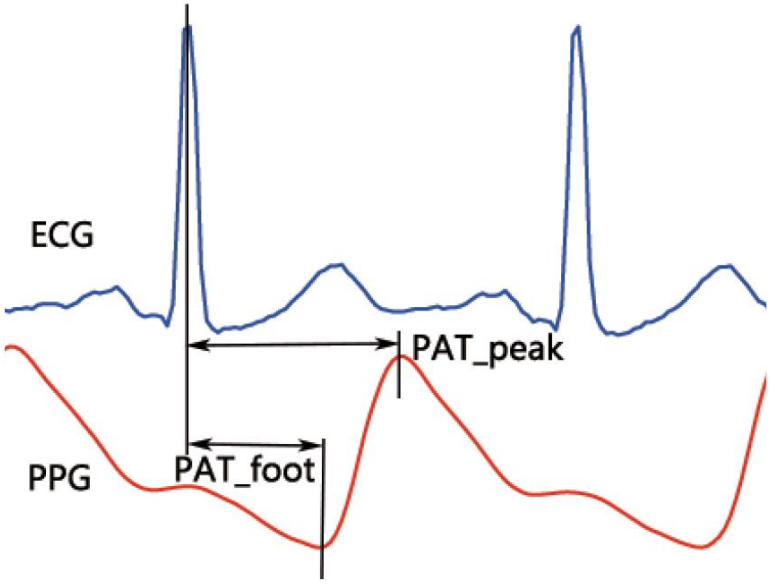

Figure 1.19: PAT measurement, based on ECG and PPG [77]

1.10.2 PPG Sensor with an Accelerometer[78]

Researchers have combined a PPG sensor with an accelerometer, approximating BP using a non-invasive, wearable, PPG sensor ring, worn on the finger. The accelerometer measures hydrostatic pressure variations when strapped to the upper arm, on the left side. The Wiener model-based relationship between transmural pressure and the PPG waveform was able to extract arterial pressure from optical estimated waveforms [79].

1.10.3 Pulse Transit Time (PTT)

PTT refers to the time difference between the proximal and distal waveforms. For this technique, two inline PPG sensors are placed on an artery to capture the proximal and distal waveforms, as shown in Figure 1.20. The fiducial points (the foot, systolic peak, the peaks of the first and second derivative, and intersecting tangents) are measured for each pulse waveform, and their time differences provide the PTT. Averaging PTT values over multiple cardiac cycles can reduce physiological artefacts [80][81]. Other important locations for measuring volumetric blood pulses include the radial artery, at the wrist and on the little finger (which target the ulnar and digital arteries, respectively), and height sensors are used to counteract hydrostatic pressure effects, shown in Figure 1.21. PTT is a ubiquitous technique with the potential to estimate BP [54], [59], [62]-[72], [82]–[92], . PTT can be used to produce dynamic BP waveforms [93][94].

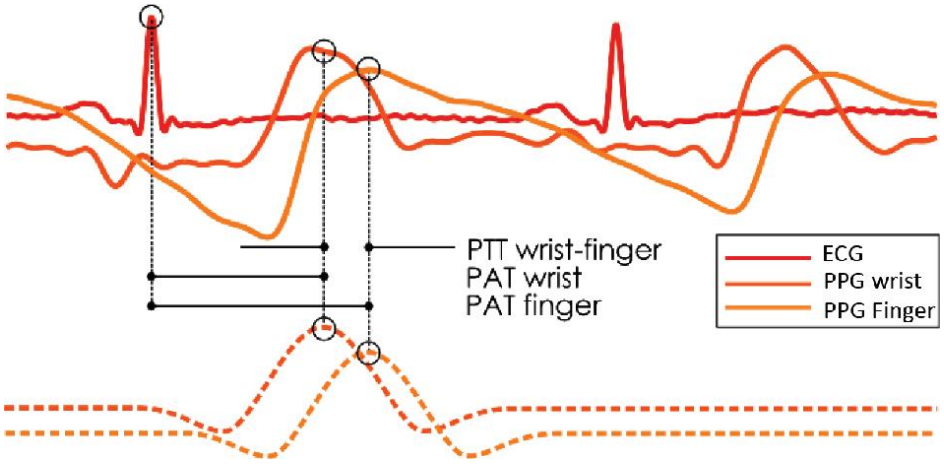

Figure 1.20: PTT between two PPG sensors [95]

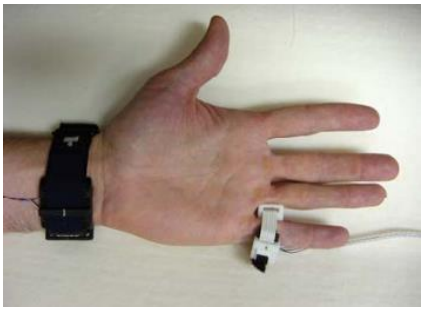

Figure 1.21: Inline PPG sensor, measuring PTT [28]

1.10.4 Pulse Wave Velocity (PWV)

The PWV measures the elasticity (or stiffness) of an artery, based on pressure waveforms. PWV-based arterial stiffness assessments can provide valuable information regarding CVD diseases [96]. PWV is measured as the ratio between distance of measurement location on an artery and PTT, which is mathematically represented as follows:

$$PWV = \left(\frac{\Delta x}{PTT}\right) \tag{1.1}$$

The PWV can be regional and local, depending on the measurement method. The regional method combines two similar sensors that can be located either inline or on two different branches of an arterial tree. Local PWV is measured by sensing pressure and flow arterial waveforms at the same location and is conventionally used by invasive sensors [97]. PWV can also be measured non-invasively, using an ultrasound sensor [8].

1.11 Evolution of Pulse Wave Velocity for BP Measurements and Limitations

The relationship between PWV and BP has been investigated by researchers over the last two decades, and promising evidence has indicated the existence of a direct relationship between these variables. However, two major problems have been identified with the use of PWV to estimate BP. First, PWV estimates can be inaccurate when using non-invasive sensors because of differences in the waveform origins, which can differ between the two measurement sites. Empirical calibrations and generalised transfer functions are often used to translate PWV measurements into BP estimates. Second, PWV varies with age, height, and ethnicity in normotensive

patients. Various techniques have been used to measure arterial stiffness, and their relationships with BP are described below.

1.11.1 Inline Sensors

For wearable applications, two surface-contact, polyvinylidene difluoride (PVDF) piezoelectric sensors are placed on the forearm, to measure arterial PTT from the brachial to the radial arteries, based on the pressure waveform, as shown in Figure 1.22.

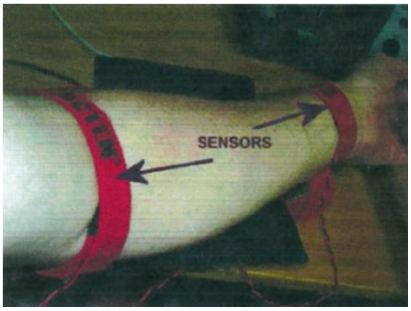

Figure 1.22: PVDF sensor for PTT measurements [48]

1.11.2 Carotid to Femoral PWV

The conventional measurement technique uses a tonometric device, combined with a cuff. The cuff is strapped to the thigh on the subject's femoral artery, and the tonometric sensor is placed on the carotid artery, as shown in Figure 1.23. The simultaneous acquisition of arterial waveforms provides the PWV, and the carotid to femoral length is calculated. The same procedure can be used without the cuff, by gating two waveforms taken at two different intervals at the carotid and femoral arteries. Aortic proximal and distal waveforms are predictors of cardiovascular risks [98].

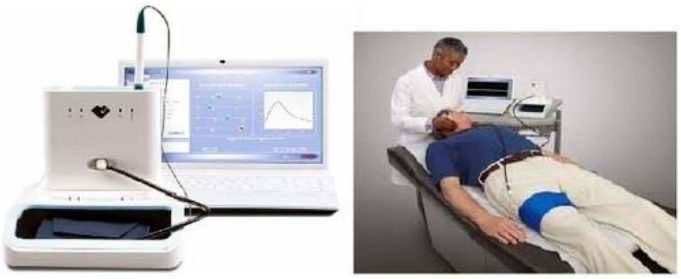

Figure 1.23: The operation of the AtCor PWV measurement system [35]

1.12 PTT Measurements by Eliminating PEP from PAT

A researcher developed a technique for obtaining PTT measurements by eliminating the PEP from the PAT, using an ear-anchored device to measure integrated physiological signals, including the ballistocardiogram (BCG), PPG, and ECG. The BCG was estimated by an accelerometer sensor in the ear. A single-lead ECG was recorded using one electrode on the back of the neck, with a reference electrode at the mastoid, on the back of the ear. Reflectance PPG was acquired on the back of the ear. The sensory device was wirelessly connected to a PC, where the MAP showed a linear relationship to ln(1/PTT) [99]. A similar system used a weight scale to measure BCG signals, which was used to remove the PEP from the PAT [100], and the obtained signals are shown in Figure 1.24.

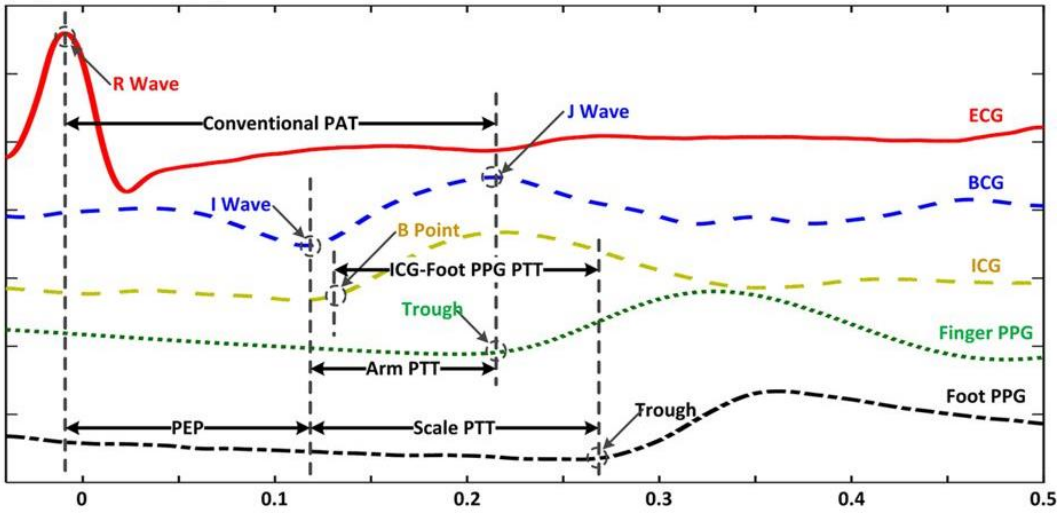

Figure 1.24: Using BCG and PPG to measure PTT [100]

1.13 Pulse Wave Analysis

The pulse wave analysis can provide valuable diagnostic information regarding artery stiffness, based on contour properties. The contour properties can be determined using the forward and reflected waves of a standing wave in the arterial tress, which varies significantly according to artery elasticity. The types of arterial indexes can be based on spatial and/or temporal fiducial locations on the pulse contour. These arterial indexes can be measured using the arterial second derivative, as shown in Figure 1.25.

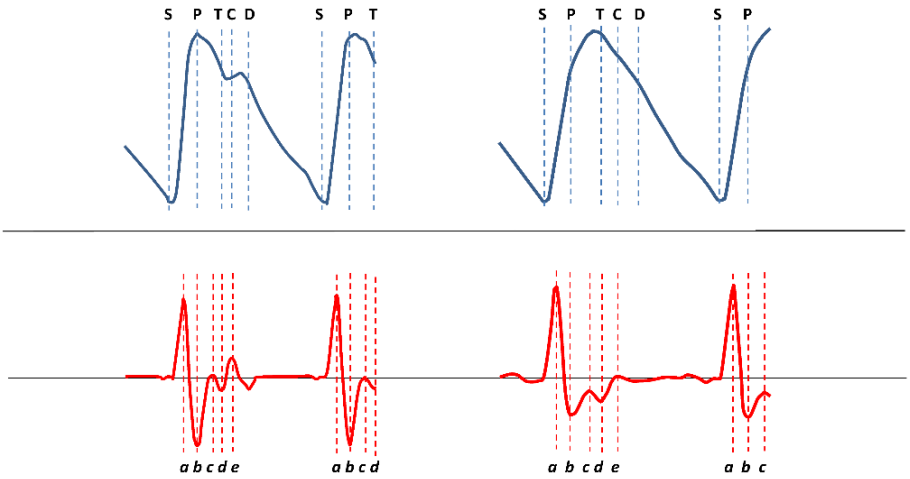

Figure 1.25: Digital plethysmogram (blue) and accelerated plethysmogram (red) [101]

The most significant arterial indexes include the stiffness index (SI), reflection index (RI), aging index (AI), augmentation index (AIx), elasticity index (EI), cardiac ejection elasticity index (EEI), and dicrotic reflection index (DRI) [101]. The functional parameters of these arterial provide information regarding arterial stiffness. The arterial waveform systolic amplitude is directly proportional to local vascular distensibility [102] and correlates with SBP estimates [103]. The pulse width provides a direct relationship to vascular resistance [104]. The ratio of the area under the curve at the dicrotic notch is an indicator of peripheral resistance [105].

1.14 Pressure-volume Loops

1.14.1 Invasive Measurement

PWV measurements that use the transit time of two pressure waves measure the average velocity, rather than the local PWV, due to the different compositions of arterial sites. For example, the aortic PWV measurement technique is a weighted average of wave speeds, as wave at the carotid artery spends less time in the vessel compared with the same wave in the femoral artery, which spends a longer time on the arterial tree. When measuring the local pulse wave, knowing the arterial physiological information is advantageous. A transducer is inserted into an artery to measure pressure and volume, simultaneously. The velocity is measured as the slope of a linear portion of the pressure-volume loop (PU loop), as shown in Figure 1.26. The use of this technique is limited because of its invasive nature [97].

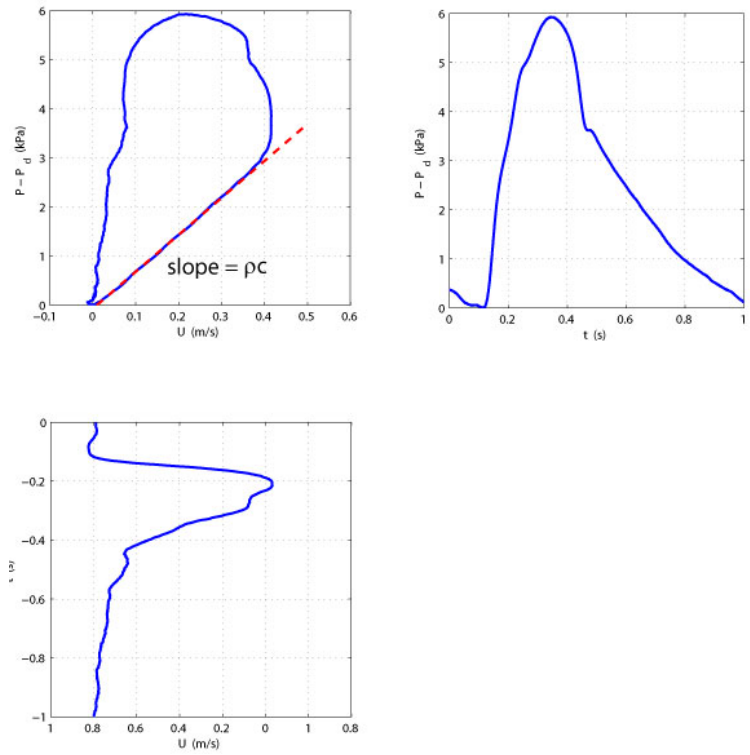

Figure 1.26: PU Loop, generated based on the pressure and velocity waveforms. The red dotted line shows the slope (PWV) [97]

1.14.2 Ultrasound-based BP Measurement

Non-invasive assessments of local BP/PWV have enormous diagnostic potential for the early detection of CVD and the necessity of arteriovenous shunts during surgical operations. Ultrasound systems are used in clinical practice to evaluate blood flow velocity, volumetric blood flow, and arterial wall movements; however, the simultaneous acquisition of waveforms has been challenging. The simultaneous acquisition of flow and distension waveforms has not been viable using conventional models, such as Doppler velocity measurements and M-mode wall tracking. Two sensors have been used to assess average of velocity and distension waveform to obtain smoother results can cause temporal misalignment, as reported by Williams et al. [8]. In recent years, local PWV and vascular impedance assessment mechanisms have been successfully developed [8]. Uniform insonation and echo-tracking can measure the PWV, using the flow-area (QA) method, and the BP waveform can be estimated from the PWV waveform if DBP is known, using a cuff-based monitor [8]. However, the continuous or long-term exposure to ultrasound may warm the muscle, which limits its use for ambulatory assessments.

1.15 Sensor Location Placement Map

1.15.1 Chest and Finger

In the literature, researchers have used the PPG of the index finger to measure arterial waveforms, which provides the most accurate signal for this measurement. ECG signal is typically acquired based on Einthoven's equilateral triangle, and various electrode placements are practised, with chest placement representing one of the most suitable locations [52], [53],[54],[55]–[57]. Various methods have been reported, in which PAT has been calculated from ECG and finger PPG [58],[91], [106]–[110], radial artery PPG [106], using reflectance PPG at the brachial artery [91],[109] or using EBI electrodes [58].

1.15.2 Forehead

The forehead is one of the most stable points for reflected PPG signal acquisition because it provides the excellent and stable reflectance of incident wavelength on the bone. Researchers, worldwide, have exploited this feature to obtain signals for PAT [111]. In addition, mastoid locations have been tested by researchers and various possibilities at forehead for such scenarios. The PAT technique uses ECG and PPG sensors at the forehead or lower body [92][108][112] [108], transmission-mode PPG sensors on the earlobe [92], or a reflectance-mode PPG sensor on the buttocks (via a toilet seat) [112].

1.15.3 PTT and PWV from Fingers and Toes

As described above, the finger is one of the most suitable locations for PPG measurements, and the toe can be used similarly to the index finger [113]. The toe provides a point at a different length from the finger, allowing PWV to be calculated, which is not possible on when using the index fingers of both hands or adjacent fingers, index finger to ear and toe [87].

1.15.4 Carotid to Femoral Arteries

During standard clinical practice, PWV measurements are obtained using the carotid and femoral arteries, with the time and distance relationships for the pulse to reach each location providing the PWV. PWV provides a measurement for aortic stiffness, and the sensors used for measurement include ultrasound and pulse tonometer. SphygmoCor and Compilior Ltd have developed commercial devices. PTT can also be estimated through central arteries [86][87].

1.16 Calibration Mechanism

BP estimations using PTT techniques have been calibrated using intervention techniques, which lower and raise BP. Common methods for raising BP in subjects include high-intensity exertion, such as cycling, running, and the Valsalva manoeuvre, whereas BP can be lowered using Muller's manoeuvre or cold pressor methods [5]. Mental arithmetic and inverted image tracing-type techniques have also been reported in the literature, as shown in Table 1.3. For invasive procedures, pharmacological techniques have been used to lower or raise the BP [51], [59], [71]–[74], [82], [84], [86]–[89], [62], [90]–[92], [114].

Table 1.3: Intervention methods and their effects on BP [5]

Intervention	∆SP/DP [mmHg]
Cold Pressor	+16/+14 (normal) +43/+31 (high BP)
Sustained Handgrip	+45 to 50/+40 (normal)
Nitro-glycerine	–17/–2 (Cath patients) –15/NA (outpatients)
Neck Chamber	–15/–15 (normal)
Mental Arithmetic	+20/+11 (normal)
Slow Breathing	–8/–5 (normal)
Valsalva Maneuverer	–15/–15 (normal)
Posture	< |10|/+4 (normal)
Exercise	+40/+40 (normal)

1.17 Estimation of BP from PTT

One of the methods used to estimate BP from PTT is by solving for MAP in Moens-Korteweg equation and Young's Modulus equation, as described [59], [65], [74], [87], [88], [91], [92], [115], [116]:

$$\mathrm{P} = \frac{1}{\alpha}\ln\left(2\mathrm{r}\rho\frac{\Delta\mathrm{X}^2}{\mathrm{E_o h}}\right) - \frac{2}{\alpha}\ln\left(\mathrm{PTT}\right) \tag{1.2}$$

where ρ represents blood viscous density, h represents artery wall thickness, r represents the artery inner radius, E_o represents the artery Young's modulus, and ΔX represents the heart to finger distance value [117].

Equation 1.2 can be used to determine BP, as follows:

$$BP = K_1 \ln(PTT) + K_2 \tag{1.3}$$

Another equation shape and form, using a non-linear approach and a quadratic function, has been tested, as follows [52], [67] [57], [76]:

$$BP = \frac{K_1}{PTT} + K_2 \tag{1.4}$$

To predict the asymptotic behaviour model, the following equation is used [118].

$$BP = \frac{K_2}{(PTT - K_1)^2} + K_3 \tag{1.5}$$

To estimate BP from PWV the following equation can be used:

$$\mathrm{PWV\ (cm/ms)} = \frac{\mathrm{BDC} \times \mathrm{Height\ (cm)}}{\mathrm{PTT\ (ms)}} \tag{1.6}$$

BDC represents the body correlation factor and use as "0.5" as constant.

$$\mathrm{BP_{PTT}} = \mathrm{P1} \times \mathrm{PWV} \times \mathrm{e}^{\mathrm{P3} \times \mathrm{PWV}} + \mathrm{P2} \times \mathrm{PWV}^{\mathrm{P4}} - (\mathrm{BP_{PTT,cal}} - \mathrm{BP_{cal}}) \tag{1.7}$$

Where, *P1* = 700, *P2* = 766,000, *P3* = –1, and *P4* = 9, $BP_{PTT,cal}$ represents the BP calculated from PTT at a calibrated BP, BP_{cal} represents the cuff-based BP used for calibration, and BP_{PTT} represents the BP estimated from PTT [119].

Another method that can be used to estimated BP from PTT [120] is shown below:

$$\mathrm{SBP} = 526.465 - 1.3813\ \mathrm{PAT} - 0.0012\ \mathrm{HR} - 0.0158\ \mathrm{TDB} - 0.0241\ \mathrm{FET} \tag{1.8}$$

$$\mathrm{DBP} = 265.741 - 0.5681\ \mathrm{PAT} - 0.0299\ \mathrm{HR} - 0.0358\ \mathrm{TDB} - 0.00267\ \mathrm{FET} \quad (1.9)$$

Where *PAT* is the pulse arrival time, *HR* is the heart rate, *TDB* is the arterial stiffness index, and *FET* is the femoral artery elastic wave.

BP can also be estimated using the following method [121]:

$$\mathrm{BP_{sys}} = 215 + 0.2886\ \mathrm{PTT_{PPG}} - 0.8002\mathrm{PTT_{Pressure}} \quad (1.10)$$

$$\mathrm{BP_{dia}} = 123 + 0.4493\ \mathrm{PTT_{PPG}} - 0.7239\mathrm{PTT_{Pressure}} \quad (1.11)$$

Where, BP_{sys} is SBP, PTT_{PPG} is the PPT from the PPG signal, $PTT_{Pressure}$ is the PTT calculated from the pressure cuff, and BP_{dia} is DBP.

Regression analyses have been utilised to predict BP in the literature [62], [64], [85], [86], [89], [118], [66]–[73]. Least square regression has also been used for BP estimation [62], [67], [68], [72], [85], [86], [88], [90], [92]. Calibration intervals have been periodic for all methods.

1.18 Summary

Hypertension is among the largest challenges for healthcare systems, worldwide, and this chapter summarised the evolution of BP measurement methods, their importance, and currently accepted standards. Since ancient times, cuff-based devices have been key tools for measuring BP; however, no clinical-grade devices have been developed for the non-invasive, continuous, cuffless BP measurement. During the last two decades, PWV, PAT, PTT, PU-loops, and pulse wave morphology analysis techniques have been developed, producing clinically significant results. All of the cuffless BP estimation devices and their underlying techniques, which range from tonometric to wearable devices, require frequent calibration mechanisms that rely on conventional cuff-based BP measurements. The accuracies of these techniques do not currently meet the required AAMI/BHS standards. The tonometric and volume clamp methods produce clinical-grade information but lack accuracy due to the operational index and the complex control mechanism, respectively. In contrast, wearable techniques primarily rely on optical technologies, and the implied information is not as significant as information provided by other devices. This study has attempted to combine the

accuracy of a tonometric device into a wearable device, resulting in the development of a novel and accurate device for cuffless BP measurements.

1.19 Overview of the Thesis

This thesis consists of six chapters, including this introductory and background chapter reviewing arterial waveforms (Chapter 1). This chapter describes currently available measurement techniques and the ongoing, state-of-the-art research examining methods for the assessment of hypertension and its related parameters. This chapter also introduces the regulated standards available for the assessment of PB and their acceptable accuracy ranges. This chapter reviewed the historical development of BP sensors and the methods and waveforms used to measure BP and hypertension. Non-invasive assessment methods, based on PPG, tonometric waveforms, and distension waveforms, were also reviewed. The precisions and accuracies of non-invasive sensors and methods were presented to highlight their shortcomings.

Chapter 2 describes the cardiovascular mechanics underlying arterial waveforms, to provide background for the governing principles associated with BP measurements. The parameters necessary to quantify sensor waveforms are presented, to address the key objectives of this thesis. By the end of Chapter 3, current state-of-the-art sensing methodologies and their working principles will be explained. Chapter 3 describes the mathematical derivation of blood flow and pressure waveforms and the relationships between these variables. The mathematical relationships among wave propagations are also derived in Chapter 3. Finally, the mathematical relationships between haemodynamic parameters and the arterial waveform are derived, to validate the theoretical information presented in previous chapters.

Chapter 4 explains the experimental setup that was used to collect the novel dataset and describes the data acquisition platform, protocol, and sensors used for waveform acquisition. Furthermore, Chapter 4 demonstrates the methodology used to compare the waveforms obtained throughout the experimental study with their gold standards. Chapter 5 explains the results and findings from the experimental study described in Chapter 4 and discusses their relevance and limitations. Chapter 6 summarises the scientific findings and provides the main conclusions for this thesis. Chapter 6 also provides suggestions for the continuation and improvement of this study.

1.20 References

[1] World Health Organization, “A global brief on hypertension : silent killer, global public health crisis: World Health Day 2013,” 2013.

[2] G. F. Mitchell, “Arterial stiffness and hypertension: chicken or egg?,” Hypertens. (Dallas, Tex. 1979), vol. 64, no. 2, pp. 210–4, Aug. 2014.

[3] M. Ecobici and C. Stoicescu, “Arterial Stiffness and Hypertension - Which Comes First?,” Maedica (Buchar)., vol. 12, no. 3, pp. 184–190, Sep. 2017.

[4] S. Elhani, T. J. Cleophas, and R. Atiqi, “Lifestyle interventions in the management of hypertension: a survey based on the opinion of 105 practitioners.,” Neth. Heart J., vol. 17, no. 1, pp. 9–12, Jan. 2009.

[5] R. Mukkamala, “Towards Ubiquitous Blood Pressure Monitoring via Pulse Transit Time: Theory and Practice,” IEEE Trans Biomed Eng., vol. 62, no. 8, pp. 1879–1901, Aug. 2015.

[6] W. W. Nichols, M. F. O’Rourke, C. Hartley, and D. A. McDonald, McDonald’s blood flow in arteries theoretic, experimental, and clinical principles. Arnold, 1998.

[7] A. B. Hertzman and C. R. Spealman, “Observations on the finger volume pulse recorded photoelectrically,” Am. J. Physiol., vol. 119, pp. 334–335, 1937.

[8] B. W. A. M. M. Beulen, N. Bijnens, G. G. Koutsouridis, P. J. Brands, M. C. M. Rutten, and F. N. van de Vosse, “Toward Noninvasive Blood Pressure Assessment in Arteries by Using Ultrasound,” Ultrasound Med. Biol., vol. 37, no. 5, pp. 788–797, May 2011.

[9] M. Butlin and A. Qasem, “Large Artery Stiffness Assessment Using SphygmoCor Technology,” Pulse (Basel, Switzerland), vol. 4, no. 4, pp. 180–192, Jan. 2017.

[10] A. E. W. Johnson, “MIMIC-III, a freely accessible critical care database,” Sci. Data, vol. 3, p. 160035, May 2016.

[11] A. V Chobanian, “The Seventh Report of the Joint National Committee on Prevention, Detection, Evaluation, and Treatment of High Blood Pressure,”

JAMA, vol. 289, no. 19, p. 2560, 2003.

[12] S. Committee, I. Engineering, and B. Society, IEEE Standard for Wearable Cuffless Blood Pressure Measuring Devices. 2014.

[13] P. M. Kearney, M. Whelton, K. Reynolds, P. Muntner, P. K. Whelton, and J. He, “Global burden of hypertension--analysis of worldwide data,” Lancet, vol. 365, pp. 217–223, 2005.

[14] X. Zhou, W. Wu, and S. Bao, “[Mobile Health: IEEE Standard for Wearable Cuffless Blood Pressure Measuring Devices].,” Zhongguo Yi Liao Qi Xie Za Zhi, vol. 39, no. 4, pp. 285–7, Jul. 2015.

[15] J. Allen, “Photoplethysmography and its application in clinical physiological measurement,” Physiol. Meas., vol. 28, no. 3, pp. R1–R39, Mar. 2007.

[16] J. P. Lekakis, “Arterial stiffness assessed by pulse wave analysis in essential hypertension: Relation to 24-h blood pressure profile,” Int. J. Cardiol., vol. 102, no. 3, pp. 391–395, 2005.

[17] J. P. Degaute, P. van de Borne, P. Linkowski, and E. Van Cauter, “Quantitative analysis of the 24-hour blood pressure and heart rate patterns in young men.,” Hypertension, 1991.

[18] J. Blacher, A. P. Guerin, B. Pannier, S. J. Marchais, M. E. Safar, and G. M. London, “Impact of aortic stiffness on survival in end-stage renal disease.,” Circulation, vol. 99, no. 18, pp. 2434–9, 1999.

[19] A. L. Pauca, M. F. O. Rourke, and N. D. Kon, “Prospective Evaluation of a Method for Estimating Ascending Aortic Pressure From the Radial Artery Pressure Waveform,” 2010.

[20] M. J. Roman, “Central pressure more strongly relates to vascular disease and outcome than does brachial pressure: The strong heart study,” Hypertension, vol. 50, no. 1, pp. 197–203, 2007.

[21] E. Koroboki, “Circadian Variation of Blood Pressure and Heart Rate in Normotensives, White-Coat, Masked, Treated and Untreated Hypertensives,” Hell. J. Cardiol., vol. 7, pp. 432–438, 2012.

[22] I. B. Wilkinson, J. R. Cockcroft, and D. J. Webb, “Pulse wave analysis and arterial stiffness.,” J. Cardiovasc. Pharmacol., vol. 32 Suppl 3, pp. S33-7, 1998.

[23] P. Boutouyrie and S. J. Vermeersch, “Determinants of pulse wave velocity in healthy people and in the presence of cardiovascular risk factors: Establishing normal and reference values,” Eur. Heart J., vol. 31, no. 19, pp. 2338–2350, 2010.

[24] G. Mancia, “2013 ESH/ESC Guidelines for the management of arterial hypertension,” J. Hypertens., vol. 31, no. 7, pp. 1281–1357, Jul. 2013.

[25] L. T. Hersh, B. Friedman, W. Luczyk, and J. Sesing, “Evaluation of filtering methods for acquiring radial intra-artery blood pressure waveforms,” J. Clin. Monit. Comput., vol. 29, no. 5, pp. 659–669, 2015.

[26] K. Tegtmeyer, G. Brady, S. Lai, R. Hodo, and D. Braner, “Placement of an Arterial Line,” N. Engl. J. Med., vol. 354, no. 15, p. e13, Apr. 2006.

[27] J. F. H.Dally, High Blood Pressure : Its Variations and Control. William Heinemann, 1934.

[28] Atkins, O’Brien, Wesseling, and I. Guelen, “Increasing observer objectivity with audio-visual technology: the Sphygmocorder.,” Blood Press. Monit., vol. 2, no. 5, pp. 269–272, Oct. 1997.

[29] S. Blanchard, “ANATOMY AND PHYSIOLOGY,” in Introduction to Biomedical Engineering, pp. 73–125, 2005.

[30] M. Forouzanfar, S. Ahmad, I. Batkin, H. R. Dajani, V. Z. Groza, and M. Bolic, “Coefficient-Free Blood Pressure Estimation Based on Pulse Transit Time–Cuff Pressure Dependence,” IEEE Trans. Biomed. Eng., vol. 60, no. 7, pp. 1814–1824, Jul. 2013.

[31] G. Bilo, “Impact of cuff positioning on blood pressure measurement accuracy: may a specially designed cuff make a difference?,” Hypertens. Res., vol. 40, no. 6, pp. 573–580, Jun. 2017.

[32] C. F. Babbs, “Oscillometric measurement of systolic and diastolic blood pressures validated in a physiologic mathematical model.,” Biomed. Eng.

Online, vol. 11, p. 56, Aug. 2012.

[33] E. D. M. Dias, “Carotid intima-media thickness is associated with cognitive deficiency in hypertensive patients with elevated central systolic blood pressure.,” Cardiovasc. Ultrasound, vol. 10, p. 41, 2012.

[34] C. M. McEniery, J. R. Cockcroft, M. J. Roman, S. S. Franklin, and I. B. Wilkinson, “Central blood pressure: current evidence and clinical importance,” Eur. Heart J., vol. 35, no. 26, pp. 1719–25, Jul. 2014.

[35] G. C. Cloud, C. rajkumar, J. Kooner, J. Cooke, and C. J. Bulpit, “Estimation of central aortic pressure by SphygmoCor® requires intra-arterial peripheral pressures,” Clin. Sci., vol. 105, no. 2, pp. 219–225, Aug. 2003.

[36] A. S. Meidert, “Radial artery applanation tonometry for continuous non-invasive arterial pressure monitoring in intensive care unit patients: Comparison with invasively assessed radial arterial pressure,” Br. J. Anaesth., vol. 112, no. 3, pp. 521–528, 2014.

[37] J. Y. Wagner, “Continuous noninvasive arterial pressure measurement using the volume clamp method: an evaluation of the CNAP device in intensive care unit patients,” J. Clin. Monit. Comput., vol. 29, no. 6, pp. 807–813, 2015.

[38] Penaz, “Photoelectric measurement of blood pressure, volume and flow in the finger,” Dig. 10th Int. Conf. Med. Biol. Eng., 1973.

[39] B. P. Imholz, W. Wieling, G. A. van Montfrans, and K. H. Wesseling, “Fifteen years experience with finger arterial pressure monitoring: assessment of the technology.,” Cardiovasc. Res., vol. 38, no. 3, pp. 605–16, Jun. 1998.

[40] J. Y. Wagner, J. Grond, J. Fortin, I. Negulescu, M. Schöfthaler, and B. Saugel, “Continuous noninvasive cardiac output determination using the CNAP system: evaluation of a cardiac output algorithm for the analysis of volume clamp method-derived pulse contour,” J. Clin. Monit. Comput., 2015.

[41] Y. Van Der Does, “Non-invasive blood pressure and cardiac index measurements using the Finapres Portapres in an emergency department triage setting,” Am. J. Emerg. Med., vol. 31, no. 7, pp. 1012–1016, 2013.

[42] “Smartsigns Compact 300 Monitor | Obstetrics Patient Monitoring | Smartsigns | Monitors | Huntleigh Healthcare Limited | Huntleigh Diagnostic Products Division | Part of the Getinge Group.” [Online]. Available: http://www.huntleigh-diagnostics.com/store/obstetric-monitoring/patient-monitoring/smartsigns-compact-300. [Accessed: 20-May-2019].

[43] “ABPM 7100 Ambulatory Blood Pressure Monitor.” [Online]. Available: https://www.welchallyn.com/en/products/categories/cardiopulmonary/ambulatory-blood-pressure-monitor/abpm-7100-blood-pressure-monitor.html. [Accessed: 20-May-2019].

[44] J. A. Walsh, E. J. Topol, and S. R. Steinhubl, “Novel Wireless Devices for Cardiac Monitoring,” Circulation, vol. 130, no. 7, pp. 573–581, Aug. 2014.

[45] G. Guanqun Zhang, S. A. McCombie, R. Greenstein, and D. B. McCombie, “Assessing the challenges of a pulse wave velocity based blood pressure measurement in surgical patients,” in 2014 36th Annual International Conference of the IEEE Engineering in Medicine and Biology Society, 2014, vol. pp. 574–577, 2014.

[46] L. S. Manning, T. G. Robinson, and R. B. Panerai, “The SOMNOtouch device as a novel method for measuring short-term blood pressure variability,” Blood Press. Monit., vol. 20, no. 6, pp. 361–368, Dec. 2015.

[47] K.-G. Ng, “Progress on the development of the MediWatch ambulatory blood pressure monitor and related devices,” Blood Press. Monit., vol. 9, no. 3, pp. 149–65, Jun. 2004.

[48] J. McLaughlin, M. McNeill, B. Braun, and P. D. McCormack, “Piezoelectric sensor determination of arterial pulse wave velocity,” Physiol. Meas., vol. 24, no. 3, pp. 693–702, Aug. 2003.

[49] L. A. Geddes, M. H. Voelz, C. F. Babbs, J. D. Bourland, and W. A. Tacker, “Pulse transit time as an indicator of arterial blood pressure,” Psychophysiology, vol. 18, no. 1, pp. 71–4, Jan. 1981.

[50] W. S. Harris, C. D. Schoenfeld, and A. M. Weissler, “Effects of Adrenergic Receptor Activation and Blockade on the Systolic Preejection Period, Heart

Rate, and Arterial Pressure in Man," J. Clin. Invest., vol. 46, no. 11, pp. 1704–1714, Nov. 1967.

[51] H. Gesche, D. Grosskurth, G. Küchler, and A. Patzak, "Continuous blood pressure measurement by using the pulse transit time: Comparison to a cuff-based method," Eur. J. Appl. Physiol., vol. 112, no. 1, pp. 309–315, Jan. 2012.

[52] G. Jeong, K. Yu, and N. Kim, "Continuous Blood Pressure Monitoring using Pulse Wave Transit Time," Measurement, pp. 2–5, 2005.

[53] S. Ye, G. Kim, and D. Jung, "Estimation of systolic and diastolic pressure using the pulse transit time," World Academy of Science, vol. 43, no. 7, pp. 726–731, 2010.

[54] R. Magjarevic, Measuring Blood Pressure Using a Photoplethysmography Approach, vol. 21,, Heidelberg: Springer Berlin Heidelberg, 2008.

[55] C. Yu, "Optomechanical magnetometry with a macroscopic resonator," IEEE Sens. J., vol. 14, no. 10, pp. 3490–3497, Oct. 2015.

[56] S. Fuke, T. Suzuki, K. Nakayama, H. Tanaka, and S. Minami, "Blood pressure estimation from pulse wave velocity," 35th Annu. Int. Conf. IEEE EMBS, pp. 6107–6110, 2013.

[57] S. Mazaheri, "A Comparative Review of Blood Pressure Measurement Methods Using Pulse Wave Velocity," IEEE International Conference on Smart Instrumentation, Measurement and Applications (ICSIMA), pp 1-5, Kuala Lumpur, 2014.

[58] C. Douniama, C. Sauter, and R. Couronné, "Blood pressure tracking capabilities of pulse transit times in different arterial segments: A clinical evaluation," 36th Annu. Comput. Cardiol. Conf., pp. 201–204, 2009.

[59] C. C. Y. Poon and Y. T. Zhang, "Cuff-less and Noninvasive Measurements of Arterial Blood Pressure by Pulse Transit Time," in 2005 IEEE Engineering in Medicine and Biology 27th Annual Conference, 2005, vol. 6, pp. 5877–5880.

[60] R. A. Payne, C. N. Symeonides, D. J. Webb, and S. R. J. Maxwell, "Pulse transit time measured from the ECG: an unreliable marker of beat-to-beat blood

pressure," J. Appl. Physiol., vol. 100, no. 1, pp. 136–141, Jan. 2006.

[61] C. Ahlstrom, A. Johansson, F. Uhlin, T. Länne, and P. Ask, "Noninvasive investigation of blood pressure changes using the pulse wave transit time: a novel approach in the monitoring of hemodialysis patients," J. Artif. Organs, vol. 8, no. 3, pp. 192–197, Oct. 2005.

[62] Y. Choi, Q. Zhang, and S. Ko, "Noninvasive cuffless blood pressure estimation using pulse transit time and Hilbert–Huang transform," Comput. Electr. Eng., vol. 39, no. 1, pp. 103–111, Jan. 2013.

[63] D. Spulak, R. Cmejla, and V. Fabian, "Parameters for mean blood pressure estimation based on electrocardiography and photoplethysmography," in 2011 International Conference on Applied Electronics, no. 2, pp. 1–4, 2011.

[64] I. cheol Jeong, J. Wood, and J. Finkelstein, "Using individualized pulse transit time calibration to monitor blood pressure during exercise," Stud. Health Technol. Inform., vol. 190, pp. 39–41, 2013.

[65] W. Chen, T. Kobayashi, S. Ichikawa, Y. Takeuchi, and T. Togawa, "Continuous estimation of systolic blood pressure using the pulse arrival time and intermittent calibration," Med. Biol. Eng. Comput., vol. 38, no. 5, pp. 569–74, Sep. 2000.

[66] Y. S. Yan and Y. T. Zhang, "A Novel Calibration Method for Noninvasive Blood Pressure Measurement Using Pulse Transit Time," in 2007 4th IEEE/EMBS International Summer School and Symposium on Medical Devices and Biosensors, pp. 22–24, 2007.

[67] F. S. Cattivelli and H. Garudadri, "Noninvasive Cuffless Estimation of Blood Pressure from Pulse Arrival Time and Heart Rate with Adaptive Calibration," in 2009 Sixth International Workshop on Wearable and Implantable Body Sensor Networks, pp. 114–119, 2009.

[68] M. Masè, W. Mattei, R. Cucino, L. Faes, and G. Nollo, "Feasibility of cuff-free measurement of systolic and diastolic arterial blood pressure," J. Electrocardiol., vol. 44, no. 2, pp. 201–207, Mar. 2011.

[69] J. Muehlsteff, X. L. Aubert, and M. Schuett, "Cuffless Estimation of Systolic

Blood Pressure for Short Effort Bicycle Tests: The Prominent Role of the Pre-Ejection Period," in 2006 International Conference of the IEEE Engineering in Medicine and Biology Society, vol. 1, pp. 5088–5092, 2006.

[70] Y. Yoon, J. H. Cho, and G. Yoon, "Non-constrained blood pressure monitoring using ECG and PPG for personal healthcare.," J. Med. Syst., vol. 33, no. 4, pp. 261–6, Aug. 2009.

[71] A. Jadooei, O. Zaderykhin, and V. I. Shulgin, "Adaptive algorithm for continuous monitoring of blood pressure using a pulse transit time," in 2013 IEEE XXXIII International Scientific Conference Electronics and Nanotechnology (ELNANO), pp. 297–301, 2013.

[72] H. T. Ma, "A Blood Pressure Monitoring Method for Stroke Management," Biomed Res. Int., vol. 2014, pp. 1–7, 2014.

[73] S. S. Thomas, "BioWatch — A wrist watch based signal acquisition system for physiological signals including blood pressure," in 2014 36th Annual International Conference of the IEEE Engineering in Medicine and Biology Society, 2014, vol., pp. 2286–2289, 2014.

[74] B. M. McCarthy, B. O'Flynn, and A. Mathewson, "An Investigation of Pulse Transit Time as a Non-Invasive Blood Pressure Measurement Method," J. Phys. Conf. Ser., vol. 307, no. 1, p. 012060, Aug. 2011.

[75] A. M. Katz, "Physiology of the heart," Clin. Cardiol., vol. 4, no. 4, pp. 196–196, Jul. 1981.

[76] G. Zhang, M. Gao, D. Xu, N. B. Olivier, and R. Mukkamala, "Pulse arrival time is not an adequate surrogate for pulse transit time as a marker of blood pressure," J. Appl. Physiol., vol. 111, no. 6, pp. 1681–1686, Dec. 2011.

[77] Q. Zhang, "Cuff-less blood pressure measurement using pulse arrival time and a Kalman filter," J. Micromechanics Microengineering, vol. 27, no. 2, p. 024002, Feb. 2017.

[78] P. A. Shaltis, A. Reisner, and H. H. Asada, "Wearable, Cuff-less PPG-Based Blood Pressure Monitor with Novel Height Sensor," in 2006 International

Conference of the IEEE Engineering in Medicine and Biology Society, vol. 1, pp. 908–911, 2006.

[79] A. Marinkovid, A. Marinkovid, H. H. Asada, T. Supervisor, and L. Anand, “Reconstructing the Blood Pressure Waveform using a Wearable,” 39th Annual International Conference of the IEEE Engineering in Medicine and Biology Society (EMBC), Seogwipo, pp. 821-824, 2007.

[80] R. Asmar, “Assessment of arterial distensibility by automatic pulse wave velocity measurement. Validation and clinical application studies,” Hypertens. (Dallas, Tex. 1979), vol. 26, no. 3, pp. 485–90, Sep. 1995.

[81] W. Lu, “Research on the main elements influencing blood pressure measurement by pulse wave velocity.,” Front. Med. Biol. Eng., vol. 4, no. 3, pp. 189–99, 1992.

[82] B. M. McCarthy, C. J. Vaughan, B. O’Flynn, A. Mathewson, and C. Ó Mathúna, “An examination of calibration intervals required for accurately tracking blood pressure using pulse transit time algorithms,” J. Hum. Hypertens., vol. 27, no. 12, pp. 744–750, Dec. 2013.

[83] J. E. Davies, “Use of simultaneous pressure and velocity measurements to estimate arterial wave speed at a single site in humans,” Am J Physiol Heart Circ Physiol. 290(2), pp 878-85, 2006.

[84] B. Gribbin, A. Steptoe, and P. Sleight, “Pulse wave velocity as a measure of blood pressure change.,” Psychophysiology, vol. 13, no. 1, pp. 86–90, Jan. 1976.

[85] H. Gesche, D. Grosskurth, G. Küchler, and A. Patzak, “Continuous blood pressure measurement by using the pulse transit time: comparison to a cuff-based method,” Eur. J. Appl. Physiol., vol. 112, no. 1, pp. 309–315, Jan. 2012.

[86] J. Sola, “Noninvasive and Nonocclusive Blood Pressure Estimation Via a Chest Sensor,” IEEE Trans. Biomed. Eng., vol. 60, no. 12, pp. 3505–3513, Dec. 2013.

[87] Y. Chen, C. Wen, G. Tao, M. Bi, and G. Li, “Continuous and Noninvasive Blood Pressure Measurement: A Novel Modeling Methodology of the Relationship

Between Blood Pressure and Pulse Wave Velocity," Ann. Biomed. Eng., vol. 37, no. 11, pp. 2222–2233, Nov. 2009.

[88] D. B. McCombie, A. T. Reisner, and H. H. Asada, "Motion based adaptive calibration of pulse transit time measurements to arterial blood pressure for an autonomous, wearable blood pressure monitor," in 2008 30th Annual International Conference of the IEEE Engineering in Medicine and Biology Society, 2008, vol., pp. 989–992, 2008.

[89] C. C. Young, J. B. Mark, W. White, A. DeBree, J. S. Vender, and A. Fleming, "Clinical evaluation of continuous noninvasive blood pressure monitoring: accuracy and tracking capabilities.," J. Clin. Monit., vol. 11, no. 4, pp. 245–52, Jul. 1995.

[90] M. Mingwu Gao and R. Mukkamala, "Perturbationless calibration of pulse transit time to blood pressure," in 2012 Annual International Conference of the IEEE Engineering in Medicine and Biology Society,, pp. 232–235, 2012.

[91] P. Rai et al., "Smart healthcare textile sensor system for unhindered-pervasive health monitoring," SPIE Proceedings, vol. 8344, 2012.

[92] G. Lopez, "Continuous Blood Pressure Monitoring in Daily Life," J. Adv. Mech. Des. Syst. Manuf., vol. 4, no. 1, pp. 179–186, 2010.

[93] D. B. McCombie, "Development of a wearable blood pressure monitor using adaptive calibration of peripheral pulse transit time measurements," Thesis (Ph. D.) Massachusetts Institute of Technology, Dept. of Mechanical Engineering, 2008.

[94] K. Li and S. Warren, "A Wireless Reflectance Pulse Oximeter With Digital Baseline Control for Unfiltered Photoplethysmograms," IEEE Trans. Biomed. Circuits Syst., vol. 6, no. 3, pp. 269–278, Jun. 2012.

[95] A.-G. Pielmus, "Novel computation of pulse transit time from multi-channel PPG signals by wavelet transform," Curr. Dir. Biomed. Eng., vol. 2, no. 1, pp. 209–213, Jan. 2016.

[96] C. M. McClean, "The effect of acute aerobic exercise on pulse wave velocity and

oxidative stress following postprandial hypertriglyceridemia in healthy men," Eur. J. Appl. Physiol., vol. 100, no. 2, pp. 225–234, 2007.

[97] K. H. Parker, "An introduction to wave intensity analysis," Med. Biol. Eng. Comput., vol. 47, no. 2, pp. 175–188, Feb. 2009.

[98] S. Laurent, "Expert consensus document on arterial stiffness: methodological issues and clinical applications," Eur. Heart J., vol. 27, no. 21, pp. 2588–2605, Sep. 2006.

[99] E. S. Winokur, "Single-Site, Noninvasive, Blood Pressure Measurements at the Ear using Ballistocardiogram (BCG), and Photoplethysmogram (PPG), and a Low-Power, Reflectance-Mode PPG SoC," 2013.

[100] S. L.-O. Martin, "Weighing Scale-Based Pulse Transit Time is a Superior Marker of Blood Pressure than Conventional Pulse Arrival Time," Sci. Rep., vol. 6, no. 1, p. 39273, Dec. 2016.

[101] E. von Wowern, G. Östling, P. M. Nilsson, and P. Olofsson, "Digital Photoplethysmography for Assessment of Arterial Stiffness: Repeatability and Comparison with Applanation Tonometry," PLoS One, vol. 10, no. 8, p. e0135659, Aug. 2015.

[102] J. C. Dorlas and J. A. Nijboer, "Photo-electric plethysmography as a monitoring device in anaesthesia. Application and interpretation.," Br. J. Anaesth., vol. 57, no. 5, pp. 524–30, May 1985.

[103] E. C.-P. Chua, S. J. Redmond, G. McDarby, and C. Heneghan, "Towards Using Photo-Plethysmogram Amplitude to Measure Blood Pressure During Sleep," Ann. Biomed. Eng., vol. 38, no. 3, pp. 945–954, Mar. 2010.

[104] A. A. Awad, "The relationship between the photoplethysmographic waveform and systemic vascular resistance," J. Clin. Monit. Comput., vol. 21, no. 6, pp. 365–372, Nov. 2007.

[105] L. Wang, E. Pickwell-MacPherson, Y. P. Liang, and Y. T. Zhang, "Noninvasive cardiac output estimation using a novel photoplethysmogram index," in 2009 Annual International Conference of the IEEE Engineering in Medicine and

Biology Society, pp. 1746–1749, 2009.

[106] J. D. Lane, L. Greenstadt, D. Shapiro, and E. Rubinstein, “Pulse transit time and blood pressure: an intensive analysis.,” Psychophysiology, vol. 20, no. 1, pp. 45–9, Jan. 1983.

[107] A. Steptoe, H. Smulyan, and B. Gribbin, “Pulse wave velocity and blood pressure change: calibration and applications.,” Psychophysiology, vol. 13, no. 5, pp. 488–93, Sep. 1976.

[108] P. A. Obrist, K. C. Light, J. A. McCubbin, J. S. Hutcheson, and J. L. Hoffer, “Pulse transit time: relationship to blood pressure and myocardial performance.,” Psychophysiology, vol. 16, no. 3, pp. 292–301, May 1979.

[109] Y.-L. Ya-Li Zheng, B. P. Yan, Y.-T. Yuan-Ting Zhang, and C. C. Y. Poon, “An Armband Wearable Device for Overnight and Cuff-Less Blood Pressure Measurement,” IEEE Trans. Biomed. Eng., vol. 61, no. 7, pp. 2179–2186, Jul. 2014.

[110] G. V Marie, C. R. Lo, J. Van Jones, and D. W. Johnston, “The relationship between arterial blood pressure and pulse transit time during dynamic and static exercise.,” Psychophysiology, vol. 21, no. 5, pp. 521–7, Sep. 1984.

[111] L. A. Geddes, M. Voelz, S. James, and D. Reiner, “Pulse arrival time as a method of obtaining systolic and diastolic blood pressure indirectly.,” Med. Biol. Eng. Comput., vol. 19, no. 5, pp. 671–2, Sep. 1981.

[112] J. S. Kim, Y. J. Chee, J. W. Park, J. W. Choi, and K. S. Park, “A new approach for non-intrusive monitoring of blood pressure on a toilet seat,” Physiol. Meas., vol. 27, no. 2, pp. 203–211, Feb. 2006.

[113] Snapshots of Hemodynamics, vol. 18. Boston: Kluwer Academic Publishers, 2005.

[114] D. J. Hughes, C. F. Babbs, L. A. Geddes, and J. D. Bourland, “Measurements of Young’s Modulus of Elasticity of the Canine Aorta with Ultrasound,” Ultrason. Imaging, vol. 1, no. 4, pp. 356–367, Oct. 1979.

[115] T. Wibmer, “Blood pressure monitoring during exercise: Comparison of pulse

transit time and volume clamp methods.," Blood Press., vol. 24, no. 6, pp. 353–60, 2015.

[116] C. C. Y. Poon, Y. Zhang, and Y. Liu, "Modeling of Pulse Transit Time under the Effects of Hydrostatic Pressure for Cuffless Blood Pressure Measurements," in 2006 3rd IEEE/EMBS International Summer School on Medical Devices and Biosensors, pp. 65–68, 2006.

[117] E. Hermeling, "The change in arterial stiffness over the cardiac cycle rather than diastolic stiffness is independently associated with left ventricular mass index in healthy middle-aged individuals," J. Hypertens., vol. 30, no. 2, pp. 396–402, Feb. 2012.

[118] T. Wibmer, "Pulse transit time and blood pressure during cardiopulmonary exercise tests.," Physiol. Res., vol. 63, no. 3, pp. 287–96, 2014.

[119] G. J. Langewouters, K. H. Wesseling, and W. J. Goedhard, "The static elastic properties of 45 human thoracic and 20 abdominal aortas in vitro and the parameters of a new model.," J. Biomech., vol. 17, no. 6, pp. 425–35, 1984.

[120] M. Remoissenet, Waves Called Solitons. Berlin, Heidelberg: Springer Berlin Heidelberg, 1999.

[121] E. Hermeling, "Noninvasive Assessment of Arterial Stiffness Should Discriminate Between Systolic and Diastolic Pressure Ranges," Hypertension, vol. 55, no. 1, pp. 124–130, Jan. 2010.

Chapter 2

Physiology of Arterial Waveforms, Sensors, and Measurement Methods

This chapter describes the basic cardiovascular physiology principles and mechanics that are necessary to understand the concepts of blood flow underlying the arterial stiffness assessment. This chapter outlines the following concepts: blood flow from the heart, the Windkessel effect in the aorta, the effects of arterial tree dynamics on blood flow, and the effects of reflected waves on pressure and flow waveforms. The elasticity of the arteries, blood rheumatology, and their complexity inflow will also be described, in the context of blood flow and PWV. The methods used to estimate arterial stiffness, including arterial waveform morphology, PTT, HRV, and local PU-loop methods, are explored and compared across different sensing methodologies.

2.1 The Cardiovascular Mechanics

The cardiovascular system's primary purpose is to transport blood to and from the organs, where gaseous and nutrient exchanges occur in tissues, at the cellular level. These exchanges occur in a convection fashion, which allows it to overcome massive precapillary resistance. Further explanations can be found in the book 'Computational Cardiovascular Mechanics' [1].

The heart works as a mechanical pump, and its circulation system has two components, pulmonary circulation and systemic circulation. Pulmonary circulation emanates from the right atrium (RA) and right ventricle (RV), where the vena cava stores blood before oxygenation by the lungs. Systemic circulation emanates from the left ventricle (LV) and the left atrium (LA), which receives oxygenated blood from the pulmonary veins, and the LV pumps the blood to the whole body, as shown in Figure 2.1. The heart pumps blood in a non-continuous manner, into the aorta. The ventricle pressure-volume relationship during each beat has four stages: ventricular filling, isovolumetric contraction, ejection, and isovolumetric relaxation. The cardiac cycle is illustrated in Figure 2.2, using Wigger's diagram, in which the temporal relationships between ventricular pressure, ventricular volume, atrial pressure, and aortic pressure are shown.

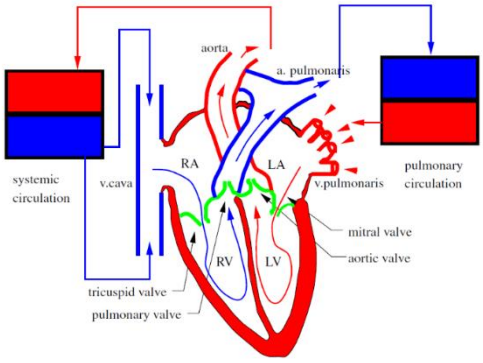

Figure 2.1: Schematic view of the cardiac circulation system [2]

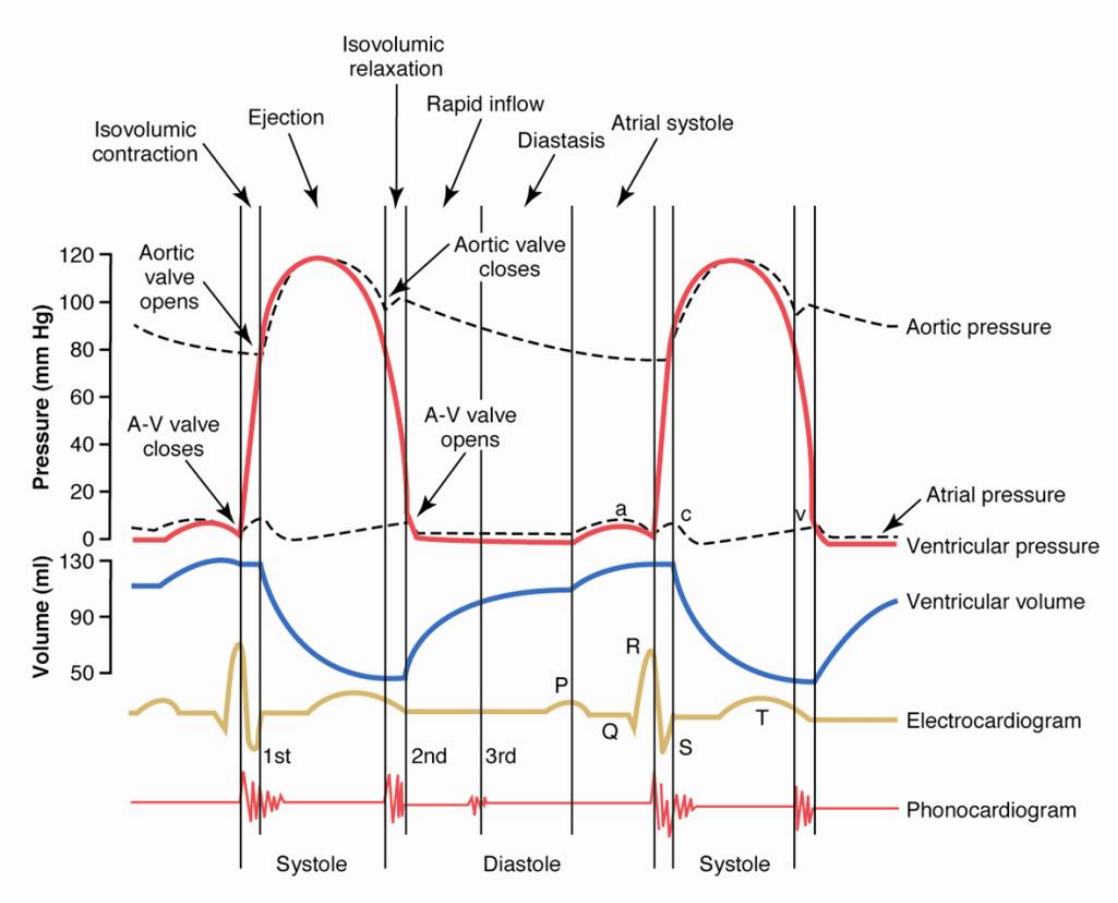

Figure 2.2: Wigger's Diagram [3]

2.2 Facts About the Heart and Arterial Flow

BP and blood flow are generated by the heart, which is essential for transport in a closed-loop system. During an average lifetime of 70 years, the human heart beats more than 2.5 billion times and pumps approximately 1 million barrels of blood, which travels 0.3 billion miles in the arterial tree [4].

2.3 The Arterial Tree and Blood Circulation

Arteries are composed of four layers, the endothelium, elastin, collagen, and smooth muscle. The endothelium is a single-cell layer, which regulates the blood for a smooth layer. Elastin is the most flexible part of the wall and is a central component of the aorta. Collagen is 400 times stiffer than elastin and becomes active at high BP. Smooth muscles produce tension via physiological changes and are prominent components of the peripheral arteries. The Maxwell artery model can be used to characterise the features [5][6], as shown in Figure 2.3 (a-d).

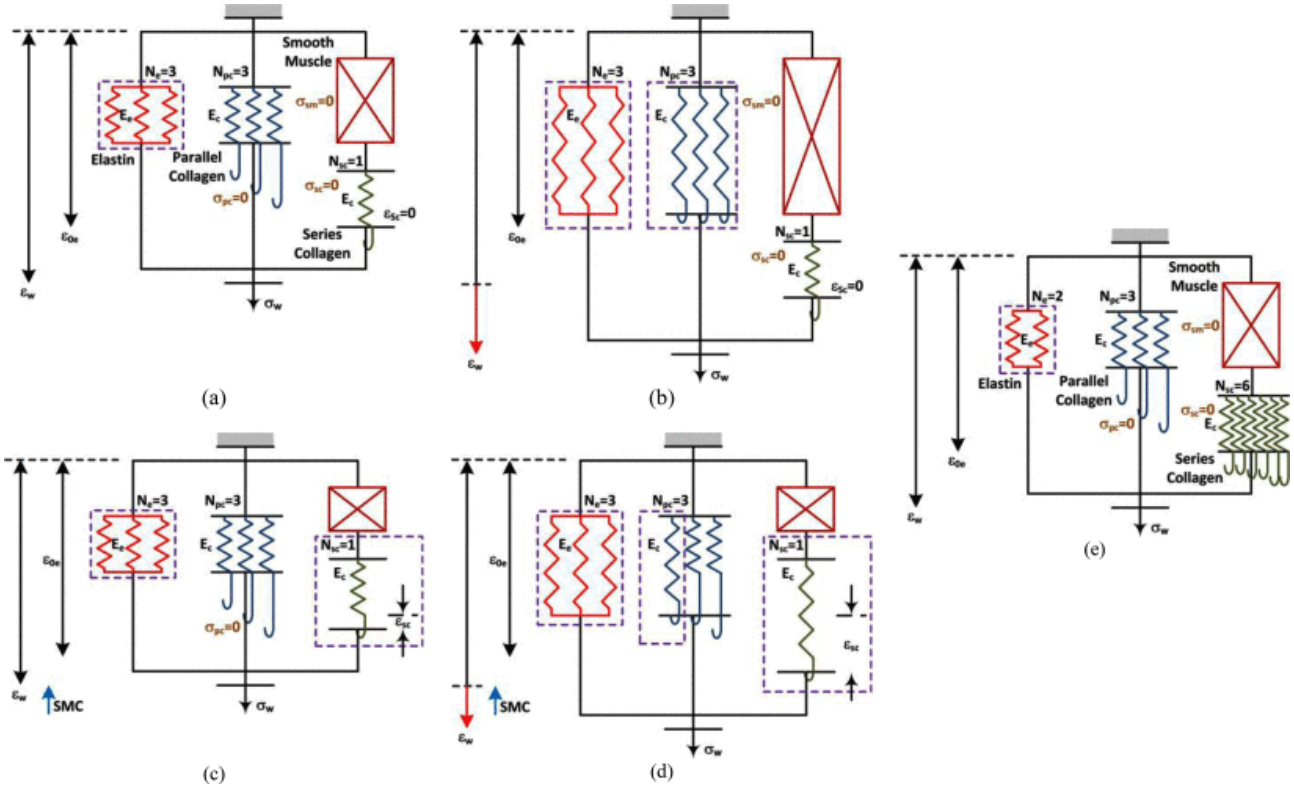

Figure 2.3: The Maxwell Arterial Model [6]

In this model, *'E'* represents elasticity, the subscript *'e'* represents elastin, and *'c'* represents collagen. For double subscripts, *'s'* represents series and *'p'* represents parallel. *'N'* represents the number of elements, $'\varepsilon'$ represents strain, and $'\sigma'$ represents wall stress. Figure 2.3a and b show the low extension and high extension of the central wall, respectively, during smooth muscle relaxation. Figure 2.3c and d show the low extension and high extension of the central wall, respectively, during smooth muscle contraction, and Figure 2.3e shows the peripheral wall. The spring represents elastin, the hook represents collagen, and the box with a cross represents the smooth muscles.

Arteries can be categorised into four categories, based on their sizes: large arteries, small arteries, arterioles, and capillaries. In the circulation system, the heart works periodically, alternating between high-volume and no-volume blood flow. When BP in the LV increases, aortic pressure opens the aortic valves, and blood is ejected into the ascending aorta, which is referred to as systole. When LV pressure falls, the aortic valve closes and no blood flows from the heart, which is referred to as diastole. The aorta connects to arteries, which connect to arterioles and then to capillaries.

The pressure in the systematic circulation system ranges from 80–120 mmHg in healthy adults, under relaxed conditions, whereas the pressure in the pulmonary circulation system ranges from 8–25 mmHg. Furthermore, the pressure in the pulmonary capillaries ranges from 0–7 mmHg in the systemic arteries. The pressure level in the arterial network is shown in Figure 2.4.

The arterial tree walls dilate and constrict to regulate BP, which are referred to as vasodilation and vasoconstriction, respectively. Blood regulation depends on blood in the tissues, which passes through the capillaries. The exchange of fluid, gas, nutrients, hormones, and other substances occurs in the capillaries. Venules collect the blood and transport them to veins, which progressively increase in size, as shown in Figure 2.5.

The arterial wall consists of elastic fibres and smooth muscles, which make the arteries behave in a viscoelastic manner. When moving from a larger artery to a smaller artery, the elastic fibre composition gradually decreases, whereas smooth muscles increase, as stated by Ottesen et al. [7].

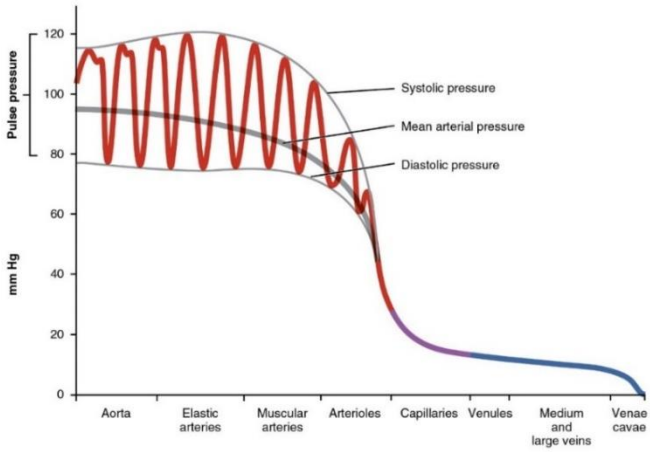

Figure 2.4: The pressure in the arterial network [9]

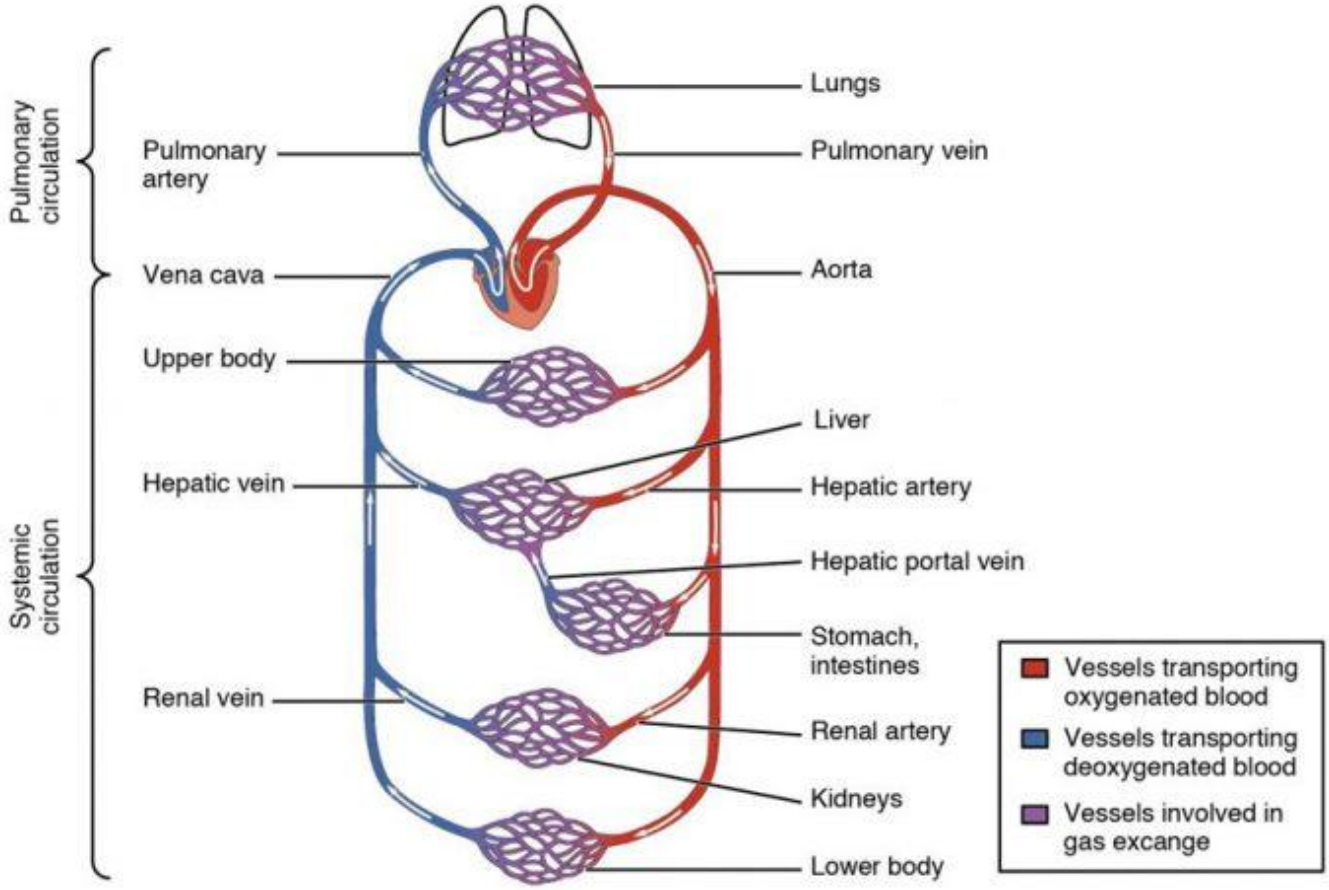

Figure 2.5: The circulatory system [8]

2.4 Windkessel Effect

In the circulatory system, the aorta is the most prominent artery, which changes the heart's non-continuous flow into a continuous flow. During systole, aortic pressure increases, whereas, during diastole, pressure decreases until the next systole. Aortic compliance gives the aorta the capacity to hold a large amount of blood, a phenomenon that was explained by Otto Franks using the Windkessel (WK) model, which is shown in Figure 2.6.

In its simplest form, the WK is comprised of two parameters: resistance and compliance (often known as capacitance), relative to the aorta. Resistance depends on the radius of the aorta, whereas compliance depends on the elasticity of the aorta. Higher resistance is associated with a higher LV load, whereas higher compliance is associated with a lower LV load.

In the WK model, the aorta is analogous to a chamber filled with air and attached to a pump. The pump fills the chamber with water, which compresses the air and pushes the water outside. Similar to how the air pocket can be compressed and decompressed by water flow, a similar phenomenon occurs in the aorta due to elasticity.

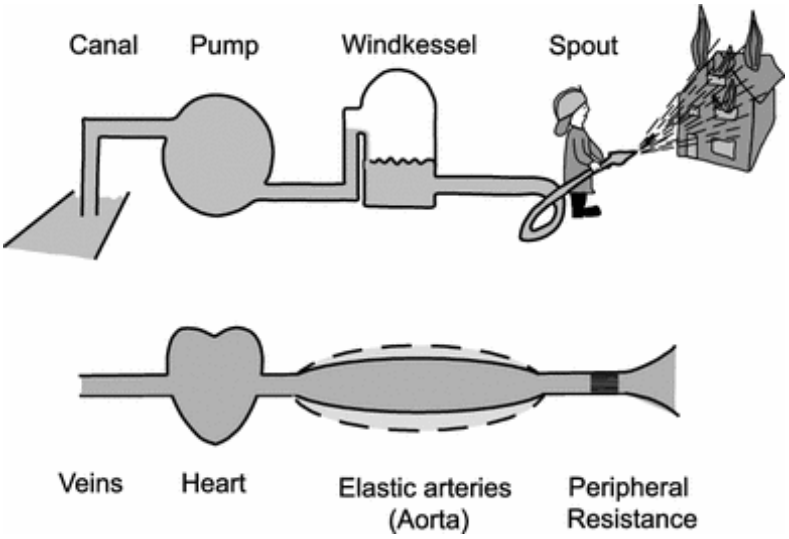

Figure 2.6: Windkessel effect [10]

2.5 Pulse Wave Velocity

"The Scientific understanding of the pulse and its application to medicine has at all times been dependent on the knowledge of the theory and of physiological mechanisms, and on tile availability of methods for its measurements." The importance of the arterial pulse is emphasised in "The Arterial Pulse" by O'Rourke, Kelly and Avolio (1992) [11].

The accurate estimation of arterial stiffness is known to have great diagnostic and prognostic value and has attracted much research attention during recent decades. PWV is a non-invasive, straightforward, and reproducible method for the measurement of arterial stiffness. PWV *'is not blood flow velocity'*; furthermore, PWV is at least 20 times faster than blood flow velocity in a healthy subject.

To understand the concept of PWV, the analogy of shock wave behaviour through solids and liquids can be used. Newton's cradle is an ideal example of the movement of a shockwave, as shown in Figure 2.7. When the observer raises the hanging steel ball and then releases it, the ball converts potential energy to kinetic energy, hitting the other hanging balls. As it strikes, the ball generates a shock wave that moves the

last ball, which swings like a pendulum. The movement of the shock wave is a thousand times faster and independent of the speed of the first ball. The last ball breaks away with a speed similar to that of the first ball when it struck the second ball.

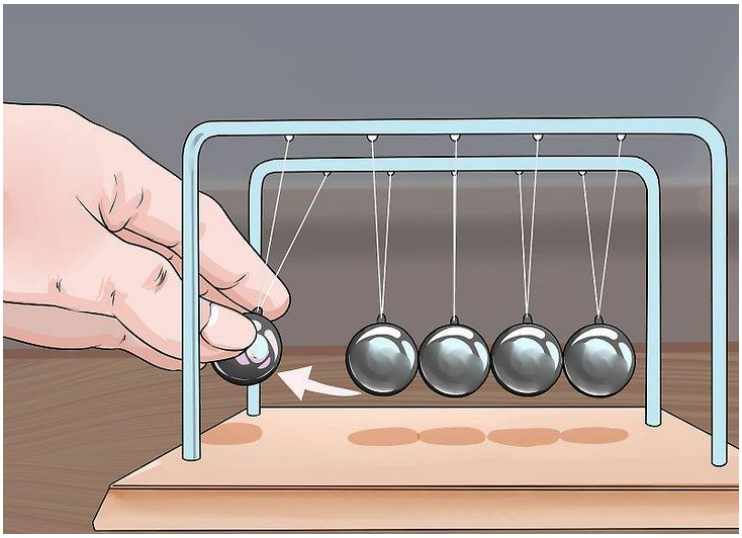

Figure 2.7: Newton's cradle

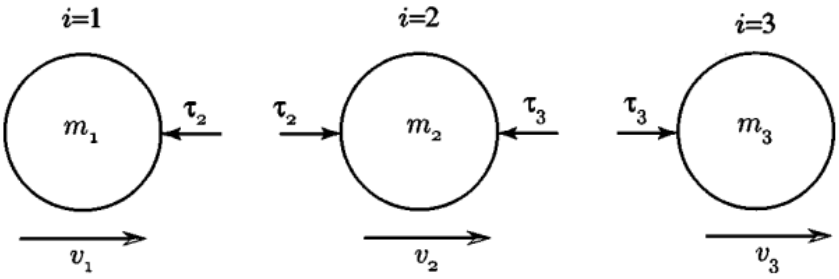

Figure 2.8: Three-ball Newton's cradle, used by Ceanga et al. [12]

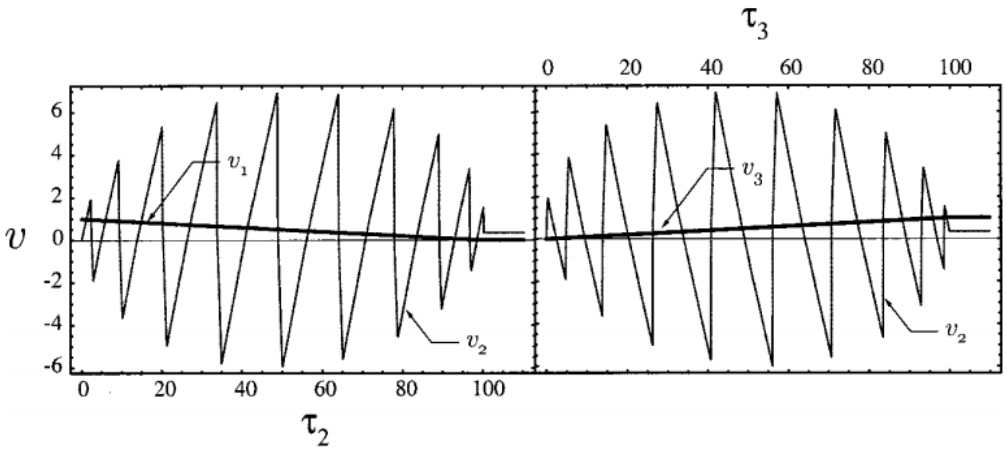

Figure 2.9: Velocity impulse diagram [12]

Ceanga et al. [12] explained a three-ball Newton's cradle, using a very small ball between two very large peripheral balls, as shown in Figure 2.8, where, *'m'* = mass, *'τ'* = impulse, *'v'*= velocity, *'i'* = order number, and the subscripts show the numbers of the objects. Figure 2.9 depicts the impulse velocity diagrams of the small ball, which introduces several micro-collisions that transmit the momentum from one incident large ball to the other large ball.

A tsunami, which can be caused by an earthquake, is an example of applying a similar principle to liquids. The tectonic plates under the earth's crust strikes and generates a shock wave under the surface of the sea, causing a tsunami wave. The height and magnitude of a tsunami are much larger than those of normal waves. The shock wave in this scenario moves differently compared with Newton's cradle. The transfer of energy among solids does not cause the deformation of shape, whereas, for liquids, shockwaves move all of the material, according to the principle of conservation of momentum, and the behaviour is the same as that observed for Newton's cradle.

In a healthy subject, the LV ejection period is 0.35 $\pm$ 0.08 ms [13] at 72 bpm and is dependent on heart rate (HR). The preload, afterload, and contractile states represent 40% of the cardiac cycle, whereas the LV relaxes for the remaining time. During each LV ejection, 70 ml of blood is pushed into the arterial system in a 70-kg, healthy subject. This push results in a tidal wave, which increases the BP to 120 mmHg during the LV relaxation period, then reduces the BP until it reaches 80 mmHg. The aorta regulates the blood flow, but the effect of the tidal wave can be observed in the arterial tree, in the shape of pulses. Continuous heartbeats result in a standing wave in the arterial tree, resulting in pulses far from the heart exerting different effects on its waveform due to the reflected waves.

The aorta follows the WK principle, which ensures that blood will flow continuously after being released in a non-continuous manner from the LV. Due to LV contraction a volume blood ejects into the aorta generates a shock wave which modulates on top of blood flow out of aorta and speed of shock incarease as the arterial system gets stiffer.

The heart works periodically; however, the speed of blood flow speed does not change in response to pulsation. The elasticity of the arterial tree generates a distension

waveform, which transforms kinetic energy into potential energy and results in the pulsation phenomenon.

Waves move faster in solids than in liquids, and the same phenomenon can be observed for arterial stiffness, in the form of PWV. A stiffer artery results in higher PWV, which eventually results in high BP.

2.6 Morphology of the Arterial Waveform

The arterial waveform contains two distinct regions, the rising edge region, called the anacrotic region, and the falling edge region, called the catacrotic region. The anacrotic region represents the systolic phase, whereas the catacrotic region represents the diastolic phase. The dicrotic notch is present in the catacrotic phase, and its position is highly reliant on the compliance of the artery, as shown in Figure 2.10.

Arterial stiffness can be determined using PWV and pulse contour analysis [14]. The myriad of bifurcations generates reflected waves and frequent anastomoses, which eventually forms a standing wave. The total reflection results in a notch, which ideally occurs in the middle of the catacrotic phase of the waveform, as it moves from systole to diastole. The reflection wave travels faster as arteries become stiffer, which can result in higher BP, as shown in Figure 2.10, which shows a comparison between normotensive and hypertensive reflected waves.

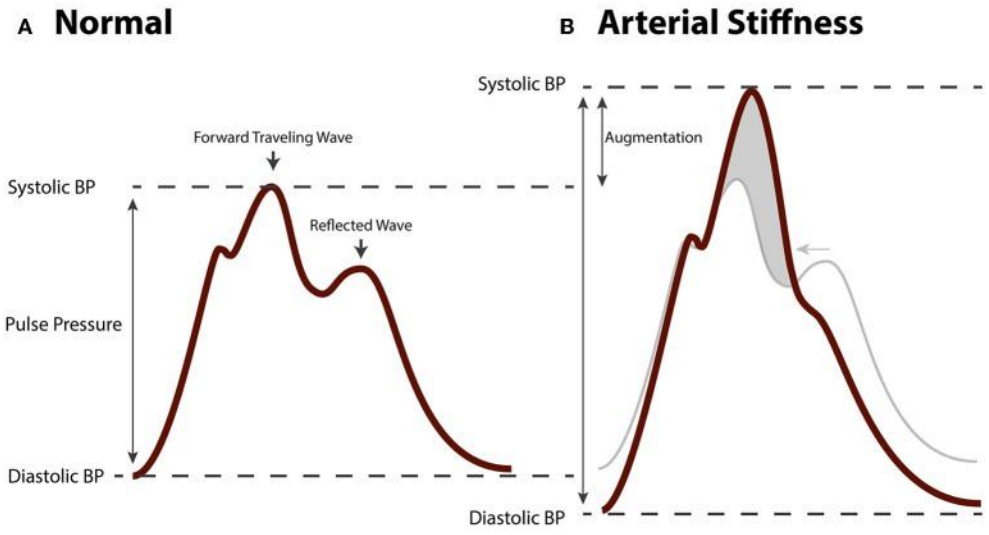

Figure 2.10: The effects of artery stiffness on reflected waves. ‘A’ is normotensive and ‘B’ is hypertensive [15]

The arterial pulse contour contains haemodynamic information [16] of prognostic value, and arterial stiffness can significantly change the morphology of the pulse contour. The relationship between the anacrotic phase of the wave and the reflected wave can be measured using the augmentation index (AIx). Both large artery stiffness and peripheral resistance cause larger wave reflections, which greatly influence the AIx [16]. A tonometric device can be used to measure the PWV and AIx and requires highly trained operators. Digital volume pulse contour analysis is an alternative to tonometric techniques, which uses the second derivative of the raw PPG waveform, which is also known as the accelerated plethysmogram (APG), to analyse the anacrotic and dicrotic notches, using mathematical remodelling. The second derivative fiducial point and derived parameters are closely associated with the distensibility of the carotid artery, age, BP, and arterial diseases [17].

2.6.1 Augmentation Index (AIx)

The AIx measures reflected wave perturbations on the systolic pressure waveform. The reflected waves moving from the peripheral artery to the central aortic artery result in the dicrotic notch. Lower artery compliance is disproportionately associated with an increase in systolic pressure, which eventually results in a higher load in the LV. AIx is measured as a ratio between systolic peak and tidal crest difference and the systolic peak and diastolic crest difference [18], as shown in Equation 2.1 and Figure 2.11.

$$AIx = \frac{pSBP_2 - DBP}{pSBP - DBP} \times 100\% \quad (2.1)$$

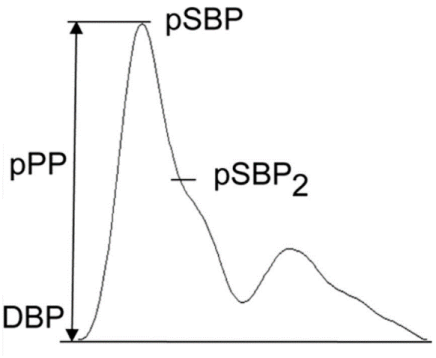

Figure 2.11: Peripheral pulse augmentation index (AIx) [18]

2.6.2 Reflectance Index

The reflectance index is defined as the temporal difference between the systolic peak and the dicrotic peak [19], as shown in Figure 2.12 and Equation 2.2.

$$RI = \Delta T \tag{2.2}$$

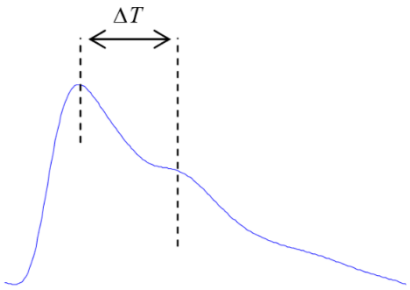

Figure 2.12: Time delay between the arterial waveform peak and the dicrotic notch [17]

2.6.3 Stiffness Index

The stiffness index is defined as the ratio between the systolic peak and dicrotic peak amplitudes [16], as shown in Figure 2.13 and Equation 2.3.

$$SI = \frac{y}{x} \tag{2.3}$$

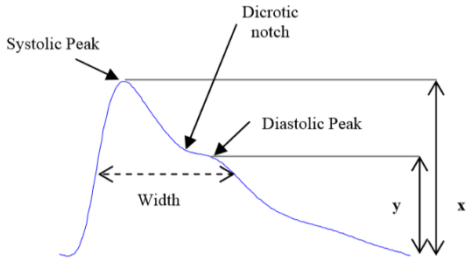

Figure 2.13: Arterial waveform and fiducial locations [17]

2.6.4 Large Artery Stiffness Index

The systolic component is caused by the pressure wave generated by the LV and morphological changes as the wave reaches the end of the organ or the distal artery. Large artery stiffness index is defined as the ratio between the systolic peak and the reflectance index, as shown in Equation 2.4.

$$SI_L = \frac{x}{\Delta T} \tag{2.4}$$

where *'x'* is the height of the pulse and 'ΔT' is the time delay, which decreases with age. The mean PWV increases with age and height [19]–[21], as shown in Figure 2.14.

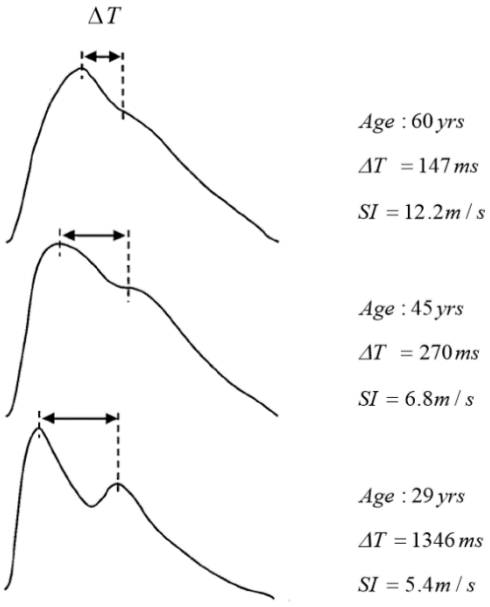

Figure 2.14: Changes in the augmentation index with changes in subjects' ages [21]

2.7 Accelerated Plethysmogram (APG)

The acquisition of PPG waveforms is simple, but the detection of the inflexion point is questionable on this waveform. Researches have used the first and second derivatives to facilitate the interpretation of the features [16], which has been quite successful. The APG analysis has roots in Eastern medicine, where the pulse has been greatly important as a diagnostic tool, and most of this work has been based in Japan. Inuma et al. [22] described the APG waveform morphologies for various subjects, as shown in Figure 2.15, which can be stratified as follows: (A) represents good blood circulation, indicating healthy subjects; (B) represents good circulation but deterioration has begun; (C) represents poor circulation, which can be caused by cold sensitivity and other factors, including atherosclerosis; (D–G) represent terrible circulation, which can be due to a variety of diseases, including cerebrovascular diseases, breast cancer, ischemia, and uterine diseases.

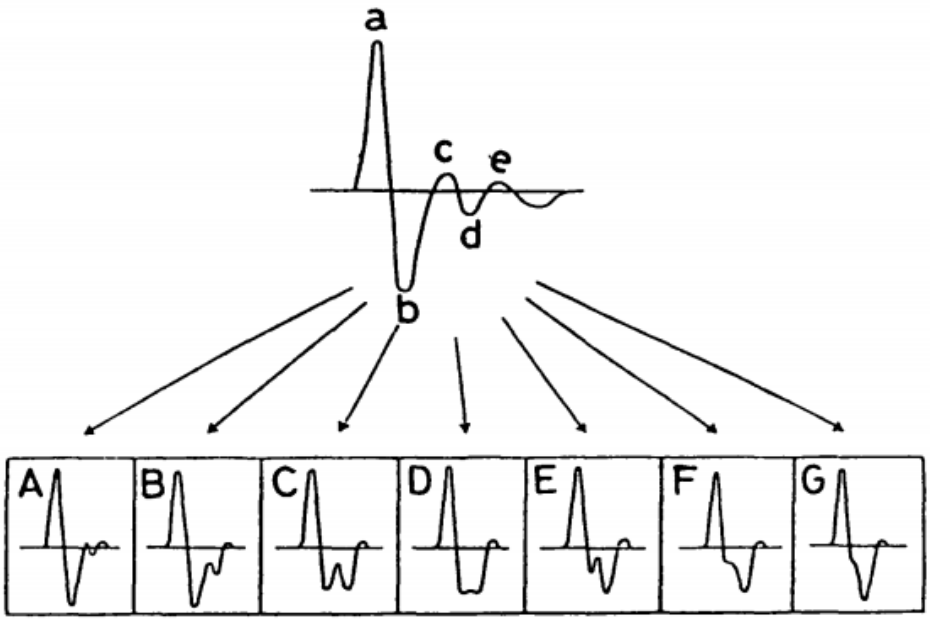

Figure 2.15: Accelerated PPG, categorised by patient categories [24]

The APG fiducial point ratio increase/decrease provides information regarding arterial stiffness [16], can be used to segregate hypertensive subjects [23], correlates with the Framingham score [25], pharmacological effects [16], left ventricle afterload [26], vascular age [27], and sympathetic response [28], and is closely related to age. The APG waveform provides information regarding blood circulation, which can be used to differentiate cerebrovascular, ischemic, and tumour-related diseases [22]. Nousou et al. [23] have developed a self-organising map system to adjust the APG peaks, to classify peaks correctly.

2.7.1 First Derivative

The first derivative is the least commonly used derivative in the literature [21] and is most often used to detect the diastolic parameter, when the first derivative is the closest derivative, or to determine the zero-crossing point. The parameter $'\Delta T'$ represents the time necessary for the pressure wave to go from the left ventricle to the peripheral artery and back to the heart, as shown in Figure 2.16, and can be calculated based on the positive to negative zero-crossing points on the first derivative.

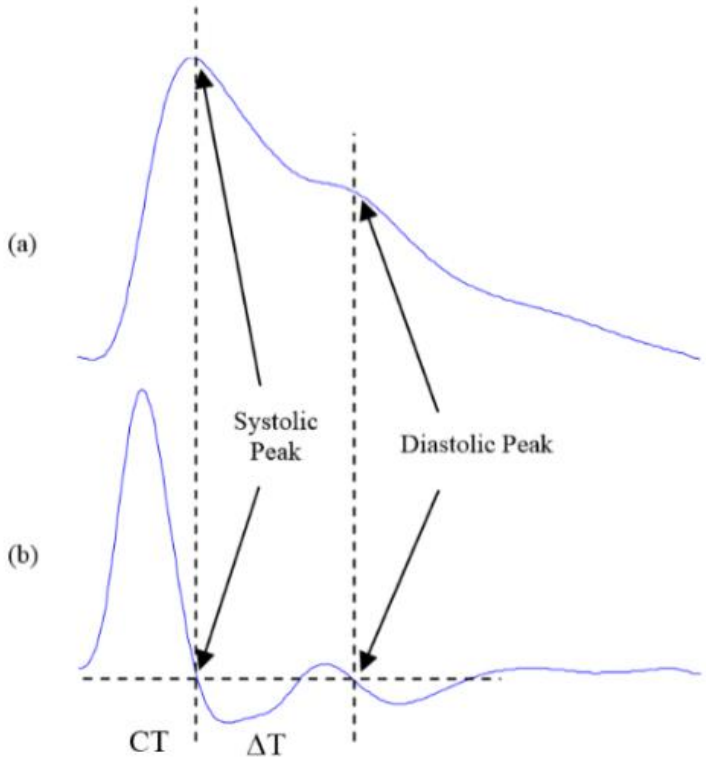

Figure 2.16: First derivative fiducial points [17]

2.7.2 Second Derivative

The second derivative of PPG is considered to be more useful for the interpretation of signal morphology. In the second derivative, four waves are in the anacrotic phase and one is in the catacrotic phase, as follows: (1) the a-wave is the early systolic positive wave; (2) the b-wave is the early systole negative wave; (3) the c-wave is the late systole re-increasing wave; (4) the d-wave is the late systole re-decreasing wave; and (5) the e-wave is the dicrotic notch [17]. The height of each wave is measured from the baseline, resulting in positive values above the baseline and negative values below the baseline, as shown in Figure 2.17.

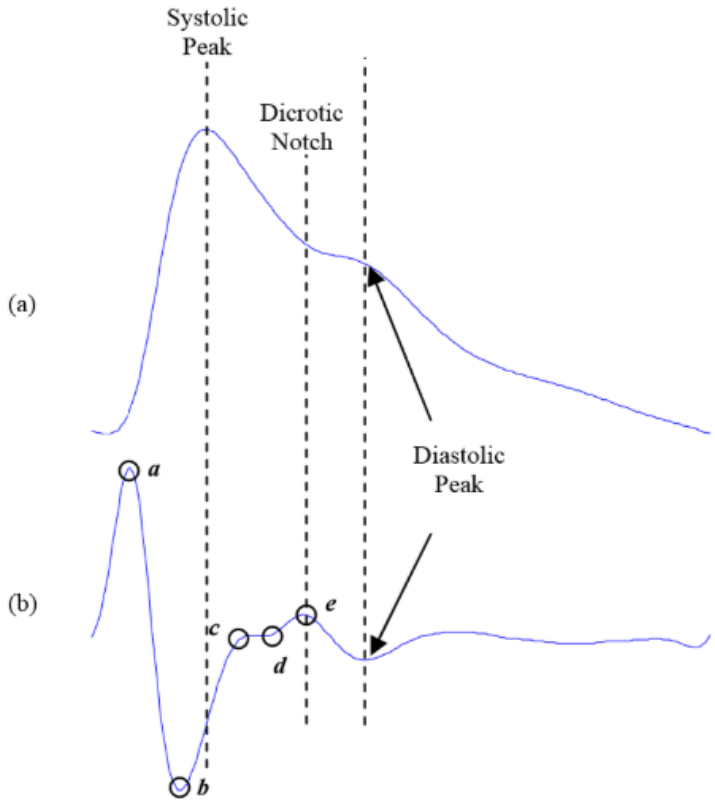

Figure 2.17: Second derivative fiducial points [17]

2.7.2.1 The Ratio of b/a

Takazawa et al. [16] stated that the b-wave to a-wave ratio increases as arterial stiffness increases and also increases with age. Imanaga et al. [29] stated that the ratio represents the local vascular distensibility, showing changes in the artery caused by distensibility diseases, such as atherosclerosis. Aiba et al. [30] showed that the negative value of this ratio decreases as exposure time to lead (metal) increases and significant changes were observed in subjects who were exposed to lead for more than five years in their respective working environments. Nousou et al. [23] were able to independently distinguish between hypertensive and healthy subjects using ratio values. Otsuka et al. [25] demonstrated that this ratio was favourably correlated with the Framingham score, which is an independent factor for predicting CVD patient. Baek et al. [26] showed that this ratio increases with age.

2.7.2.2 The Ratio of c/a

Takazawa et al. [16] showed that the c-wave to a-wave ratio decreases as arterial stiffness decreases and that it decreases with age. Nousou et al. [23] showed that this

ratio was independently able to distinguish between hypertensive and healthy subjects. Baek et al. [26] showed that this ratio decreases with increasing age.

2.7.2.3 The Ratio of d/a

Takazawa et al. [16] showed that the d-wave to a-wave ratio reflects a decrease in arterial stiffness, and Baek et al. [26] showed that this ratio decreases with age. The negative value of this ratio is useful for the evaluation of vasoactive agents in the bloodstream.

2.7.2.4 The Ratio of e/a

Takazawa et al. [16] demonstrated that the e-wave to a-wave ratio increases with decreased arterial stiffness, and Baek et al. [26] showed that this ratio decreases with increasing age.

2.7.2.5 The Ratio of (b – c – d – e)/a

Takazawa et al. [16] demonstrated that examining the ratio between the total difference among the b–e-waves and the a-wave increases with age and can be useful for describing vascular ageing, which can be used as a screening tool for atherosclerosis. Kimura et al. [27] used this ratio to measure vascular age, using a multiplicative factor of 45.5 and an additive factor of 65.9.

2.7.2.6 The Ratio of (b – e)/a

Baek et al. [26] demonstrated that even when the c-wave and d-wave are missing, the ratio comparing the difference between the b**–**e-waves and the a-wave may be able to measure vascular age. Inuma et al. [22] classified the APG, based on different levels of blood circulation, as shown in Figure 2.15, which was able to clearly define the cases examined by Baek et al. [26].

2.7.2.7 The Ratio of (c + d – b)/a

Inuma et al. [22] demonstrated that the ratio between the value calculated as the ratio between (c + d – b) wave and the a-wave can provide a comprehensive ageing index, which increases with age, especially in cases of bad blood circulation or cold sensitivity.

2.8 Pulse Transit Time

The PTT refers to the time necessary for a pressure pulse to travel between two distant points on an arterial tree. For a fixed distance, the travel time depends solely on the

arterial condition. Stiffer arteries are associated with shorter travel times for pressure pulses, and vice versa. PTT can be a difficult parameter to measure as the arterial tree can have different artery compositions at different sites. Conventionally, PTT is measured at the carotid and the femoral (C&F) arteries and has been demonstrated to be a good predictor of CVDs. The C&F PTT parameter is highly dependent on subject height and provides gives information for the aortic artery. The C&F PTT is based on a component of the arterial network, which has a mixed composition for large arteries because the measurement is taken at two sites and two different branches. The aortic arch bifurcates into branches, and the distance between the measurement sites is not directly equivalent to the distance between the measurement site and the arch. This measurement technique requires a tonometric device, with the subject in the supine posture. PTT techniques used at the distal arteries (e.g. radial and digital) use PPG and PVDF sensors [6], which are suitable for wearable applications.

2.9 Pressure-Volume Loop

PTT techniques require two sensors, at two distant positions, to acquire data. In contrast, The PU-loop method can be used to determine the PWV from a single measurement location. The most significant advantage of the PU-loop method the ability to assess arterial stiffness from a single measurement point. The single-point assessment provides a direct relationship with the arterial site, which can help assess atherosclerosis in a specific area or facilitate the assessment of a specific area both before and/or after surgery.

Using this technique, the pressure and volume waveforms are acquired simultaneously, at a single location. In traditional clinical practice, the PU-loop is measured invasively, by inserting a catheter into a carotid or femoral site. In the heart, the LV PU-loop can be measured to determine ventricle enlargement or LV hypertrophy. The PU-loop can be used to assess the arterial condition after graft surgery and bypass surgery [31].

This technique can be very suitable for wearable technology because it requires only a single location. This technique can be used for the fusion of two waveform datasets. This technique was investigated for the measurement of PWV using a non-invasive method, as explained in Chapter 5.

2.10 Heart Rate Variability

HRV has prognostic value for cardiovascular morbidity and is known to be a precursor for hypertension and other CVDs. HRV is a physiological phenomenon and describes the measure of variability between beat to beat intervals. HRV is a predictor of autonomic balance between the sympathetic and parasympathetic modulation of the HR. An increase in sympathetic activity and a decrease in the parasympathetic response are predictors of cardiac mortality [32] associated with diseases, such as myocardial infarction, stroke, and heart failure. Reduced HRV is a predictor of parameters that increase the Framingham risk score, such as hypertension, diabetes, high cholesterol, smoking, and increasing age [32].

Sympathetic activity increases HR during exercise and other exertion activities. Parasympathetic activity decreases the HR during condition such as rest and sleep. These two systems regulate the HR in circadian cycles, increasing during the day to respond to daily tasks and decreasing at night while resting or sleeping. In a healthy subject, HR changes continuously and dynamically, in addition to following circadian rhythms.

2.10.1 Time Domain

The time-domain measurement is the simplest and most useful analysis method and is the least prone to noise. This analysis quantifies the variability associated with interbeat intervals and uses statistical measurements [33]. The primary parameters are as follows:

- SDNN: Standard deviation of normal-to-normal (NN) intervals
- RMSSD: Root mean square of successive NN intervals
- NN50: Number of adjacent NN intervals that differ from each other by 50 ms
- pNN50: Proportion of adjacent NN intervals that differ from each other by 50 ms
- HR

The SDNN is the gold standard for CV risk stratification, and values below 50 ms indicate unhealthy subjects, whereas 50–100 ms indicates compromised health and above 100 ms indicates healthy subjects. Individuals with SDNN values of at least 100 ms have a 5.3-fold lower chance of heart attack than individuals with SDNN values of

50 ms or lower. NN50 and pNN50 require an epoch of 2 min. RMSSD estimates vagally mediated changes in HRV, which are a source of parasympathetic activity [34].

2.10.2 Frequency Domain

In the frequency domain analysis, the sum of the sinusoids represents the time series. The analysis measures the distribution of power in four frequency zone [33], as follows:

- Ultra-low frequency (ULF) band, ranging up to 0.003 Hz and below
- Very low frequency (VLF) band, ranging from 0.003–0.04 Hz
- Low-frequency (LF) band, ranging between 0.04–0.15 Hz
- High-frequency (HF) band, ranging between 0.15–0.4 Hz

The distribution measurement schemas are categorised as follows:

- The ratio of LF to HF power
- The power of frequency bands, in standard units
- The absolute power of the frequency band, in ms^2

The stratification methods for the frequency band can be performed using Fast Fourier transform or autoregressive modelling. Because the circadian rhythm is the primary driver of the ULF band, HRV must be recorded for 24 hr. ULF can show distinct regions associated with different psychiatric activities during a 24-hr recording. VLF is strongly correlated with causes of mortality and shows a stronger correlation then the LF and HF zones. The sympathetic activity has significant influences on the amplitude and frequency of the VLF band. LF is primarily reflected by baroreceptor activity but not by a cardiac sympathetic intervention. LF requires a minimum recording of 2 minutes for analysis. HF represents the respiratory-induced changes in HR, which can vary in neonates and adults. HF activity increases at night and is correlated with stress, anxiety, and panic-like feelings. The LF/HF ratio provides information regarding the sympathetic and parasympathetic activity ratio.

2.10.3 Nonlinear Domain

The nonlinear domain analysis quantifies the unpredictability of the interbeat interval time series, and the non-linear domain parameters are as follows [33]:

- Poincaré plot standard deviation perpendicular to the line of identity (SD1)
- Poincaré plot standard deviation along the line of identity (SD2)

- The ratio of SD1 to SD2
- Sample entropy, which measures the regularity and complexity of a time series
- Approximate entropy, which measures the regularity and complexity of a time series

The nonlinearity analysis correlates the frequency and time domain measurements when they result from the same processes, such as post-myocardial infarction. A Poincare plot is a scatter plot of the distance between an R-R interval to its previous interval. SD1 predicts DBP and the difference in HR and requires 5 min of HRV recording. SD2 reflects the baroreflex sensitivity and can be calculated based on either short-term or long-term HRV recordings. SD1/SD2 provides similar information to LF/HF, with the assumption that LF is the result of sympathetic activity and HF is the result of parasympathetic activity. Sample entropy provides a less-biased single regularity and complexity compared with the time series. In contrast, approximate entropy provides a similar single regularity and complexity as a time series.

2.10.4 Time-Frequency Analysis

The time-frequency analysis provides the temporal evolution of the spectrum, allowing time and frequency information to be viewed simultaneously [33]. The autoregressive Lomb-Scargale periodogram and wavelet transforms to calculate the spectrogram. The same parameters used in the frequency domain analysis are used, such as the peaks and percentages of ULF, VLF, LF, and HF bands.

In the windowed-periodogram method, larger windows are separated into smaller windows, which can be overlapping, to determine power spectral density (PSD). The two-dimensional plotting of the PSD along the time and frequency axis produces a spectrogram. A continuous wavelet transform is a useful tool for the time-frequency analysis on smaller-windowed periodograms.

2.11 Sensing Methodologies

2.11.1 Photoplethysmogram - PPG

The word plethysmogram is a combination of two Greek words, ‘plethysmos’, meaning increase, and ‘gram’, meaning writing [35]–[37]. Over the last century, plethysmograms have evolved, and different variants measure variations in blood flow volumes, using water- [38]–[42], air- [43], [44], or mercury-filled [45]–[50] cuffs, which

are strapped to an organ. With the advent of the digital era, techniques have evolved to include impedance- [51]–[53] and photovoltaic-based [54]–[65] blood flow measurements. In 1938, Hertzman discovered a relationship between backscattered light and volumetric blood flow, a phenomenon known as PPG [9]. PPG consists of a photovoltaic sensor [36], which measures changes in volumetric blood flow in the microvascular bed of tissues against incident light. PPG devices show high sensitivity, reliability, and reproducibility. They are easy to use, simple to set up, convenient, and economical, representing a non-invasive and less intrusive form of sensor. PPG devices have been widespread in clinical practice, on an everyday basis, in primary and intensive health care units, to measure blood oximetry and HR.

PPG waveforms are morphologically similar to BP waveforms, providing vital insights into the cardiovascular system. Skin, bone, pigment, and arterial and venous blood flow absorb incident light, which can be measured using two methods. In the transmissive method [6], the source of light is within the line of sight of the receiver. In the reflective method [23], [29], [36], the source of light illuminates the area, and the bone reflects the light to the receivers.

The waveform consists of an alternating current (AC) component and a direct current (DC) component, as shown in Figure 2.18. The AC component is the result of volumetric changes in the pulsating blood flow through an artery, in which the main component of light is absorbed by haemoglobin [66]. The DC component depends on the tissue's average blood volume in the arteries and veins, skin, bone, and other tissues. The waveform provides vital biomarker information regarding arterial blood flow and HR.

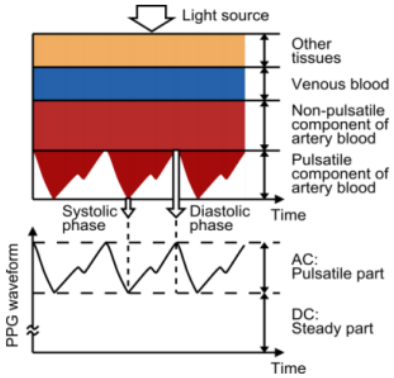

Figure 2.18: Wearable Photoplethysmography Sensors - Past and Present [67]

PPG sensing follows the Beer-Lambert–Bouguer law [68]:

$$I(\lambda) = I_0 \exp\left[-\mu_a(\lambda)cd\right] \tag{2.5}$$

where $'I(\lambda)'$ is the intensity of light (lux), $'I_0'$ is the intensity of incident light (lux), $'\lambda'$ is the source wavelength (cm), $'\mu_a'$ is the extinction coefficient or absorptivity of the substance (L/mmol*cm), *'c'* is the concentration of the absorbing substance, which is constant in the medium (mmol/L), and *'d'* is the optical path length of the medium (cm).

The skin consists of the epidermis, dermis, and subcutaneous tissue layers, which contain capillaries, arterioles, and arteries. The penetration depth of the light source depends on the wavelength of the source. Commonly used light source wavelengths include 440 nm (green), 660 nm (red), and 960 nm [infrared (IR)] [35], [36], [67], [69]–[72], and the penetration depth increases as the wavelength increases, from 300 nm to 1,100 nm. The augmented depth for wavelengths and skin layers are shown in Figure 2.19. The IR wavelength is less sensitive to oxygenation in the blood and produces a more stable signal [35]. The IR wavelength is most commonly used for cuffless BP estimations.

The contact pressure of the sensor considerably changes the waveform and derives information [73]. Contact pressure is required to increase the amplitude, which is relative to the wavelength, and is pronounced in shorter wavelengths [67], [71], [74]–[76]. Reduced pressure avoids discomfort and tissue damage.

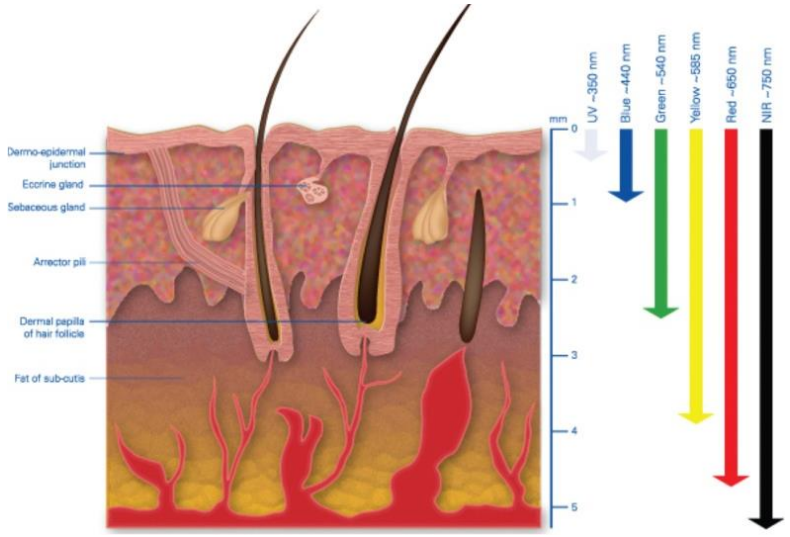

Figure 2.19: A schematic diagram of the finger layers and the penetration depth of the light source [77]

2.11.2 Ballistic Pulse Pressure – BPP

Volume changes in the limbs have been important for clinical and physiological assessments. Limb girth variations are due to arterial blood flow waveform which is directly proportional to a pressure wave in the blood flow stream. The systolic amplitude is directly proportional to vascular distensibility [81].

This mechanical distortion, which is caused by arterial distension, has been the focus of research since the late 18th century. The methods devised by Schafer et al. [78], and then adapted by Ahlborh et al. [79], used a rigid fluid-filled jacket that was strapped around the limb and attached to a scale, to allow the changes in the enclosed limb volume or the distension waveform to be observed. In 1949, mercury in a rubber resistance strain gauge was used to measure the girth of the limb. A representative system, consisting of two gauges strapped around the limb, is shown in Figure 2.20.

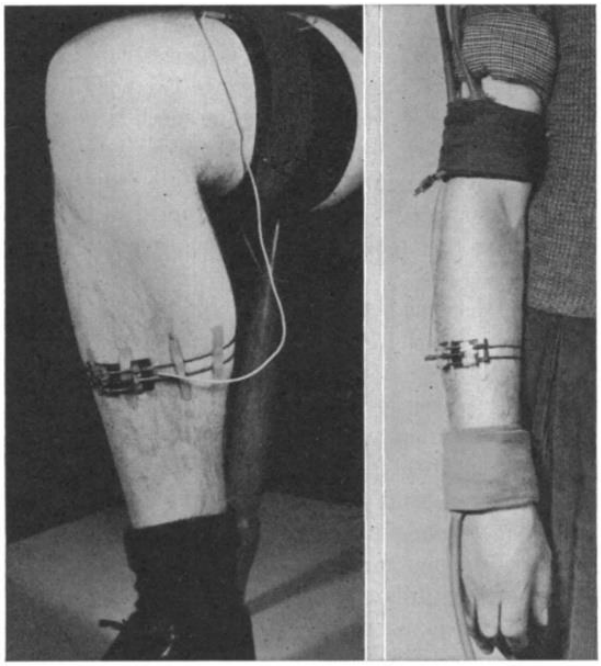

Figure 2.20: Resistive gauges strapped on limbs [80]

The piezoelectric sensor is a piecewise, continuous electromechanical sensor that measures changes in mechanical displacement/pressure and produces a change in the electrical form. Lee et al. [83] formulated the classical equation for a thin laminate, with a piezoelectric effect. On a thin laminate, the displacement is characterised by geometric deformation, as shown in Figure 2.21.

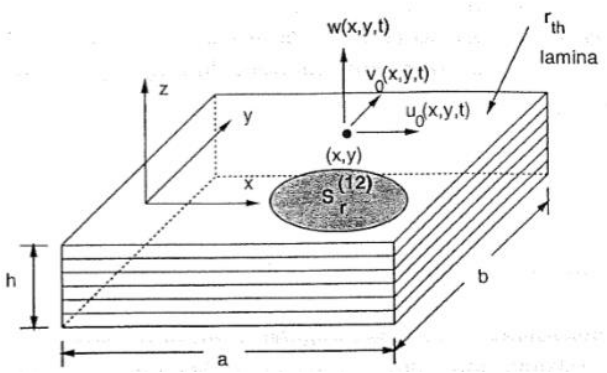

Figure 2.21: Laminated model of a composite plate with an electrode surface [84]

In Figure 2.21, $'u_0'$ is the displacement in the x-axis, 'v_0' is the displacement in the y-axis, and *'a'* is the length and *'b'* is the width of the sensor, which is negligible compared to the orthogonal axis deflection, *'w'*, in the z-axis. The deformation produces a charge $'q_r(t)'$ [83], defined as follows:

$$q_r(t) = -\bar{z}_r \int_0^a \int_0^b \{F(x,y)P_0(x,y)L_p[w(x,y,t)]\}_r dx\, dy \qquad (2.6)$$

$$(r = 1,2, \dots \dots \dots \dots N)$$

where

$$L_p = e_{31}^0 \frac{\partial^2}{\partial x^2} + e_{32}^0 \frac{\partial^2}{\partial y^2} + 2e_{36}^0 \frac{\partial^2}{\partial x \partial y} \qquad (2.7)$$

$$F_r(x,y) = \begin{cases} 1 & if(x,y)\ is\ within\ the\ rth\ sensor\ coverage \\ 0 & otherwise \end{cases} \qquad (2.8)$$

where $'e_{31}^0{}', 'e_{32}^0{}', and\ 'e_{36}^0'$ are piezoelectric [(charge/area)/strain] constants, $'P_0(x,y)'$ is directional polarity, $'\bar{z}_r'$ is the distance from the geometric centre of the *'rth'* sensor, and *'N'* is the number of piezoelectric sensors [84].

The waveform that is measured by a piezoelectric sensor is the BPP waveform. The BPP waveform contains information regarding arterial diameter changes caused by a pressure wave [82]. BPP measures the distention waveform, which is the result of transmural pressure on the elastic boundaries of the artery.

BPP sensing follows the Kessel formula [66], which is stated as follows:

$$\sigma = p_i \frac{r}{s} \quad \text{r>>s} \tag{2.9}$$

where $'\sigma'$ is circumferential tension (Pa), $'p_i'$ is internal pressure (Pa), *'r'* is the vessel radius (m), and *'s'* is wall thickness (m).

BPP is related to the distension waveform according to Hooke's Law, which is stated as:

$$\sigma = E.\epsilon \tag{2.10}$$

where '*E'* is the elastic modulus (N/m^2) and $'\epsilon'$ is the strain (dimensionless).

The effects of arteriosclerosis, aortic stenosis, and aortic insufficiency have been exemplified by the use of a piezoelectric PVDF sensor at the radial artery [82], as shown in Figure 2.22.

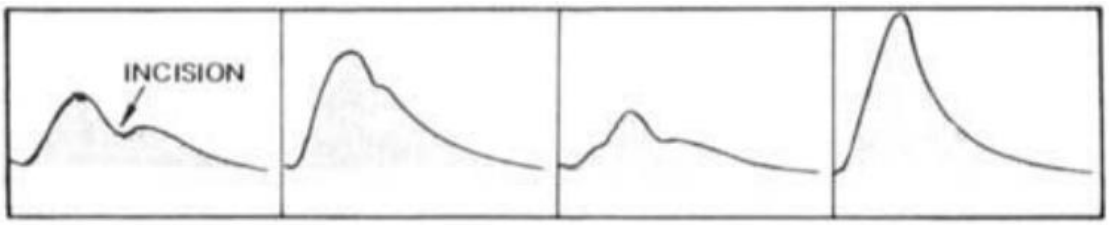

Figure 2.22: Normal (Left to right), arteriosclerosis, aortic stenosis, and aortic insufficiency waveforms recorded using a piezoelectric sensor [82]

2.12 Summary

This chapter provides a background of cardiovascular mechanics, which are very important to fully understand and extract information from an arterial waveform. Blood flow originates from the heart, moving through the arterial tree, and back into the heart, in a closed-loop system. Then, the arterial tree affects the blood flow waveform, based on changes in arterial composition and area. The WK phenomenon in the arterial tree explains the slow fall in aortic pressure compared with the ejection of blood flow from the LV. The WK model reduces the load on the heart and the end organs, which is very important for the cardiovascular system. Then, the principle of PWV was explained, the most important phenomenon necessary to understand the stability of blood flow in a closed-loop, pulsating system. PWV represents the oldest method for the measurement of arterial stiffness, which measures speed, based on an Eulerian frame of reference. The importance of arterial waveform morphologies and their related stiffness indexes were described, which are indicators of the severe effects on

the cardiovascular system caused by arterial stiffness. Next, the APG analysis was described, which is a state-of-the-art signal-processing method that can extract hidden information from an arterial waveform. APG indexes can quantify arterial stiffness and predict adverse effects. This chapter also developed the background of HRV, PTT, and the PU-loop, which are key methods for the validation of arterial waveforms because of their trackability, consistency, and fusion across the different morphologies. Finally, the working principles of PPG and BPP sensors, which are the sensors under comparison, were described, including their sensing methodologies and associated waveforms. The BPP sensor was compared against the state-of-the-art PPG sensor and validated against the HRV, PTT, and PU-loop techniques, based on existing gold-standard measurement methods, in this study, which is described in later chapters.

2.13 References

[1] J. M. Guccione, G. S. Kassab, and M. B. Ratcliffe, Eds., Computational Cardiovascular Mechanics. Boston, MA: Springer US, 2010.

[2] F. N. Van De Vosse and M. E. H. Van Dongen, Cardiovascular Fluid Mechanics lecture notes. Technische Universiteit Eindhoven, 1998.

[3] M. R. Imam, “Analysis of beat-to-beat ventricular repolarization duration variability from electrocardiogram signal,” Ph.D. Thesis, Department of Electrical and Electronic Engineering, The University of Melbourne Australia, 2015.

[4] M. J. Loe and W. D. Edwards, “A light-hearted look at a lion-hearted organ (or, a perspective from three standard deviations beyond the norm) Part 1 (of two parts),” Cardiovasc. Pathol., vol. 13, no. 5, pp. 282–292, Sep. 2004.

[5] A. J. Bank, H. Wang, J. E. Holte, K. Mullen, R. Shammas, and S. H. Kubo, “Contribution of Collagen, Elastin, and Smooth Muscle to In Vivo Human Brachial Artery Wall Stress and Elastic Modulus,” Circulation, vol. 94, no. 12, pp. 3263–3270, Dec. 1996.

[6] R. Mukkamala, “Towards Ubiquitous Blood Pressure Monitoring via Pulse Transit Time: Theory and Practice,” IEEE Trans Biomed Eng., vol. 62, no. 8, pp. 1879–1901, Aug. 2015.

[7] J. T. Ottesen, M. S. Olufsen, J. K. Larsen, and Society for Industrial and Applied Mathematics., Applied mathematical models in human physiology. Society for Industrial and Applied Mathematics (SIAM, 3600 Market Street, Floor 6, Philadelphia, PA 19104), 2004.

[8] W. Leeah, "The Cardiovascular System" Anatomy and Physiology. Open Oregon State, Oregon State University, 2020.

[9] J. G. Betts, "The cardiovascular system. Blood vessels and circulation", Anatomy and physiology, Houston, Texas : OpenStax College, Rice University, 2017 .

[10] N. Westerhof, J.-W. Lankhaar, and B. E. Westerhof, “The arterial Windkessel,” Med. Biol. Eng. Comput., vol. 47, no. 2, pp. 131–141, Feb. 2009.

[11] M. F. O'Rourke, R. P. Kelly, and A. P. (Alberto P. . Avolio, The arterial pulse. Lea & Febiger, 1992.

[12] V. Ceanga and Y. Hurmuzlu, "A New Look at an Old Problem: Newton's Cradle," J. Appl. Mech., vol. 68, no. 4, p. 575, Jul. 2001.

[13] N. Kolev and M. Zimpfer, "Left ventricular ejection time and end-systolic pressure revisited.," Anesth. Analg., vol. 81, no. 4, pp. 889–90, Oct. 1995.

[14] E. von Wowern, G. Östling, P. M. Nilsson, and P. Olofsson, "Digital Photoplethysmography for Assessment of Arterial Stiffness: Repeatability and Comparison with Applanation Tonometry," PLoS One, vol. 10, no. 8, p. e0135659, Aug. 2015.

[15] B. J. van Varik, R. J. M. W. Rennenberg, C. P. Reutelingsperger, A. A. Kroon, P. W. de Leeuw, and L. J. Schurgers, "Mechanisms of arterial remodeling: lessons from genetic diseases," Front. Genet., vol. 3, p. 290, 2012.

[16] K. Takazawa, "Assessment of vasoactive agents and vascular aging by the second derivative of photoplethysmogram waveform.," Hypertens. (Dallas, Tex. 1979), vol. 32, no. 2, pp. 365–70, Aug. 1998.

[17] M. Elgendi, "On the analysis of fingertip photoplethysmogram signals.," Curr. Cardiol. Rev., vol. 8, no. 1, pp. 14–25, Feb. 2012.

[18] S. Munir, "Peripheral Augmentation Index Defines the Relationship Between Central and Peripheral Pulse Pressure," Hypertension, vol. 51, no. 1, pp. 112–118, Jan. 2008.

[19] J. M. Padilla, E. J. Berjano, J. Saiz, L. Facila, "Assessment of relationships between blood pressure, pulse wave velocity and digital volume pulse," Computers in Cardiology, 2006.

[20] U. Rubins, A. Grabovskis, J. Grube, and I. Kukulis, "Photoplethysmography Analysis of Artery Properties in Patients with Cardiovascular Diseases," Springer, Berlin, Heidelberg, pp. 319–322, 2008.

[21] S. C. Millasseau, R. P. Kelly, J. M. Ritter, and P. J. Chowienczyk, "Determination of age-related increases in large artery stiffness by digital pulse contour

analysis.," Clin. Sci. (Lond)., vol. 103, no. 4, pp. 371–7, Oct. 2002.

[22] J. Inuma, "Relationship between acceleration plethysmography and aortic calcification index in chronic kidney disease patients," Hong Kong J. Nephrol., vol. 14, no. 2, pp. 48–53, Oct. 2012.

[23] N. Nousou, S. Urase, Y. Maniwa, K. Fujimura, and Y. Fukui, "Classification of Acceleration Plethysmogram Using Self-Organizing Map," in 2006 International Symposium on Intelligent Signal Processing and Communications, pp. 681–684, 2006.

[24] S. Homma, S. Ito, T. Koto, and H. Ikegami, "Relationship between accelerated plethysmogram blood pressure and arteriolar elasticity," Japanese J. Phys. Fit. Sport. Med., vol. 41, no. 1, pp. 98–107, Mar. 1992.

[25] T. Otsuka, T. Kawada, M. Katsumata, and C. Ibuki, "Utility of second derivative of the finger photoplethysmogram for the estimation of the risk of coronary heart disease in the general population.," Circ. J., vol. 70, no. 3, pp. 304–10, Mar. 2006.

[26] H. J. Baek, J. S. Kim, Y. S. Kim, H. B. Lee, and K. S. Park, "Second Derivative of Photoplethysmography for Estimating Vascular Aging," in 2007 6th International Special Topic Conference on Information Technology Applications in Biomedicine, 2007, pp. 70–72.

[27] Y. Kimura, "Kampo therapy for premenstrual syndrome: Efficacy of Kamishoyosan quantified using the second derivative of the fingertip photoplethysmogram," J. Obstet. Gynaecol. Res., vol. 33, no. 3, pp. 325–332, Jun. 2007.

[28] T. Ushiroyama, Y. Kajimoto, K. Sakuma, and M. Ueki, "Assessment of chilly sensation in Japanese women with Laser Doppler Fluxmetry and Acceleration Plethysmogram with respect to peripheral circulation," Bulletin of the Osaka Medical College, vol. 51(2), 2005.

[29] I. Imanaga, H. Hara, S. Koyanagi, and K. Tanaka, "Correlation between wave components of the second derivative of plethysmogram and arterial distensibility," Jpn. Heart J., vol. 39, no. 6, pp. 775–84, Nov. 1998.

[30] Y. Aiba, “Peripheral hemodynamics evaluated by acceleration plethysmography in workers exposed to lead.,” Ind. Health, vol. 37, no. 1, pp. 3–8, Jan. 1999.

[31] K. H. Parker, “An introduction to wave intensity analysis,” Med. Biol. Eng. Comput., vol. 47, no. 2, pp. 175–188, Feb. 2009.

[32] C. S. Yoo, K. Lee, S. H. Yi, J.-S. Kim, and H.-C. Kim, “Association of heart rate variability with the framingham risk score in healthy adults.,” Korean J. Fam. Med., vol. 32, no. 6, pp. 334–40, Sep. 2011.

[33] F. Shaffer and J. P. Ginsberg, “An Overview of Heart Rate Variability Metrics and Norms.,” Front. public Heal., vol. 5, p. 258, 2017.

[34] R. E. Kleiger, J. P. Miller, J. T. Bigger, and A. J. Moss, “Decreased heart rate variability and its association with increased mortality after acute myocardial infarction.,” Am. J. Cardiol., vol. 59, no. 4, pp. 256–62, Feb. 1987.

[35] K. H. Shelley, “Photoplethysmography: Beyond the Calculation of Arterial Oxygen Saturation and Heart Rate,” Anesth. Analg., vol. 105, no. On Line Suppl., pp. S31–S36, Dec. 2007.

[36] J. Allen, “Photoplethysmography and its application in clinical physiological measurement.,” Physiol. Meas., vol. 28, no. 3, pp. R1–R39, Mar. 2007.

[37] M. E. Alnaeb, N. Alobaid, A. M. Seifalian, D. P. Mikhailidis, and G. Hamilton, “Optical techniques in the assessment of peripheral arterial disease.,” Curr. Vasc. Pharmacol., vol. 5, no. 1, pp. 53–9, Jan. 2007.

[38] N. Unno, K. Inuzuka, H. Mitsuoka, K. Ishimaru, D. Sagara, and H. Konno, “Automated Bedside Measurement of Penile Blood Flow Using Pulse-Volume Plethysmography,” Surg. Today, vol. 36, no. 3, pp. 257–261, Feb. 2006.

[39] P. Lavoisier, R. Barbe, and M. Gally, “Validation of a continuous penile blood-flow measurement by pulse-volume-plethysmography,” Int. J. Impot. Res., vol. 14, no. 2, pp. 116–120, Apr. 2002.

[40] Y. Kawakami, H. A. Menkes, and A. B. DuBois, “A water-filled body plethymograph for the measurement of pulmonary capillary blood flow during changes of intrathoracic pressure.,” J. Clin. Invest., vol. 49, no. 6, pp. 1237–51,

Jun. 1970.

[41] R. W. Hyde, “Cowbird Research and Measuring Pulsatile Diffusing Capacity,” Am. J. Respir. Crit. Care Med., vol. 165, no. 6, pp. 755–756, Mar. 2002.

[42] D. Horwitz and D. J. Patel, “Maximal hand blood flow in hypertensive and normal subjects.,” Am. J. Cardiol., vol. 55, no. 4, pp. 418–22, Feb. 1985.

[43] E. Criado, M. A. Farber, W. A. Marston, P. F. Daniel, C. B. Burnham, and B. A. Keagy, “The role of air plethysmography in the diagnosis of chronic venous insufficiency.,” J. Vasc. Surg., vol. 27, no. 4, pp. 660–70, Apr. 1998.

[44] M. S. Weingarten, M. Czeredarczuk, S. Scovell, C. C. Branas, G. M. Mignogna, and C. C. Wolferth, “A correlation of air plethysmography and color-flow-assisted duplex scanning in the quantification of chronic venous insufficiency.,” J. Vasc. Surg., vol. 24, no. 5, pp. 750–4, Nov. 1996.

[45] M. T. DeSanctis, M. R. Cesarone, L. Incandela, G. Belcaro, and G. Acerbi, “Methods of Evaluation and Quantification of Microangiopathy in High Perfusion Microangiopathy (Chronic Venous Insufficiency and Diabetic Microangiopathy),” J. Cardiovasc. Pharmacol. Ther., vol. 7, no. 1_suppl, pp. S3–S6, Mar. 2002.

[46] D. Rimaud, C. Boissier, and P. Calmels, “Evaluation of the effects of compression stockings using venous plethysmography in persons with spinal cord injury.,” J. Spinal Cord Med., vol. 31, no. 2, pp. 202–7, 2008.

[47] A. N. Nicolaides, Cardiovascular Disease Educational and Research Trust, European Society of Vascular Surgery,The International Angiology Scientific Activity Congress Organization, International Union of Angiology, and Union Internationale de Phlebologie at the Abbaye des Vaux de Cernay, “Investigation of chronic venous insufficiency: A consensus statement (France, March 5-9, 1997).,” Circulation, vol. 102, no. 20, pp. E126-63, Nov. 2000.

[48] E. Mannarino, L. Pasqualini, M. Menna, G. Maragoni, and U. Orlandi, “Effects of Physical Training on Peripheral Vascular Disease: A Controlled Study,” Angiology, vol. 40, no. 1, pp. 5–10, Jan. 1989.

[49] N. A. Maskell, S. Cooke, D. J. Meecham Jones, J. G. Prior, and R. J. A. Butland,

"The use of automated strain gauge plethysmography in the diagnosis of deep vein thrombosis," Br. J. Radiol., vol. 75, no. 896, pp. 648–651, Aug. 2002.

[50] S. Croal, J. Birkmyre, M. McNally, C. Hamilton, and R. Mollan, "Strain gauge plethysmography for the detection of deep venous thrombosis.," J. Biomed. Eng., vol. 15, no. 2, pp. 135–9, Mar. 1993.

[51] K. Costeloe and P. Rolfe, "Continuous Limb Blood Flow Estimation in the Newborn Using Electrical Impedance Plethysmography," Pediatr. Res., vol. 14, no. 9, pp. 1053–1060, Sep. 1980.

[52] J. Nyboer, P. Murray, and J. A. Sedensky, "Blood-flow indices in amputee and control limbs by mutual electrical impedance plethysmography.," Am. Heart J., vol. 87, no. 6, pp. 704–10, Jun. 1974.

[53] H. C. Lukaski, P. E. Johnson, W. W. Bolonchuk, and G. I. Lykken, "Assessment of fat-free mass using bioelectrical impedance measurements of the human body," Am. J. Clin. Nutr., vol. 41, no. 4, pp. 810–817, 1985.

[54] K. Nakajima, T. Tamura, and H. Miike, "Monitoring of heart and respiratory rates by photoplethysmography using a digital filtering technique.," Med. Eng. Phys., vol. 18, no. 5, pp. 365–72, Jul. 1996.

[55] A. B. Hertzman., "Observations on the finger volume pulse recorded photoelectrically," Am. J. Physiol., vol. 119, pp. 334–335, 1937.

[56] D. T. Ubbink, "Toe Blood Pressure Measurements in Patients Suspected of Leg Ischaemia: A New Laser Doppler Device Compared with Photoplethysmography," Eur. J. Vasc. Endovasc. Surg., vol. 27, no. 6, pp. 629–634, Jun. 2004.

[57] C. Butter, "Cardiac resynchronization therapy optimization by finger plethysmography," Hear. Rhythm, vol. 1, no. 5, pp. 568–575, Nov. 2004.

[58] A. D. Foster, C. Neumann, and E. A. Rovenstine, "Peripheral circulation during anesthesia, shock and hemorrhage; the digital plethysmograph as a clinical guide," Anesthesiology, vol. 6, no. 3, pp. 246–257, May 1945.

[59] M. L. Evans and L. A. Geddes, "An assessment of blood vessel vasoactivity

using photoplethysmography.," Med. Instrum., vol. 22, no. 1, pp. 29–32, Feb. 1988.

[60] D. J. Moore, T. Maher, V. Kingston, and G. Shanik, "Assessment of venous function using photoplethysmography," Ir. J. Med. Sci., vol. 151, no. 1, pp. 308–312, Dec. 1982.

[61] B. Jönsson, C. Laurent, M. Eneling, T. Skau, and L.-G. Lindberg, "Automatic Ankle Pressure Measurements Using PPG in Ankle-brachial Pressure Index Determination," Eur. J. Vasc. Endovasc. Surg., vol. 30, no. 4, pp. 395–401, Oct. 2005.

[62] A. A. Lawrence, E. M. Latty, M. L. Chivers, and J. M. Bailey, "Measurement of Sexual Arousal in Postoperative Male-to-Female Transsexuals Using Vaginal Photoplethysmography," Arch. Sex. Behav., vol. 34, no. 2, pp. 135–145, Apr. 2005.

[63] T. A. Lees and D. Lambert, "Patterns of venous reflux in limbs with skin changes associated with chronic venous insufficiency.," Br. J. Surg., vol. 80, no. 6, pp. 725–8, Jun. 1993.

[64] M. Hahn, "Local Cold Exposure Test with a New Arterial Photoplethysmographic Sensor in Healthy Controls and Patients with Secondary Raynaud's Phenomenon," Microvasc. Res., vol. 57, no. 2, pp. 187–198, Mar. 1999.

[65] M. Hirai, "Cold sensitivity of the hand in arterial occlusive disease.," Surgery, vol. 85, no. 2, pp. 140–6, Feb. 1979.

[66] J. G. Webster, Design of pulse oximeters. Institute of Physics Pub, 1997.

[67] T. Tamura et al., "Wearable Photoplethysmographic Sensors—Past and Present," Electronics, vol. 3, no. 2, pp. 282–302, Apr. 2014.

[68] S. Hu, V. Azorin-Peris, and J. Zheng, "Opto-physiological modeling applied to photoplethysmographic cardiovascular assessment.," J. Healthc. Eng., vol. 4, no. 4, pp. 505–28, 2013.

[69] R. R. Anderson and J. A. Parrish, "The Optics of Human Skin," J. Invest. Dermatol., vol. 77, no. 1, pp. 13–19, Jul. 1981.

[70] J. Jihyoung Lee, K. Matsumura, K. Yamakoshi, P. Rolfe, S. Tanaka, and T. Yamakoshi, “Comparison between red, green and blue light reflection photoplethysmography for heart rate monitoring during motion,” in 2013 35th Annual International Conference of the IEEE Engineering in Medicine and Biology Society (EMBC), vol. 2013, pp. 1724–1727, 2013.

[71] J. Spigulis, L. Gailite, A. Lihachev, and R. Erts, “Simultaneous recording of skin blood pulsations at different vascular depths by multiwavelength photoplethysmography,” Appl. Opt., vol. 46, no. 10, p. 1754, Apr. 2007.

[72] W. Cui, L. E. Ostrander, and B. Y. Lee, “In vivo reflectance of blood and tissue as a function of light wavelength,” IEEE Trans. Biomed. Eng., vol. 37, no. 6, pp. 632–639, Jun. 1990.

[73] Y. Maeda, M. Sekine, and T. Tamura, “Relationship Between Measurement Site and Motion Artifacts in Wearable Reflected Photoplethysmography,” J. Med. Syst., vol. 35, no. 5, pp. 969–976, Oct. 2011.

[74] A. Reisner, P. A. Shaltis, D. McCombie, and H. H. Asada, “Utility of the Photoplethysmogram in Circulatory Monitoring,” Anesthesiology, vol. 108, no. 5, pp. 950–958, May 2008.

[75] K. H. Shelley, D. Tamai, D. Jablonka, M. Gesquiere, R. G. Stout, and D. G. Silverman, “The Effect of Venous Pulsation on the Forehead Pulse Oximeter Wave Form as a Possible Source of Error in Spo2 Calculation,” Anesth. Analg., vol. 100, no. 3, pp. 743–747, Mar. 2005.

[76] A. C. M. Dassel, R. Graaff, M. Sikkema, A. Meijer, W. G. Zijlstra, and J. G. Aarnoudse, “Reflectance pulse oximetry at the forehead improves by pressure on the probe,” J. Clin. Monit., vol. 11, no. 4, pp. 237–244, Jul. 1995.

[77] C. Ash, M. Dubec, K. Donne, and T. Bashford, “Effect of wavelength and beam width on penetration in light-tissue interaction using computational methods,” Lasers Med. Sci., vol. 32, no. 8, pp. 1909–1918, Nov. 2017.

[78] E. A. Schäfer and B. Moore, “On the Contractility and Innervation of the Spleen.,” J. Physiol., vol. 20, no. 1, pp. 1–50, Jun. 1896.

[79] G. Ahlborg and M. Jensen-Urstad, “Arm blood flow at rest and during arm exercise,” J. Appl. Physiol., vol. 70, no. 2, pp. 928–933, Feb. 1991.

[80] R. J. Whitney, “The measurement of volume changes in human limbs.,” J. Physiol., vol. 121, no. 1, pp. 1–27, Jul. 1953.

[81] J. C. Dorlas and J. A. Nijboer, “Photo-electric plethysmography as a monitoring device in anaesthesia. Application and interpretation.,” Br. J. Anaesth., vol. 57, no. 5, pp. 524–30, May 1985.

[82] W. Nitsche and R. Thunker, “Application of the piezo-electric effect in measuring the arterial pressure pulse,” Ferroelectrics, vol. 75, no. 1, pp. 381–384, Sep. 1987.

[83] C. K. Lee, “Theory of laminated piezoelectric plates for the design of distributed sensors/actuators. Part I: Governing equations and reciprocal relationships,” J. Acoust. Soc. Am., vol. 87, no. 3, pp. 1144–1158, Mar. 1990.

[84] J. Callahan and H. Baruh, “Modal analysis using segmented piezoelectric sensors,” AIAA J., vol. 33, no. 12, pp. 2371–2378, Dec. 1995.

[85] C. Stefanadis, “Aortic function in arterial hypertension determined by pressure-diameter relation: effects of diltiazem.,” Circulation, vol. 96, no. 6, pp. 1853–8, Sep. 1997.

[86] H. Sorvoja, V. Kokko, R. Myllyla, and J. Miettinen, “Use of EMFi as a blood pressure pulse transducer,” IEEE Trans. Instrum. Meas., vol. 54, no. 6, pp. 2505–2512, 2005.

[87] F. Clemente, P. Arpaia, and P. Cimmino, “A piezo-film-based measurement system for global haemodynamic assessment,” Physiol. Meas., vol. 31, no. 5, pp. 697–714, May 2010.

[88] J. McLaughlin, M. McNeill, B. Braun, and P. D. McCormack, “Piezoelectric sensor determination of arterial pulse wave velocity.,” Physiol. Meas., vol. 24, no. 3, pp. 693–702, Aug. 2003.

[89] G. Schwartz, “Flexible polymer transistors with high pressure sensitivity for application in electronic skin and health monitoring,” Nat. Commun., vol. 4, no.

1, p. 1859, Dec. 2013.

Chapter 3

Mathematical Derivation of Arterial Flow and its Relationship with Haemodynamic Parameters

This chapter aims to develop and describe the mathematical reasoning used for the sensing and measuring of the distention waveform. Then, explanations for the physiological information, interpretations, and related prognostic values are provided. In the first derivation, the pressure-flow relationship is derived from the Navier-Stokes equation, which is central to this study. The second derivation develops the pulse-wave propagation relationship with arterial stiffness. The third derivation develops the arterial stiffness relationship with BP. The fourth derivation develops the relationship between the pulse waveform and haemodynamic parameters, which serves as the basis for the waveform analysis. Lastly, the fusion of the data into a PU-loop relationship is derived.

3.1 The Relationship Between Arterial Flow and Pressure Waveform

The Navier-Stokes equations [1] describe the motion of incompressible Newtonian fluids. These equations have a complex solution, but the equations can be simplified using the continuity equations for the ‘x’, ‘y’, and ‘z’ directions, as given below.

$$\rho\left(\frac{\partial\omega}{\partial t}+\omega\frac{\partial\omega}{\partial x}+v\frac{\partial\omega}{\partial y}+\omega\frac{\partial\omega}{\partial z}\right)=\rho g_x-\frac{\partial y}{\partial x}+\mu\left(\frac{\partial^2\omega}{\partial x^2}+\frac{\partial^2\omega}{\partial y^2}+\frac{\partial^2\omega}{\partial z^2}\right) \quad (3.1)$$

$$\rho\left(\frac{\partial\omega}{\partial t}+\omega\frac{\partial\omega}{\partial x}+v\frac{\partial\omega}{\partial y}+\omega\frac{\partial\omega}{\partial z}\right)=\rho g_y-\frac{\partial y}{\partial y}+\mu\left(\frac{\partial^2\omega}{\partial x^2}+\frac{\partial^2\omega}{\partial y^2}+\frac{\partial^2\omega}{\partial z^2}\right) \quad (3.2)$$

$$\rho\left(\frac{\partial\omega}{\partial t}+\omega\frac{\partial\omega}{\partial x}+v\frac{\partial\omega}{\partial y}+\omega\frac{\partial\omega}{\partial z}\right)=\rho g_z-\frac{\partial y}{\partial z}+\mu\left(\frac{\partial^2\omega}{\partial x^2}+\frac{\partial^2\omega}{\partial y^2}+\frac{\partial^2\omega}{\partial z^2}\right) \quad (3.3)$$

where $\frac{\partial\omega}{\partial x}$ is the pressure force in the x direction, ρg_x is the weight of the fluid in the x direction, and the corresponding variables refer to the same information in the ‘y’ and ‘z’ directions. The second partial derivative represents the viscous forces, in their respective directional axes.

$$\rho\left(\frac{\partial\omega}{\partial t}+\omega\frac{\partial\omega}{\partial x}+v_r\frac{\partial\omega}{\partial r}+\frac{v_\theta}{r}\frac{\partial\omega}{\partial\theta}\right)=\rho g_x-\frac{\partial p}{\partial x}+\mu\left(\frac{\partial^2\omega}{\partial x^2}+\frac{\partial^2\omega}{\partial r^2}+\frac{1}{r}\frac{\partial\omega}{\partial r}+\frac{1}{x^2}\frac{\partial^2\omega}{\partial z^2}\right) \quad (3.4)$$

Simplifying the equations using Poiseuille flow [2], which describes the velocity of the fluid, results in the following:

$$\omega=\frac{1}{4\mu}\frac{dP}{dx}[r^2-R^2] \quad (3.5)$$

Where $'\rho'$ is the liquid density, $'\mu'$ is viscosity, $'v'$ is kinematic viscosity (ratio between density and viscosity), $'P'$ is pressure, $'R'$ is the external radius of the tube, $'r'$ is the internal radius of the tube, $'l'$ is the length of the tube, $'\omega'$ is the longitudinal velocity of the liquid, and '$f=\frac{n}{2\pi}$' is the frequency, equal to the HR of the subject.

The Poiseuille flow is steady and uniform over a laminar cross-section, and axially is symmetric with a cylindrical tube, which makes $\frac{\partial\omega}{\partial t}=0$, $\frac{\partial\omega}{\partial x}=0$, and $\frac{\partial\omega}{\partial\theta}=0$.

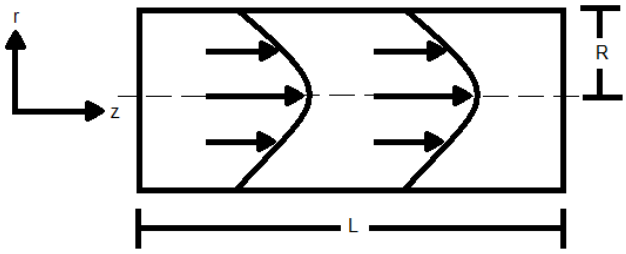

Figure 3.1: Laminar flow in a tube

$$Pressure\ gradient=\frac{p_1-p_2}{l} \quad (3.6)$$

The simplified Navier-Stokes equation, based on Poiseuille flow, is represented as:

$$\frac{d^2\omega}{dr^2}+\frac{1}{r}\frac{d\omega}{dr}+\frac{p_1-p_2}{l}=0 \quad (3.7)$$

Womersley et al. [3] expressed the arterial pulse pressure gradient as a periodic function, equivalent to the HR, as described below:

$$f=\frac{n}{2\pi} \quad (3.8)$$

The Fourier series representation of the pressure partial derivative is

$$\frac{\partial P}{\partial x} = R_e\left[\sum_{n=0}^{\infty} a_n e^{ifnt}\right] \tag{3.9}$$

where

$$a_n = A_n + iB_n$$

Using Euler's formula, the Fourier coefficients can be represented as follows:

$$\frac{\partial P}{\partial x} = A_0 + \sum_{n=1}^{N} A_n \cos(fnt) + \sum_{n=1}^{N} B_n \sin(fnt) \tag{3.10}$$

To calculate the coefficients, this equation can be written as:

$$A_n = \frac{2}{T_0}\int_0^{T_0} \frac{dy}{dx}\cos(fnt)\, dt \tag{3.11}$$

$$B_n = \frac{2}{T_0}\int_0^{T_0} \frac{dP}{dx}\sin(fnt)\, dt \tag{3.12}$$

Solving for flow velocity, as it is assumed to follow Poiseuille flow rules, which change over time, $\frac{\partial \omega}{\partial x} = 0$ and $\frac{\partial \omega}{\partial \theta} = 0$. When solving for a single harmonic, n:

$$\frac{d^2\omega}{dr^2} + \frac{1}{r}\frac{d\omega}{dr} + \frac{1}{v}\frac{d\omega}{dt} = -\frac{a_n e^{ifnt}}{\mu} \tag{3.13}$$

Velocity changes periodically, over the period defined as:

$$\omega = u(r)e^{ifnt} \tag{3.14}$$

Substituting equation 3.14 into equation 3.13 and dividing by e^{ifnt} results in the following equation:

$$\frac{d^2u}{dr^2} + \frac{1}{r}\frac{du}{dr} + \frac{ifn}{v}u = -\frac{a_n}{\mu} \tag{3.15}$$

Equation 3.15 can be transformed into a Bessel zero-order differential equation, using the fact that:

$$-i = i^3 \tag{3.16}$$

Therefore, equation 3.15 becomes:

$$\frac{d^2u}{dr^2} + \frac{1}{r}\frac{du}{dr} + \frac{i^3 fn}{v}u = -\frac{a_n}{\mu} \tag{3.17}$$

The Bessel differential equation general form is:

$$\frac{d^2u}{dr^2} + \frac{1}{r}\frac{du}{dr} + \lambda^2 u = 0 \tag{3.18}$$

where

$$\lambda = \frac{i^3 fn}{v} \tag{3.19}$$

The solution for the general Bessel function is as follows:

$$u_n(r) = c_1 J_0\left(ri^{\frac{3}{2}}\sqrt{\frac{fn}{v}}\right) + c_2 Y_0\left(ri^{\frac{3}{2}}\sqrt{\frac{fn}{v}}\right) \tag{3.20}$$

The term $'Y_0'$ must be discarded, as $'u_n(r)'$ is finite in the centre of the tube. Because equation 3.17 is not in homogenous, a simple solution can be stated, as follows:

$$u_n(r) = c_3 \tag{3.21}$$

The terms involving $'u'$ are zero, resulting in the following equation:

$$\frac{i^3 fn}{v} u = -\frac{a_n}{\mu} \tag{3.22}$$

Because kinematic viscosity is measured as follows:

$$v = \frac{\mu}{\rho} \tag{3.23}$$

Equation 3.22 becomes:

$$c_3 = \frac{a_n}{i\rho fn} \tag{3.24}$$

The solution is:

$$u_n(r) = c_1 J_0\left(ri^{\frac{3}{2}}\sqrt{\frac{fn}{v}}\right) + \frac{a_n}{i\rho fn} \tag{3.25}$$

By solving the above equation with, the no-slip condition that $'u = 0'$ and $'r = R'$:

$$c_{1=} \frac{a_n}{i\rho fn J_0\left(Ri^{\frac{3}{2}}\sqrt{\frac{fn}{v}}\right)} \tag{3.26}$$

Finally:

$$u_n(r) = \frac{a_n}{i\rho fn}\left[\frac{J_0(\lambda r)}{J_0(\lambda R)} - 1\right] \tag{3.27}$$

Adding the steady flow velocity $'u_0'$ results in the following:

$$u(r) = u_0 \sum_{n=1}^{\infty} u_n(r) \tag{3.28}$$

By integrating velocity over a differential area, through the cross-sectional area of the tube, the flow rate becomes:

$$Q = 2\pi \int_0^R u(r) r dr \tag{3.29}$$

For a steady flow:

$$u = \frac{p_1 - p_2}{ul}(r^2 - R^2) \tag{3.30}$$

Integration results in the following:

$$Q = \frac{p_1 - p_2}{8ul}\pi R^4 \tag{3.31}$$

which is Poiseuille's formula, replacing $'u(r)'$ and using the fact that:

$$\int x J_0(x)\, dx = x J_1(x)$$

$$Q_n = \frac{\pi R^4}{\mu} R_e \left[\frac{a_n}{ifn}\left\{1 - \frac{2\alpha i^{3/2}}{i^3\alpha^2}\frac{J_1\left(\alpha i^{3/2}\right)}{J_0\left(\alpha i^{3/2}\right)}\right\} e^{ifnt}\right] \tag{3.32}$$

The average flow rate is calculated as:

$$Q_0 = a_0 \frac{8\mu}{\pi R^4} \tag{3.33}$$

The solution, in terms of the Fourier series, becomes:

$$Q = Q_0 + \sum_{n=1}^{\infty} Q_n \tag{3.34}$$

Womersley solved the equation using the Bessel function in the 19th century, but computation is not the focus of this article, in which it is used as follows:

$$J_0\left(x i^{3/2}\right) = M_0(x) e^{i\theta_0} \tag{3.35}$$

$$J_1\left(\alpha i^{3/2}\right) = M_1 e^{i\theta_1} \tag{3.36}$$

Using the real part of $'e^{ifnt}'$ is $'M_n \cos(fnt + \phi)'$, where $'M_n = \sqrt{A^2 + B^2} = |a_n|'$. Simplifying for '*Q*' gives the following equation:

$$Q = \frac{\pi M R^4}{\mu}\frac{M'_{10}}{\alpha^2}\sin(fmt + \phi + \epsilon_{10}) \tag{3.37}$$

The graph in Figure 3.2 depicts the pressure gradient *'P',* juxtaposed with the flow rate *'Q'*, showing the phase-lag between the two curves [4].

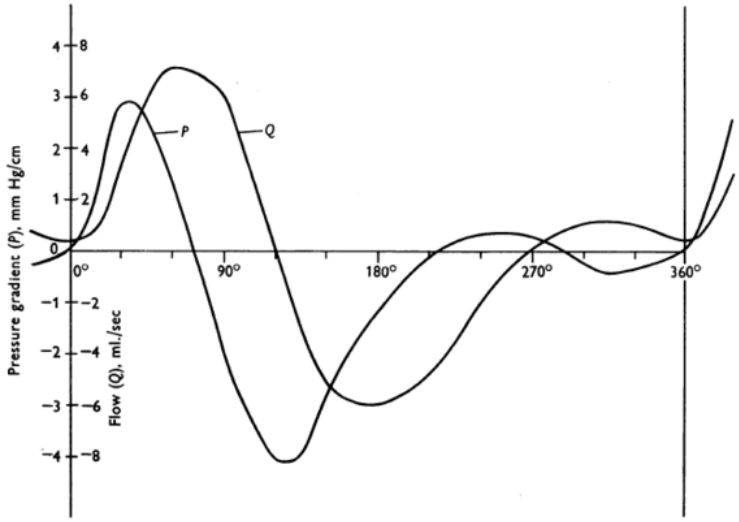

Figure 3.2: Flow rate 'Q' lags the pressure gradient 'P' [3][4]

3.2 Pulse Wave Propagation

Assuming an indefinitely long, isolated tube, through which an inviscid (non-viscous) liquid flows, the wave amplitude is small and has a long wavelength compared with the tube radius, where the slope of the wall deformation is less than one (< 1).

For simplicity, a one-dimensional flow can be used. Consider a small fluid element, in which an increase in pressure produces an increase in area, as shown below:

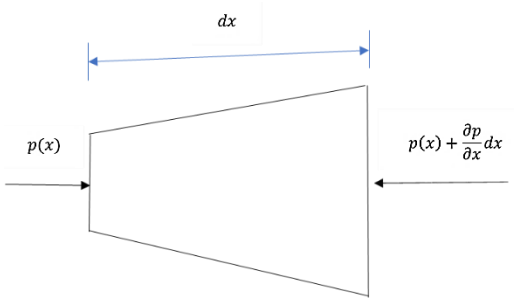

Figure 3.3: Change in pressure produces a change in the area of the liquid

By using the mass and momentum conservation equations, we have:

$$\frac{\partial u}{\partial t} + u\frac{\partial u}{\partial x} + \frac{1}{\rho}\frac{\partial p}{\partial x} = 0 \tag{3.38}$$

$$\frac{\partial A}{\partial t} + \frac{\partial (uA)}{\partial x} = 0 \tag{3.39}$$

Linearising the equation by assuming velocity, derivatives of the pressure difference and area change are small, resulting in the following:

$$\frac{\partial A}{\partial t} + A_0 \frac{\partial (u)}{\partial x} = 0 \tag{3.40}$$

$$\frac{\partial u}{\partial t} + \frac{1}{\rho}\frac{\partial p}{\partial x} = 0 \tag{3.41}$$

Taking the derivative of the equation, and equating for $'\frac{\partial u}{\partial t \partial x}'$ results in the following:

$$\frac{\partial^2 A}{\partial t^2} = \frac{A_0}{\rho}\frac{\partial^2 p}{\partial x^2} \tag{3.42}$$

Because the pressure in a thin wall tube is based on solid mechanics, the following equation applies:

$$p(x) = \frac{Eh}{a_0}\left[1 - \left(\frac{A_0}{A}\right)^{1/2}\right] \tag{3.43}$$

The binomial expansion of $\left[1 - \left(\frac{A_0}{A}\right)^{1/2}\right]$ returns:

$$p = \frac{Eh(A - A_0)}{2a_0 A_0} \tag{3.44}$$

By taking the second derivative, the following is obtained:

$$\frac{\partial^2 p}{\partial t^2} = \frac{Eh}{2a_0 A_0}\frac{\partial^2 A}{\partial t^2} \tag{3.45}$$

By using Equations 3.42 and 3.45:

$$\frac{\partial^2 p}{\partial t^2} = \frac{Eh}{2\rho a_0}\frac{\partial^2 p}{\partial x^2} \tag{3.46}$$

Which represents a standard wave equation, with the wave speed:

$$\frac{\partial^2 p}{\partial t^2} = c^2 \frac{\partial^2 p}{\partial x^2} \tag{3.47}$$

Which implies *'c'* as:

$$c = \sqrt{\frac{Eh}{2\rho a_0}} \tag{3.48}$$

This equation is the Moen-Korteweg equation [4], which states the relationship between PWV and arterial distensibility. Where '*E'* is Young's modulus of the arterial wall, *'h'* is the wall thickness, $'a_0'$ is the arterial diameter and *'ρ'* is the blood density.

3.3 PTT Relationship with BP

PTT represents the time delay of an arterial pulse between two spatially separated Eulerian frames of references on an artery. The PTT relationship with PWV can be mathematically expressed by the equation below:

$$PWV = \frac{\Delta X}{PTT} \tag{3.49}$$

where $'\Delta X'$ is the distance between two Eulerian points of references. The Moens-Korteweg equation relates elasticity to PWV, as described in the equation below:

$$PWV = \sqrt{\frac{Eh}{2r\rho}} \tag{3.50}$$

where *'E'* is the arterial Young's modulus (kg/ms^2), *'h'* is the thickness of the artery (*m*), *'r'* is the artery inner radius (*m*), and *'ρ'* is the blood density (kg/m^3). Young's modulus [5] of a material can be described as follows:

$$E = E_0 e^{\alpha P} \tag{3.51}$$

where $'E_0'$ is Young's modulus at zero pressure (Kg), *'P'* is arterial pressure (mmHg), and $'\alpha'$ is a fitting coefficient (1/mmHg). By solving equations 3.49, 3.50, and 3.51, arterial transmural pressure can be expressed as:

$$P = \frac{1}{\alpha}\ln\left(\frac{2r\rho\Delta X^2}{E_0 h}\right) - \frac{2}{\alpha}\ln(PTT) \tag{3.52}$$

The mean arterial pressure or transmural pressure is directly proportional to *'PTT',* which translate to the basis of cuffless BP measurement methods.

3.4 Arterial Waveform Relationship with a Haemodynamic Parameter

The heart pumps blood in a non-continuous manner through the aorta, which works under the WK principle [6], analogous to the resistor-capacitor parallel circuit [7], is shown in Figure 3.4 which takes account for compliance (cm^3/mmHg) and total peripheral resistance (mmHg x s/cm^3) of an artery . The compliance of an artery allows

volumetric expansion of the artery due to sudden release of blood and compliance varies in the arterial tree. The geometry of artery results in total peripheral resistance, smaller the artery higher the resistance. The valve resistance 'r' is taken as constant due to the rapid opening and closing operation. The propagation of pulse wave depends on the elasticity of the arteries; stiffer arteries result in higher PWV. This relationship is described in the Moens-Korteweg equation (Equation 3.47).

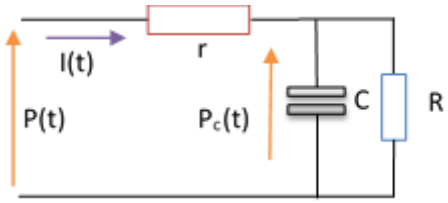

Figure 3.4: 3-element Windkessel model

The Kirchhoff current and voltage law equations for the model are as follows:

$$P(t) = I(t) * r + P_c(t) \tag{3.53}$$

$$I(t) = \frac{P_c(t)}{R} - C\frac{dP_c(t)}{dt} \tag{3.54}$$

where the arterial flow parameters analogous to electrical model parameters are as follows: '*P(t)*' is aortic BP in mmHg, '*I(t)*' is blood flow from the heart in cm^3/s, '*r*' is an aortic blood flow resistance, in $mmHg{\cdot}s/cm^3$, '$P_c(t)$' is aortic compliance in $cm^3/mmHg$, *'C'* is arterial compliance in $cm^3/mmHg$, and '*R*' is the systematic arterial system peripheral resistance in $mmHg{\cdot}s/cm^3$.

By using a state-space canonical representation and the Laplace transform, the transfer function of the 3-element WK model can be described, as shown in Figure 3.4:

$$H(s) = \frac{R}{RCs+1} + r \tag{3.55}$$

The Joukovsky equation states that changes in flow are directly proportional to changes in pressure across a wavefront [8]. The relationship between pulse pressure and PWV is described as follows:

$$PP = \rho v_0 PWV \tag{3.56}$$

where *'PP'* is pulse pressure and $'v_0'$ is the blood velocity of the heart cycle, which is described as follows:

$$v_0 = 2\frac{Q}{S} = \frac{8 \times SV \times HR}{\pi\, d^2} \tag{3.57}$$

where *'HR'* is HR, *'SV'* is stroke volume, and '*d'* is the diameter of the artery. By replacing the values in equation 3.56, using equation 3.57:

$$PP = \frac{8 \times SV \times HR}{\pi\, d^2} \sqrt{\frac{Eh}{\rho d}} \tag{3.58}$$

The pulse pressure waveform is dependent on elasticity, diameter, HR, and stroke volume. Pulse pressure is the pulse height of an arterial waveform, which is the value metric difference between the systolic and diastolic peaks, which inherit hemodynamic characteristics [9]. Waveform analysis can demonstrate the outcomes of hemodynamic parameters and arterial stiffness indices.

3.5 Pressure-Volume Loop – Data Fusion

Forces on fluids can be calculated by Newton's second law [10] of motion, which states that the acceleration *'a'* of an object is directly proportional to the magnitude of force *'F'* in the same direction and is inversely proportional to the mass 'm*'* of an object, which can be shown as:

$$F = ma \tag{3.59}$$

In our case, if pressure terms are used, then force can be presented as a change in pressure on the area. The change in momentum can represent the mass flow rate. Therefore, the equation is as follows:

$$dp\ A = C\rho\ A\ (u_i - u_0) \tag{3.60}$$

Simplifying the equation produces the Joukowsky equation [11]:

$$\Delta p = C\ \rho\ \Delta v \tag{3.61}$$

Velocity accounts for arterial stiffness, which can be measured by modifying Hooke's law as follows:

$$C = \sqrt{\frac{1}{\rho[\frac{1}{K} + \frac{D}{Ee}]}} \tag{3.62}$$

where *'ρ'* = blood density, *'K'* = bulk modulus of fluid, *'E'* = Young's modulus, *'e'* = wall thickness of the pipe, and *'D'* = artery diameter.

3.6 Summary

This chapter derives the mathematical relationships between the arterial waveform and the haemodynamic parameters, to explain the core principles that underly this research study. First, the Navier-Stokes equation was used to derive the relationship between blood flow and the pressure waveform, highlighting the differences between the sensing methodologies used for PPG and BPP waveforms. The classical derivation of the Womersley equation showed the phased lag between the flow rate and pressure gradient, which is a pivotal focus of using the BPP sensor in this research study. Second, the mathematical derivation of PWV, which states the Moen-Korteweg equation, was performed to describe the relationship between PWV and arterial stiffness parameters. Third, a derivation between PTT and BP was shown, which is the sole driving force for cuffless BP measurements, stating the direct relationship between these parameters. Fourth, a derivation between the morphology of the arterial waveform and the haemodynamic parameters was shown, to define the relationship between the arterial stiffness indexes and their effects on the cardiovascular system. Lastly, the Joukowsky equation was used to explain the use of the PU-loop to verify the PPG and BPP sensors. This chapter provided the mathematical reasoning for the study, the relationship between the haemodynamic parameters and cuffless BP measurement techniques, the direct effects of stiffness on BP waveforms, the importance of morphological indexes, and a synthesis of all of this information was verified.

3.7 References

[1] V. Girault and P. A. Raviart, "Finite Element Approximation of the Navier-Stokes Equations," Lecture Notes in Mathematics, vol. 749. Berlin-Heidelberg-New York: Springer 1979.

[2] S. Wilson, "The development of Poiseuille flow" Journal of Fluid Mechanics, vol. 38(4), pp 793-806, 1969.

[3] J. R. Womersley, “Method for the calculation of velocity, rate of flow and viscous drag in arteries when the pressure gradient is known.,” J. Physiol., vol. 127, no. 3, pp. 553–63, Mar. 1955.

[4]J. F. Hale, D. A. McDonald, and J. R. Womersley, “Velocity profiles of oscillating arterial flow, with some calculations of viscous drag and the Reynolds numbers.,” J. Physiol., vol. 128, no. 3, pp. 629–40, Jun. 1955.

[5] A. Farsi, A. D. Pullen, J. P. Latham, J. Bowen, M. Carlsson, E. H. Stitt, and M. Marigo, "Full deflection profile calculation and Young's modulus optimisation for engineered high performance materials," Scientific reports, 7, pp 46190, 2017.

[6] K. Her, J. K. Kim, K. M. Lim, and S. W. Choi, "Windkessel model of hemodynamic state supported by a pulsatile ventricular assist device in premature ventricle contraction," Biomedical engineering online, vol. 17(1), pp 18, 2018.

[7] A. Noordergraaf, Circulatory system dynamics. Academic Press, 1978.

[8] M. S. Ghidaoui, “On the fundamental equations of water hammer,” Urban Water J., vol. 1, no. 2, pp. 71–83, Jun. 2004.

[9] S. C. Millasseau et al., “Noninvasive assessment of the digital volume pulse. Comparison with the peripheral pressure pulse.,” Hypertens. (Dallas, Tex. 1979), vol. 36, no. 6, pp. 952–6, Dec. 2000.

[10] G. Buchdahl, "Science and logic: some thoughts on newton's second law of motion in classical mechanics," The British journal for the philosophy of science, volume 2(7), pp 217-235, 1951.

[11] P.R. Hanmaiahgari, R. R. Kottam and M. Kaushik, "Estimation and examination of linepack pressures in long liquid pipelines," Sādhanā, vol. 44, pp 101 - 105, 2019.

Chapter 4

Experimental Setup, Signal Processing, and Statistical Analysis

This chapter describes the experimental setup and methodologies that were used to achieve the specific aims and objectives of the study and to prove a hypothesis regarding the potential use of a ballistic pulse pressure (BPP)sensor. The hypothesis consists of three components: 1) the Polyvinylidene fluoride (PVDF) sensor can measure arterial distention waveforms, BPP waveform, which can electromechanically track the beat-to-beat changes associated with HRV; 2) the BPP sensor methodology collects richer, less-skewed raw data than a Photoplethysmogram (PPG) sensor; and 3) the combination between a BPP and a PPG sensor can form a pressure volume loop (PU-loop). This chapter first explains the acquisition platform and the integration of commercial, off-the-shelf components, and then explains the data collection environment, the study protocol, and the signal processing utilisation, in addition to the validation of the platform against various existing gold standards.

4.1 Materials and Methods

4.1.1 Acquisition Units

The Biopac MP36R unit (Biopac System, USA) was used for the simultaneous acquisition of signals. The acquisition device is comprised of four synchronised acquisition channels, which digitise data, at a sample rate of 1 kHz, with a resolution of 24 bits, in real-time. The acquisition device is serially connected to a PC (Windows 10 OS), through AcqKnowledge 4 software, which facilitates data visualisation, analysis, and export.

4.1.1.1 The Electrocardiogram Sensor

The electrocardiogram (ECG) signal was captured, and its R-peak provided a reference location for the cardiac cycles for all arterial waveform. Three electrodes were placed proximally (i.e. on the left shoulder, right shoulder, and at the pelvis) to capture an Einthoven lead-I, to view lateral wall of left ventricle, signal configuration,

as shown in Figure 4.1. The chest area provides a stable anchoring position for the ECG signal, which limits noise and motion artefacts. Before placing the hydrogel electrodes, the skin of a subject was cleaned with an alcoholic swipe, and hair was removed, to ensure good surface contact. Biopac SS2LB leads were used to capture the data on channel 1 of the Biopac MP36R unit.

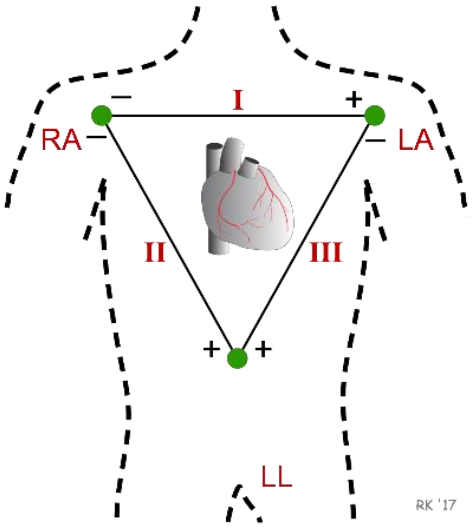

Figure 4.1: Einthoven's triangle, for ECG electrode placement on the human chest

4.1.1.2 The PPG Sensor

A 960-nm wavelength photodiode was used to illuminate the finger area, and blood flow changes were captured by a photodetector, which corresponded to the optical absorption of the volumetric blood flow. A wavelength of 960 nm achieves the highest depth into the hypodermis layer [1], which, in turn, can obtain a response from the radial indics artery, at the distal phalanx in the index digit. The reflectance sensing technique provided sufficient backscattering for the experiment. The skin of the subject was cleaned with a non-alcoholic swipe before the sensors were placed on the finger. Biopac SS4LA leads were used to capture data on channels 2 and 4 of the Biopac MP36R unit.

4.1.1.3 The BPP Sensor

PVDF piezoelectric sensors were used and placed on the index finger, to measure the distension waveform of the radial indics artery. The measured waveform is generated by the pulsating blood flow and referred to as ballistic pulse pressure (BPP). PVDF piezoelectric sensors (Measurement Specialist Ltd., USA) were used, and their

outputs were interfaced with an amplifier (Piezo Film Lab amplifier by Measurement Specialist). The surface of the sensor was insulated with electrostatic tape. The settings of the sensor amplifier are shown in Table 4.1. The output of the amplifier was interfaced with an SS9LA lead, through a BNC cable, to channels 1 and 3 of the Biopac MP36R unit. The sensor was wrapped on top of the PPG sensor fixture and strapped around the distal phalanx of the index finger. The stacking of the BPP sensor over the PPG sensor resulted in a vertical spatial alignment for the single-point, simultaneous acquisition of the waveforms.

Table 4.1**:** The parameters of the Piezo Film Lab amplifier used to measure the BPP waveform

Mode	Voltage—1G (50 pF)
Low frequency of the filter	0.1 Hz
High frequency of the filter	10 Hz
Gain	10 dB typical
Power source	9V Battery

4.1.1.4 The Tonometric Sensor

The SphygmoCor (AtCor Medical, Australia) tonometry system's, tonometric waveform (SPH) limited version, with an analogue output tonometer, was used to capture applanation tonometric data at the radial artery. The output of the system was acquired using the SS9LA interface, as an analogue signal, at channel 3 of the Biopac MP36R unit.

4.1.1.5 Miscellaneous Sensors

Huntleigh Smartsigns LitePlus Vital Signs Monitor was used to measure the brachial BP of subjects, using a medium-sized arm cuff, in a seated posture. The Nokia Body Cardio scale was used to measure the subject's weight, in kg. The subject's height was measured with a wall-mount height measurement scale. The subject's mood

(stressed/relaxed), meals, and coffee intake were recorded before and after measurements in a questionnaire.

4.1.2 Data Collection Environment

All sensors were placed on the subject's left hand, in a seated posture, with the arm on the desk. The temperature was controlled, at 22°C, and the measurements were performed in a comfortable environment, as shown in Figure 4.2.

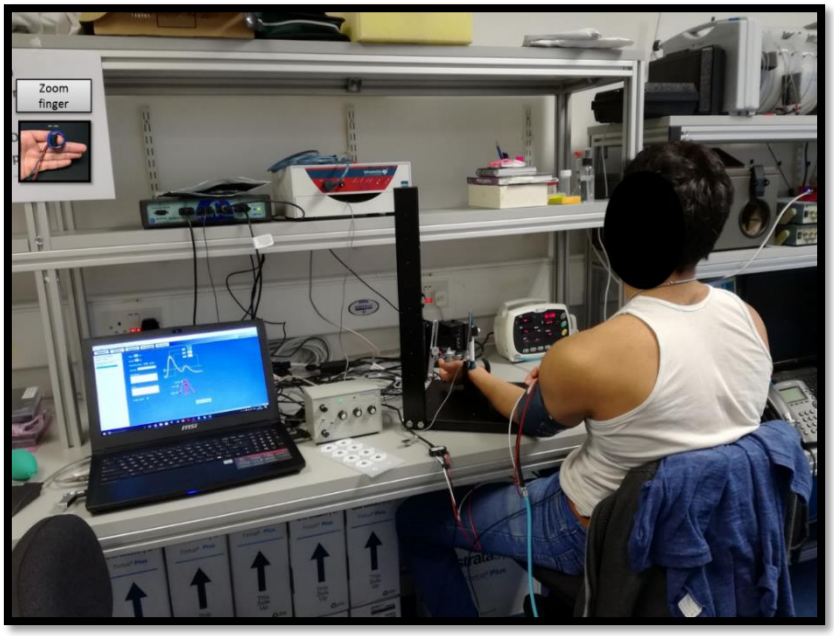

Figure 4.2: Signal acquisition setup environment, showing the actual acquisition of subject 7

4.1.3 Study Protocol

This study was conducted on a total of 22 healthy volunteers, aged 32 ± 6 years, with a mix of ethnic backgrounds. For this study, the experiments were performed in accordance with the Helsinki declaration protocol, and ethical approval was obtained, as 'A feasibility study to evaluate a novel method of assessing microcirculatory function as a predictor of the risk of Major Adverse Cardiac Events' (IRAS Project ID 166742 approved on April 30, 2020). Subjects were asked to refrain from consuming alcohol for 36 hours, meals for 4 hours, and coffee for 2 hours prior to data collection.

Subjects were asked to remain calm and avoid making any unnecessary movements, to reduce motion artefacts and avoid/minimize respiration modulation. No hydrostatic

or gravitational variations in the artery under observation occurred, as the subject's arm was maintained on a table, at a fixed location. The data collection protocol is illustrated in Figure 4.3. Subject's data were excluded if the interbeat interval (IBI) did not follow similar behaviours across technologies.

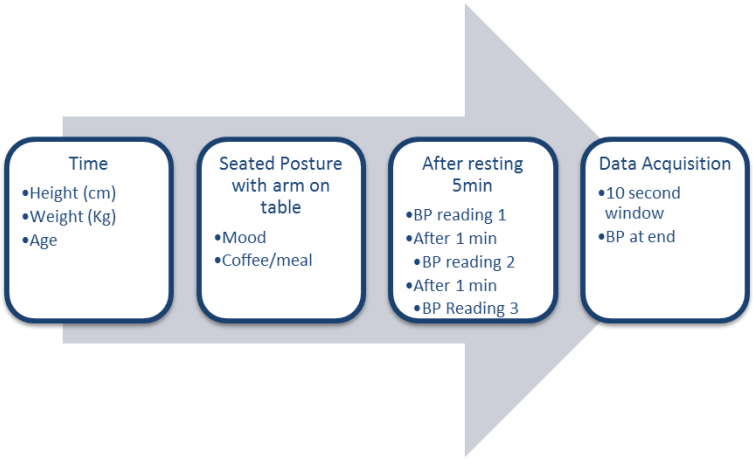

Figure 4.3**:** The data collection protocol

4.2 Experimental Setup for Heart Rate Variability Comparison Study

4.2.1 Aim and Objective

The primary aim of the experiment was to test the responsiveness and trackability of the BPP waveform against PPG waveform and ECG R-peak by using HRV analysis. The objective of the experiment was as follows:

1- To capture a noise- and artefact-free BPP waveform.
2- To co-locate the BPP and PPG sensors on the index finger distal phalanx.
3- To validate the BPP and PPG waveforms against the ECG waveform, for the HRV analysis of the cohort.
4- To investigate the most suitable fiducial point of the BPP waveform that can be used as a surrogate for the ECG R-peak

4.2.2 System Block Diagram

The system block diagram is shown in Figure 4.4. ECG, PPG, and BPP sensors were used to capture data, simultaneously, using a Biopac MP36R.

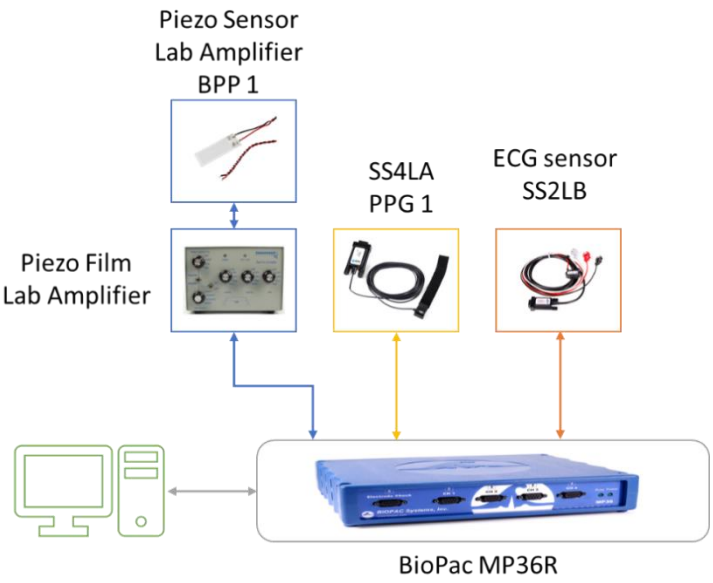

Figure 4.4: Block diagram of the data acquisition design, using a Biopac MP36R. The BPP sensor is shown on the top left, the PPG sensor is in the middle, and the ECG sensor is on the right.

4.2.3 Sensor Placement

The PPG sensor was placed at the distal phalanx of the index finger, and the BPP sensor was strapped on top of the PPG sensor, to spatially align the sensors. A schematic image showing the configuration of the co-located PPG and BPP sensors configuration is shown in Figure 4.5, and the sensor placement on the subject's finger is shown in Figure 4.6.

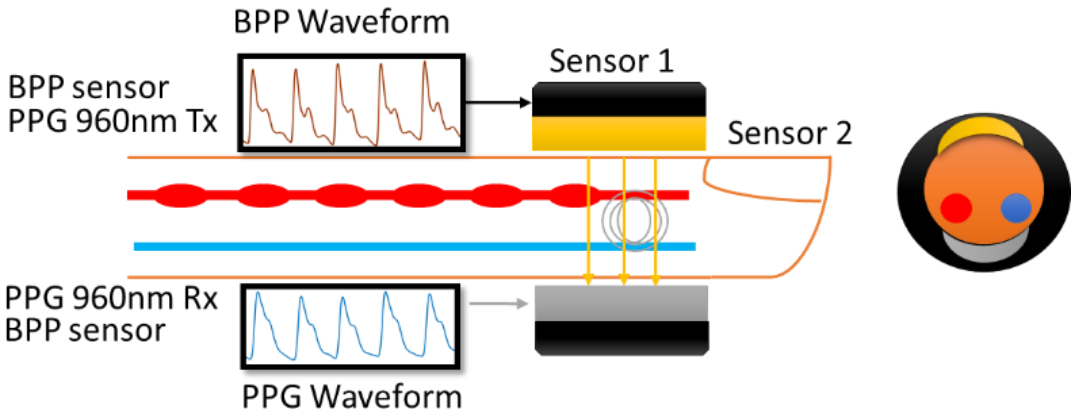

Figure 4.5: Schematic diagram illustrating the mounting of the PPG and BPP sensors on a subject's finger and demonstrating their waveforms

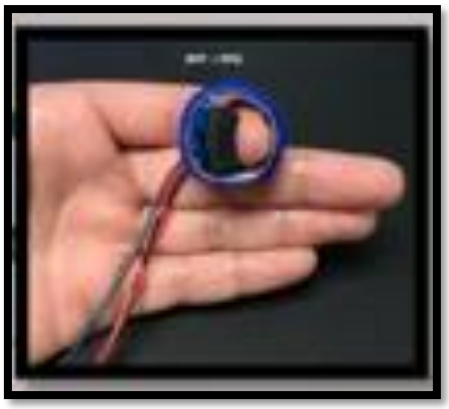

Figure 4.6: PVDF and PPG sensors placed on the subject's finger

4.2.4 Validation Sensor

In this experiment, the standard ECG electrode wereplaced on the subject's chest, was used as the gold standard for the measurement of HRV.

4.2.5 Fiducial Location of the Waveforms

Three critical locations in the BPP and PPG waveforms were selected for the analysis, which were compared against the ECG waveform. These fiducial points were as follows:

1. The peaks of the BPP and PPG waveforms.
2. The peaks of the first derivatives of the PPG and BPP waveforms.
3. The peaks of the second derivatives of the PPG and BPP waveforms.

These fiducial points are the least affected by wave reflection caused by bifurcation and peripheral resistance during blood flow in the arterial tree [2]. The fiducial points are marked on each waveform and are shown in Figures 4.7, 4.8, and 4.9.

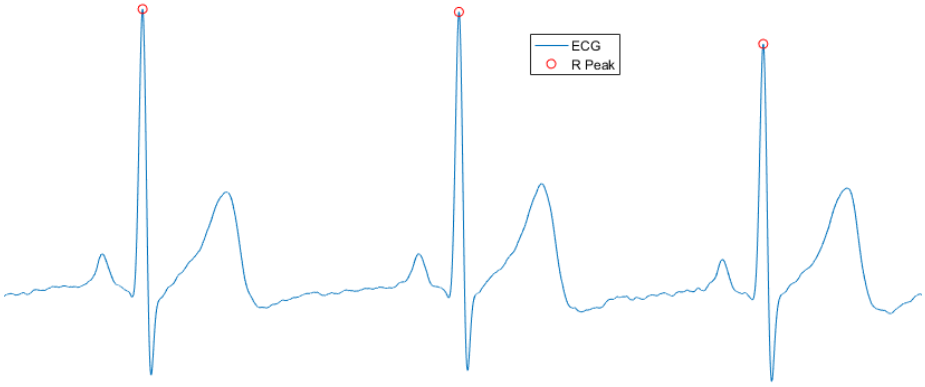

Figure 4.7: ECG waveforms from subject 7

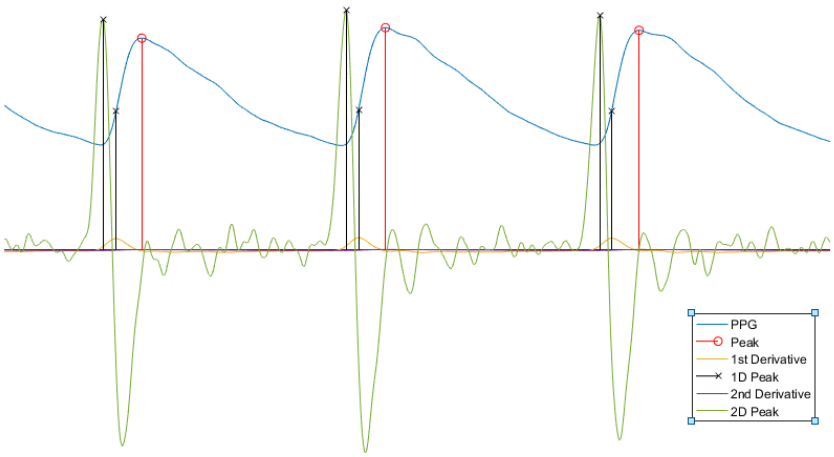

Figure 4.8: PPG waveform fiducial locations and the first and second derivative locations, for subject 7

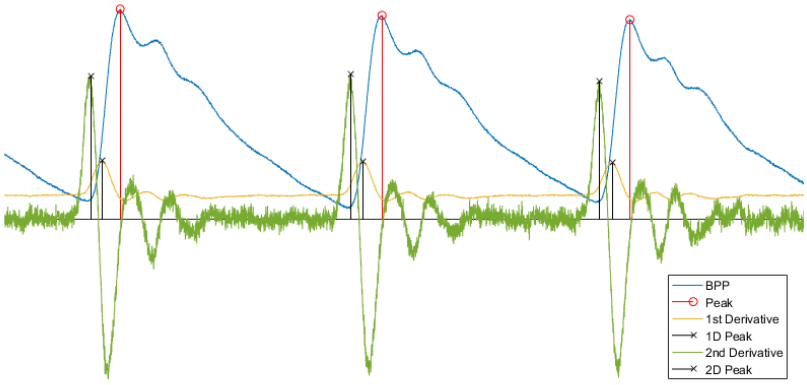

Figure 4.9: BPP waveform fiducial locations and the first and second derivatives for subject 7

4.2.6 Signal Processing Algorithm

The data were filtered using Savitzky-Golay filter, to remove noise from the signals, and the fiducial points were marked by taking the peaks of the waveform, the peaks of the first derivative, and the peaks of the second derivative, for the BPP and PPG waveforms. The R-peak on the ECG signal was detected using the Pans-Tompkins algorithm [3], and the data were visually inspected for cardiac arrhythmia. All fiducial points were detected, and the beat-to-beat intervals were calculated to perform the HRV analysis, using an open-source code [4] that is available online. Finally, statistical analyses were performed.

4.2.7 Comparison Method – Statistical Analysis

The ECG R-peak was compared against the following parameters, individually, for HRV analysis:

1. PPG peak
2. PPG peak of the first derivative
3. PPG peak of the second derivative
4. BPP peak
5. BPP peak of the first derivative
6. BPP peak of the second derivative

The agreement analysis was performed via Bland-Altman analysis. A regression analysis was performed to identify correlations among the parameters, and Spearman's rank correlation analysis was used to validate the lack of bias in the regression analysis.

4.3 Experimental Setup for the Arterial Indexes Comparison Study

4.3.1 Aim and Objective

This experiment aimed to compare the BPP waveform against the PPG waveform and to validate both against the tonometric waveform (SPH), using the SphymoCor system. The objectives of the experiment were as follows:

1- To capture the BPP, PPG, and SPH waveforms.
2- To compare the arterial indexes in the arterial waveforms.

3- To investigate the WK model transfer function for the BPP waveform, compared with the SphygmoCor tonometer.

4.3.2 System Block Diagram

The system block diagram is shown in Figure 4.10. ECG, PPG, BPP, and SPH sensors were used, attached to an MP36R unit for the simultaneous acquisition of arterial waveforms. The BP measurement was recorded manually, using a Microsoft Excel file.

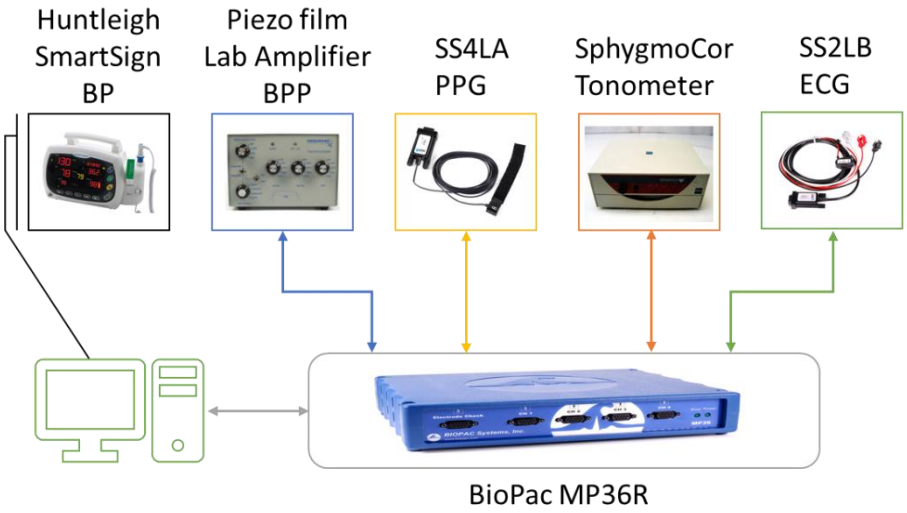

Figure 4.10: Block diagram illustrating the acquisition unit, using the Biopac MP36R unit shown on the bottom, with the sensors shown on the top.

4.3.3 Sensor Placement

The PPG sensor was placed at the distal phalanx of the index finger, and the BPP sensor was wrapped on top of the PPG sensor fixture and strapped around the distal phalanx of the index finger. The stacking of the BPP sensor over the PPG sensor provided the spatial and temporal alignment necessary for the single-point simultaneous acquisition of arterial waveforms. The tonometric sensor was placed at the radial artery, for applanation across the radius bone. A micromanipulator was used (Unisense 4958 Denmark) for the unaided human operation during the data acquisition, to achieve a consistent minimum acceptable operator index (reproducibility of waveform) of 85%. The micromanipulator provided the best repeatability and accuracy for signal acquisition during the experiment, as shown in Figure 4.11. To prop up the radius, at the wrist, a custom, 3D-printed (using a Fortus

380mc 3D Printer), semi-circular wrist clamp was used, as shown in Figure 4.12. The radial artery was palpated and marked, to align the tip of the tonometer accurately. For each subject, the tonometer vertical pressure was adjusted manually, by observing the saturation/clipping effect in the waveform, using the SphygmoCor system suite.

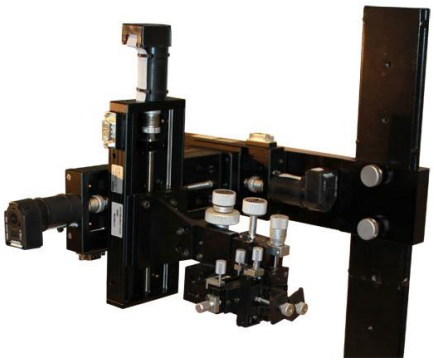

Figure 4.11: Unisense Micromanipulator 4958

Figure 4.12: 3D fixture for holding the subject's wrist

4.3.4 Validation Sensor

The SphygmoCor tonometer was used as the gold standard for the cross-validation of the PPG and BPP waveforms.

4.3.5 Fiducial Points

The waveforms are shown in Figure 4.13, and the fiducial points [5] of the waveforms are marked in Figure 4.14: *'S'* represents the diastolic peak of blood flow in the artery, indicating the aortic valve opening point and the lowest pressure for blood flow; *'P'* represents the systolic peak of blood flow in the artery, indicating the highest pressure point for blood flow; *'T'* represents the tidal wave of blood flow in the artery, indicating the reflected wave in smaller arteries; *'C'* represents the incisura wave of blood flow in

the artery, indicating aortic valve closure; *'D'* represents the dicrotic wave of blood flow in the artery which indicates the reflected pressure wave effect on waveform.

The fiducial points [6] of the second derivative, shown in Figure 4.15, and the APG arterial waveform are as follows: the '*a-wave'* is the pre-systolic positive peak of the APG; the '*b-wave'* is the pre-systolic negative peak of the APG; the '*c-wave'* is the post-systolic crest of the APG; the '*d-wave'* is the post-systolic trough; and the 'e-wave' aligns with the incisura wave.

The augmentation index (AIx), ageing index (AI), stiffness index (SI), reflection index (RI), ejection elasticity index (EEI), and dicrotic reflection index (DRI) were calculated, using the fiducial points of the BPP, PPG, and SPH waveforms.

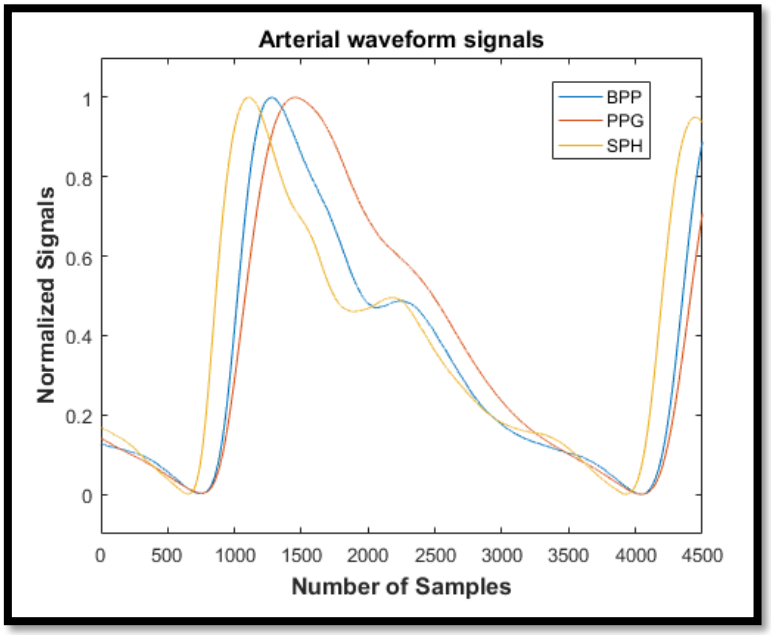

Figure 4.13: The PPG, BPP, and SPH arterial waveforms of subject 11

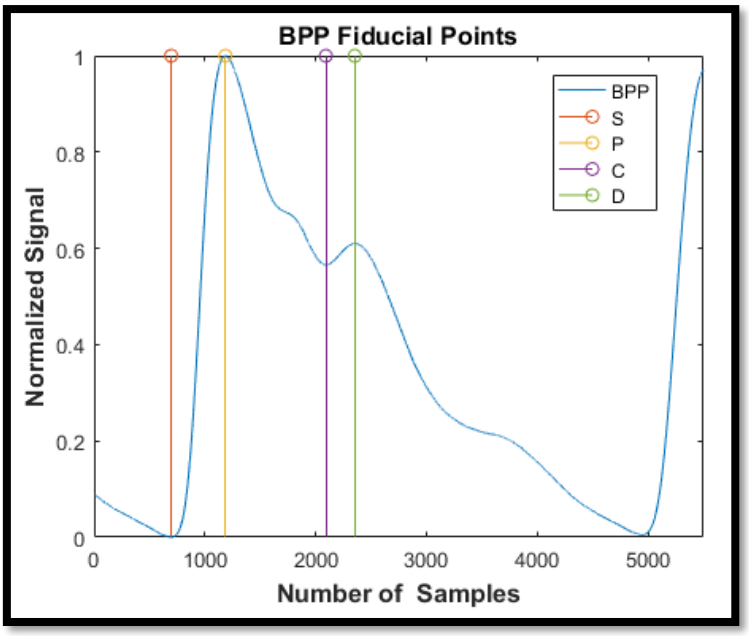

Figure 4.14: The fiducial locations for the BPP waveform of subject 11

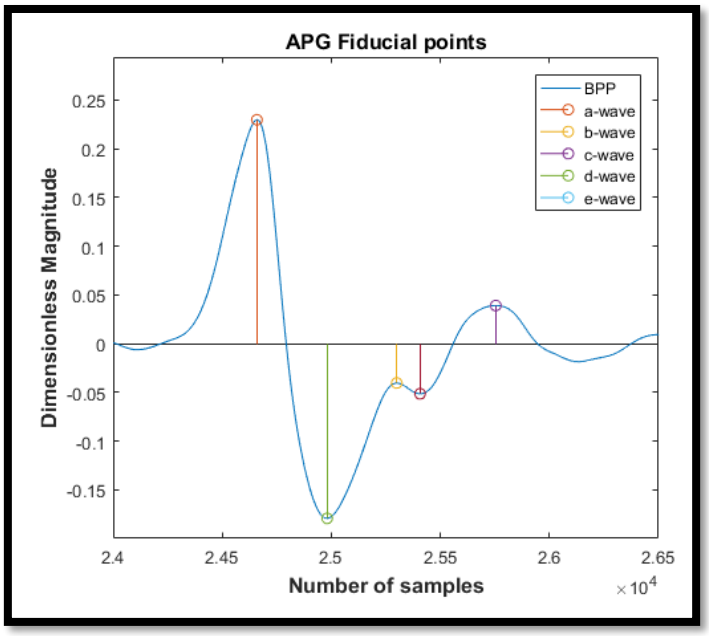

Figure 4.15: The accelerated BPP waveform fiducial locations of subject 11

4.3.6 Transfer Function

The radial artery branches from the wrist to the radial indics artery, in the distal phalanx, and was modelled using 2-element and 4-element WK models were estimated from the SPH waveform to the BPP waveform. Transfer function parameters were estimated using the MATLAB system identification toolbox.

4.3.7 Signal Processing

The text-formatted data were imported into the MATLAB platform (Mathworks, USA), for signal processing. Data were manually inspected, to remove artefacts and were cropped to obtain noise-free segments. The Pans-Tompkins algorithm [3] was used to detect and mark the ECG R-wave, which was used as the gating location for each cardiac cycle, for the remaining arterial signals. The PPG, SPH, and BPP signals were filtered using a least-squares technique, with a Savitzky-Golay filter, at –3 dB and 41 Hz. The algorithm was implemented for steady periods of the cohort data, on 10-second windows, as follows:

1. All signals were detrended and normalised.
2. ECG R-peaks were detected.
3. The ensemble averages of the PPG, BPP, and SPH signals were calculated for 10 cardiac cycles and signals within the standard deviation of $\pm$ 1 were used. The arterial waveform width for each cardiac cycle was set to 1.4 times the R-R interval, for each respective cycle.
4. The SPH, BPP, and PPG foot, peak, tidal, dicrotic notch peak, and foot fiducial points were detected.
5. The SI, RI, AI, AIx, elasticity index (EI), EEI, and DRI were calculated.
6. The 2- and 4-element WK model transfer function was calculated, using the system identification toolbox in MATLAB, for BPP to SPH signals.
7. The statistical analysis was performed.

4.3.8 Comparison of the Parameters– Statistical Analysis

The arterial index of the SPH waveform was compared against those for the PPG and BPP waveforms, individually. The agreement analysis was performed, via Bland-Altman analysis, and inter-rater agreement was performed, via weighted Kappa analysis. The regression analysis was used to find correlations among the parameters, and the Spearman’s rank correlation analysis was used to validate the lack of bias in the regression analysis.

4.4 Experimental Setup for the Pulse Transit Time Comparison Study

4.4.1 Aim and Objective

This experiment aimed to compare the pulse transit time (PTT) between the BPP and PPG waveforms. The objectives of the experiment were as follows:

1- Co-locate the PPG and BPP sensors on the index finger, using two pairs of sensors, in-line.
2- Compute and compare the PTT between the BPP and PPG waveforms

4.4.2 System Block Diagram

The system block diagram is shown in Figure 4.16. Two PPG and two BPP sensors were attached to an MP36R unit, to simultaneously capture the signals.

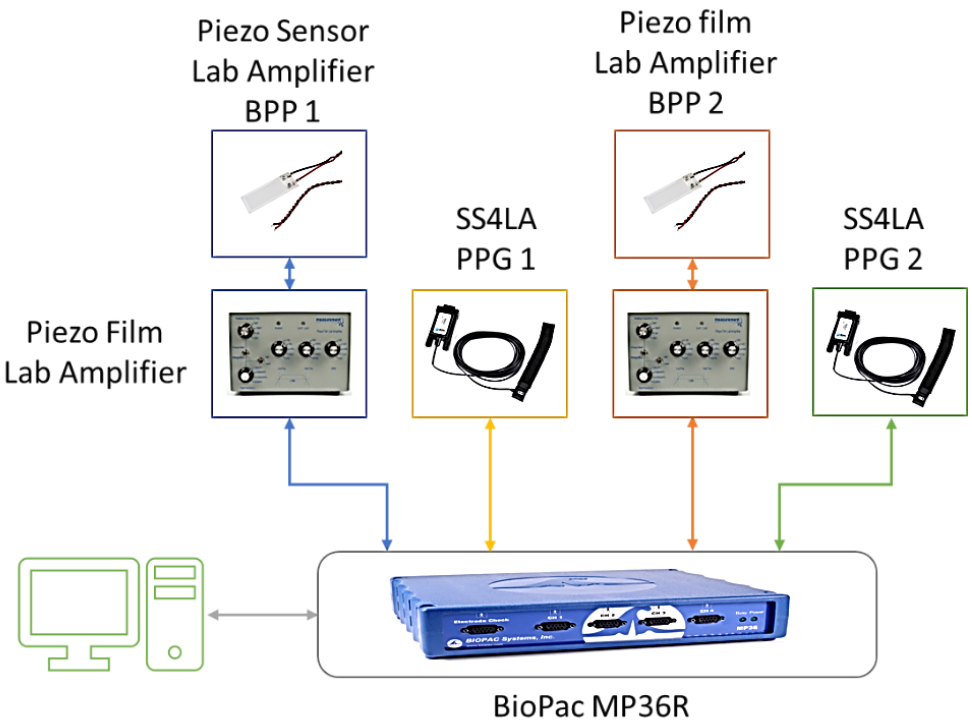

Figure 4.16: The sensor block diagram was used for the subject's data acquisition

4.4.3 Sensor Placement

Two PPG sensors were placed at the index finger, at the radial indices artery, and two BPPs were wrapped around the PPG sensors. A schematic for the sensors is shown in Figure 4.17.

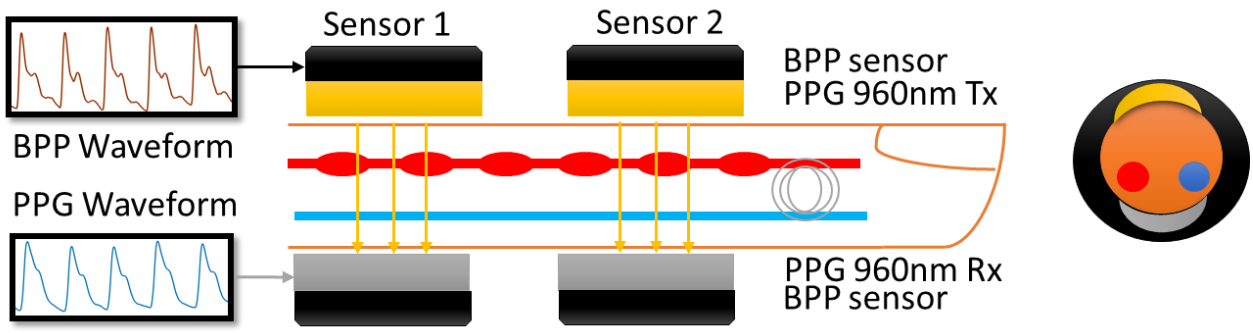

Figure 4.17: A schematic diagram, showing the lateral and cross-sectional views of the in-line sensor placement.

4.4.4 Fiducial Points

The peak of the first derivative, for each sensor, was marked, and the peak-to-peak delay between similar sensors was calculated.

4.4.5 Cross Comparison – Statistical Analysis

The cross-comparison between techniques was performed, to identify the most suitable physiological parameters and hence the sensing system for the application. The skewness was tested, and a repeated-measures ANOVA was performed, to identify significant differences between the PTT-BPP and PTT-PPG values. Agreement analysis and regression analysis were performed.

4.4.6 Signal Processing Algorithm

The signals captured from the acquisition unit, by using Acqknoweldge software, were exported in text format to MATLAB (R2018, MATLAB Inc.) software. The data were visually inspected, to remove artefacts, and cropped, to obtain clean signals. Savitzky-Golay filter was used to remove noise and higher frequency components. The steps of the algorithms are listed, as follows:

1- All signals were normalised and detrended.
2- The peaks of the first derivatives were calculated for all signals.
3- The PTTs were compared between the BPP and PPG waveforms.
4- The differences between the PTT values of each methodology were calculated.
5- The statistical analysis was performed.

4.5 Experimental Setup for the PWV and AIx Comparison Study – Data Fusion

4.5.1 Aim and Objective

The experiment aimed to test the data fusion possibilities for the BPP and PPG waveforms; therefore, the objectives are as follows:

1- Formulate a PU-loop, using the BPP and PPG waveforms.
2- Use the slope method to calculate the PWV.
3- Compute the Lissajous figure and calculate the phase-delay between the waveforms.
4- Validate the PWV and the phase-delay against the SphygmoCor Aortic Aix, using statistical comparison methods.

4.5.2 System Block Diagram and Sensor Placement

The experimental setup and sensor placement were identical to the experimental setup for the hemodynamic index study, except that the data from the SphygmoCor was captured in the SphygmoCor System Suite for the calculation of the aortic AIx.

4.5.3 Validation Sensor

The SphygmoCor system was used for the cross-validation mechanism, for the data fusion between the BPP and PPG waveforms.

4.5.4 Signal Processing Algorithm

The data acquired by the Biopac Acknowledge software was exported in Excel format, for processing in the MATLAB environment in PC (Window 10 OS). The algorithm steps used are described below:

1- A Savitzky Golay filter was used to remove the noise and determine the differences between the pressure and volume waveforms.
2- The ECG waveform R-peak was detected, using the Pan-Tompkins method [3].
3- BPP and PPG waveforms were ensembled, by gating the R-peaks, to remove signals outside of the standard deviation of $\pm$ 1.
4- The PU-loop was formed by plotting the difference between the BPP and PPG waveforms.
5- The PU-loops were normalised, and the slopes were manually drawn between

early systole (20%–30% of the BPP waveform).

6- The Lissajous figure was used to measure the phase lag and was normalised at an HR of 75 bpm
7- The statistical analysis was performed.

4.5.5 Comparison Method

The trends were compared between the data-fused PWV and the BP of the pilot study cohort. An agreement analysis was performed, via the Bland-Altman analysis, between the phase-lag and aortic AIx. The regression analysis was used to identify correlations between the phase-lag and the aortic Aix, and the Spearman's rank correlation analysis was used to validate the lack of bias in the regression analysis.

4.6 Summary

This chapter described the experimental designs used to collate a novel dataset for the comparison and validation of the various sensors and their waveforms, limited to healthy individuals only. The Biopac MP36R acquisition platform and all custom interfaces and associated sensors used in the study were described. Then, each experiment and their aims were described and their aims and objectives, system block diagrams, sensor placements, signal processing algorithms, the fiducial points on the arterial waveforms, the statistical methods, and the comparison techniques used to validate the arterial waveforms presented. These experimental studies focused on comparisons between the BPP sensor waveforms and the PPG sensor waveforms and on their validation against various techniques that represent gold standards for waveform measurement. First, HRV analysis techniques were used to validate the trackability and responsiveness of BPP and PPG sensors against the ECG gold-standard waveform. Second, the arterial indexes were validated against the SphygmoCor gold-standard tonometric waveform. Third, comparisons between the waveforms were performed, based on individual PTT measurements. And finally, the PU-loop and phase lag techniques were used to validate the fusion of information against the gold standard SphygmoCor aortic AIx index.

4.7 References

[1] A. V. Moço, S. Stuijk, and G. de Haan, “Skin inhomogeneity as a source of error in remote PPG-imaging.,” Biomed. Opt. Express, vol. 7, no. 11, pp. 4718–4733, Nov. 2016.

[2] Y. C. Chiu, P. W. Arand, S. G. Shroff, T. Feldman, and J. D. Carroll, “Determination of pulse wave velocities with computerized algorithms.,” Am. Heart J., vol. 121, no. 5, pp. 1460–70, May 1991.

[3] J. Pan, J. Willis, and W. J. Tompkins, “A Real-Time QRS Detection Algorithm,” IEEE Trans. Biomed. Eng., vol. 1, no. 3, pp. 230–236, Mar. 1985.

[4] J. Ramshur, “Design, evaluation, and application of heart rate variability software (HRVAS),” University of Memphis, Memphis, TN, USA, 2010.

[5] K. Takazawa, “Assessment of vasoactive agents and vascular aging by the second derivative of photoplethysmogram waveform.,” Hypertens. (Dallas, Tex. 1979), vol. 32, no. 2, pp. 365–70, Aug. 1998.

[6] J. Hashimoto, “Pulse wave velocity and the second derivative of the finger photoplethysmogram in treated hypertensive patients: their relationship and associating factors.,” J. Hypertens., vol. 20, no. 12, pp. 2415–22, Dec. 2002.

Chapter 5

Results and Discussions

5.1 Results for the Experimental Study Examining Heart Rate Variability Comparisons

The HRV analysis was used to compare the trackability and responsiveness of the BPP waveform against those of the PPG waveform and were validated against the ECG waveform, which is the gold standard for HRV analysis. The fiducial locations on the arterial waveforms that were used for the beat-to-beat intervals (B2BI) were the systole peak-to-peak interval, the first derivative peak to first derivative peak interval, and the second derivative peak to the second derivative peak interval, which were validated against the ECG waveform R-peak to R-peak interval, to examine the HRV analysis parameters. The significant HRV analysis parameters that were used for these comparisons are presented in Table 5.1.

Table 5.1: Time, frequency, non-linear, Poincare, and time-frequency domains of the HRV parameters that were used for the comparison analysis

Time Domain					
SDNN	pNN50	RMSSD	sdHR	HRVTi	TINN
(ms)	(%)	(ms)	(bpm)	(ms)	(ms)
Frequency Domain					
Welch periodogram, Auto-Regressive periodogram, and Lomb-Scargle periodogram					
pVLF	pLF	pHF	VLF	LF	HF
	(%)			Peak (Hz)	
Nonlinear Domain				**Poincare**	
SampEn	alpha	alpha1	alpha2	SD1	SD2
				(ms)	
Time-Frequency Domain					
Auto-Regressive, Lomb Periodogram, and Wavelet Transform					
pVLF	pLF	pHF	VLF	LF	HF
	(%)			Peak (Hz)	

*SDNN= Standard deviation of NN intervals, pNN50= Percentage of successive RR intervals that differ by more than 50 ms, RMSSD= Root mean square of successive RR interval differences, sdHR=Standard deviation HR, HRVTi= HRV triangular index,

TINN=Triangular Interpolation of the NN Interval Histogram, VLF=very-low-frequency band, LF=Low-Frequency, HF= High Frequency, p=Peak, SampEn=Sample Entropy, SD1= Poincaré plot standard deviation perpendicular the line of identity, SD2= Poincaré plot standard deviation along the line of identity alpha = Approximate entropy, which measures the regularity and complexity of a time series , alpha1= Detrended fluctuation analysis, which describes short-term fluctuations and alpha= Detrended fluctuation analysis, which describes short-term fluctuations.

The graphical user-interface options used for the HRV analysis software are shown in Appendix A, compared against their corresponding waveforms. The baseline noise and ectopic beats were removed from the beat-to-beat intervals of each waveform, to avoid artefacts during the comparison. The regression analysis was performed to determine the associations and the strength of the relationships between the arterial waveforms, and Spearman's rank correlation was used to verify that the regression was unbiased. The regression plots showing the ECG vs BPP and ECG vs PPG comparisons, for each fiducial point, are shown in Figure 5.1 (a-f). The regression *'r^2'* values and Spearman's *'rho'* values, along with the significance levels, are tabulated in Table 5.2, arranged in ascending order based on the *'r^2'* value.

Table 5.2: Regression analysis and Spearman's rank correlation for HRV parameters

	ECG R-peak		
	Regression	**Spearman's Rank Correlation**	
	r^2	rho	Significance level
PPG peak	0.9720	0.995	P < 0.0001
BPP second derivative peak	0.9659	0.984	P < 0.0001
PPG second derivative peak	0.9562	0.990	P < 0.0001
BPP peak	0.9484	0.990	P < 0.0001
BPP first derivative peak	0.9398	0.987	P < 0.0001
PPG first derivative peak	0.9247	0.988	P < 0.0001

The results for a cohort of 6 subjects, aged 34 $\pm$ 6 years, who were all male, showed that the highest overall *'r^2'* parametric fit was for the PPG waveform peak B2BI, followed by the BPP second derivative peak B2BI, whereas the lowest r^2 value was for the PPG first derivative peak B2BI, compared with the ECG R-peak to R-peak, for the HRV analysis. The highest Spearman's rank correlation *'rho'* values were also found for the PPG Peak B2BI and the BPP peak B2BI, whereas the lowest values were for the BPP second derivative peak B2BI. All the fiducial locations used for the

PPG and BPP waveforms showed very strong and significant positive associations with the ECG waveform, for all the HRV analysis parameters, based on the linear regression analysis.

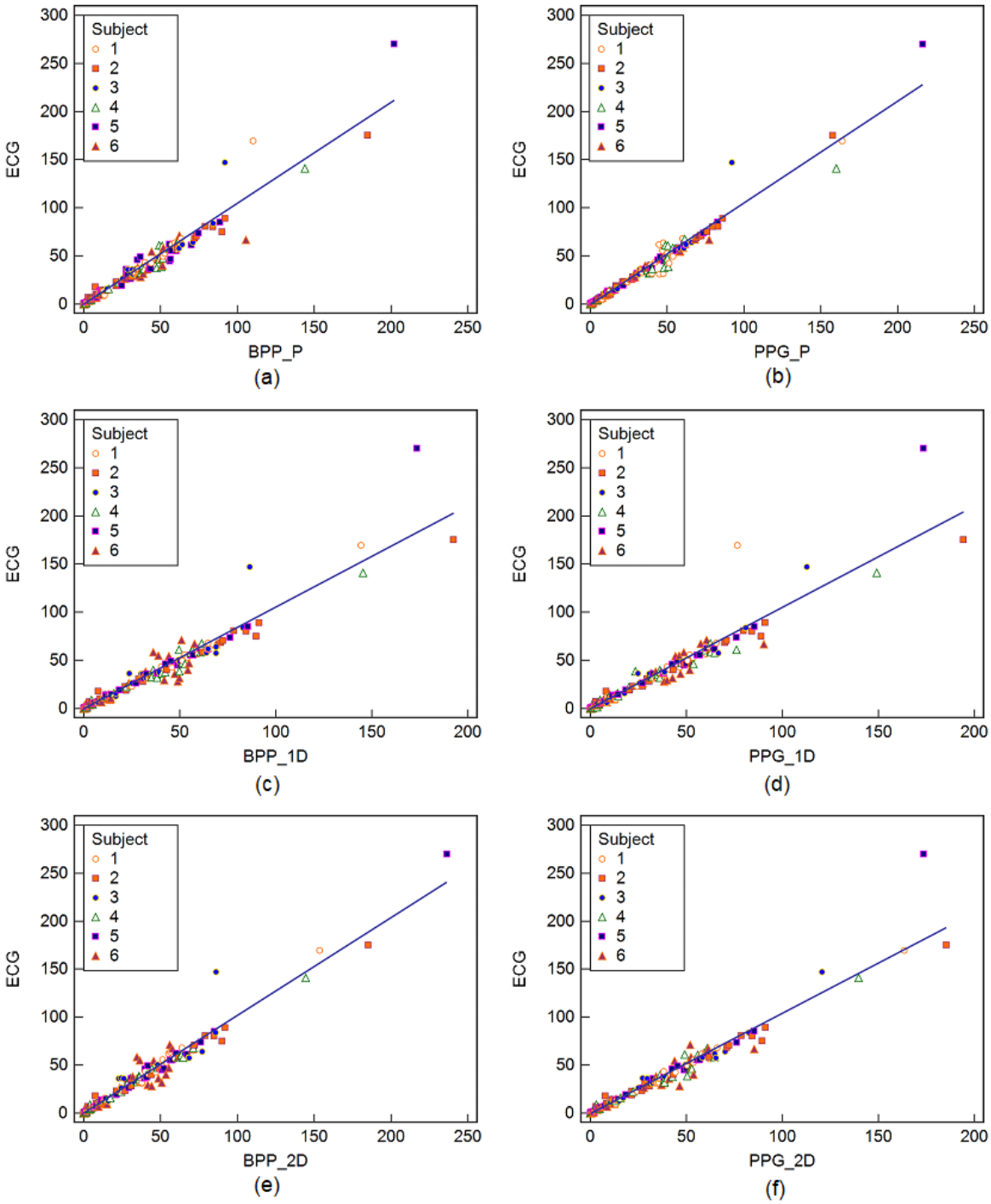

Figure 5.1: The regression analysis showing the ECG R-peak (ECG) vs a) the BPP Peak (BPP_P), b) PPG peak (PPG_P), c) BPP first derivative peak (BPP_1D), d) PPG first derivative peak (PPG_1D), e) PPG second derivative peak (PPG_2D), and f) BPP second derivative peak (BPP_2D), individually, for the HRV analysis parameters

The agreement analysis was performed via a Bland-Altman analysis, and the plots are shown in Figure 5.2. The Bland-Altman systematic difference and the limits of agreement (LoA) are tabulated in Tables 5.3 and 5.4, respectively. All parameters in the agreement analysis rejected the null hypothesis, with p-values < 0.0001. The mean differences between the parameters observed in the Bland-Altman analysis were not significant distant from zero. The lowest systematic difference was identified for the BPP second derivative peak B2BI, whereas the highest difference was identified for the PPG first derivative peak B2BI. The lowest LoA was found for the PPG peak B2BI, whereas the PPG first derivative peak B2BI presented the highest LoA.

Table 5.3: The systematic differences in HRV, with reference to fiducial points

The fiducial locations of B2BI	**n**	**Differences against ECG R-peak B2BI**		
		Mean	SD	95% Confidence interval
BPP_P	288	-0.3320	7.4359	-1.1944 to 0.5304
BPP_1D	288	-0.4252	8.0396	-1.3576 to 0.5073
BPP_2D	288	-0.1401	5.9479	-0.8299 to 0.5498
PPG_P	288	-0.3400	5.6266	-0.9926 to 0.3126
PPG_1D	288	-0.4946	8.9467	-1.5323 to 0.5430
PPG_2D	288	-0.1688	6.8504	-0.9633 to 0.6258

Table 5.4: The limits of agreement among the HRV parameters, with references to fiducial points

Variable	**Limits of agreement against ECG R-peak B2BI**			
	Lower limit	95% Confidence interval	Upper limit	95% Confidence interval
BPP_P	-14.9064	-16.3820 to -13.4308	14.2424	12.7668 to 15.7180
BPP_1D	-16.1828	-17.7782 to -14.5874	15.3324	13.7370 to 16.9278
BPP _2D	-11.7979	-12.9782 to -10.6176	11.5178	10.3375 to 12.6981
PPG_P	-11.3681	-12.4846 to -10.2515	10.6881	9.5715 to 11.8046
PPG_1D	-18.0301	-19.8055 to -16.2547	17.0408	15.2654 to 18.8162
PPG_2D	-13.5955	-14.9549 to -12.2361	13.2579	11.8985 to 14.6174

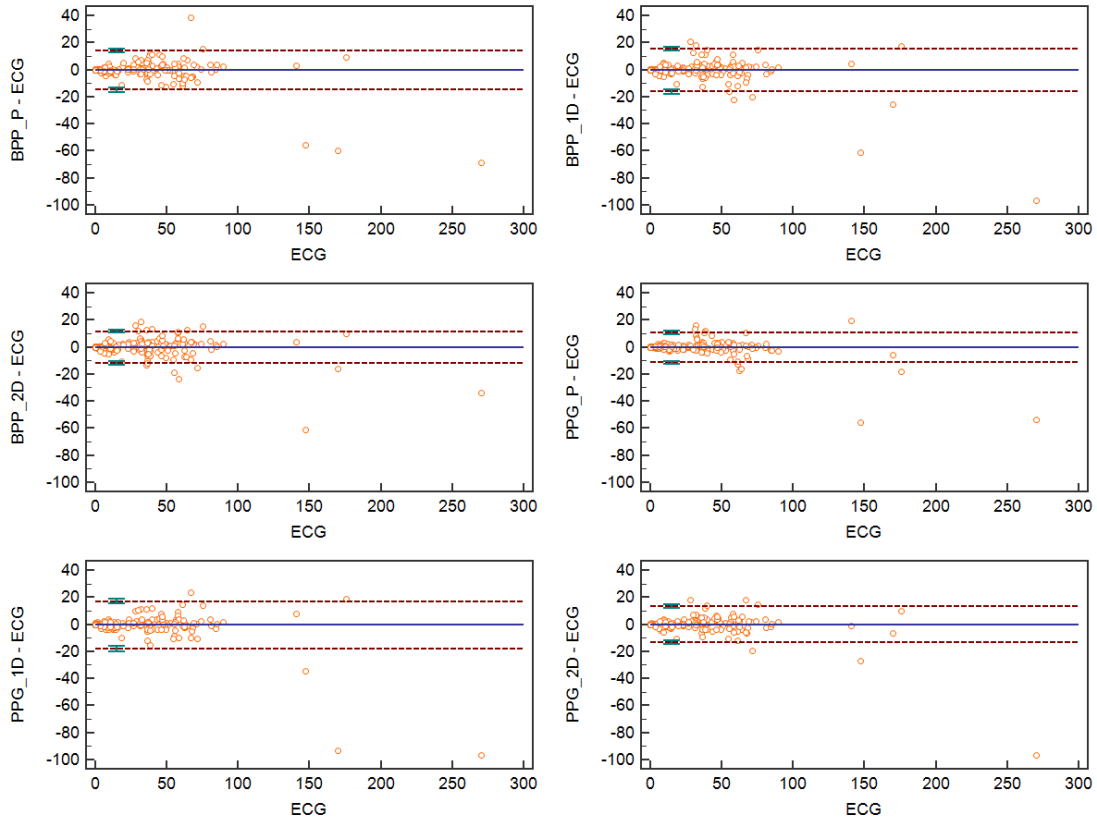

Figure 5.2: Combined B2BI Bland-Altman analyses of the ECG RR vs BPP waveform peak, first derivative, and second derivative and the ECG RR vs PPG waveform peak, first derivative, and second derivative, for HRV analysis

5.1.1 Discussion

HRV analysis has been very important in the early detection of cardiovascular disease. In the last decade, researchers have been examining potential ECG sensor alternatives, such as the PPG sensor, and this study represents an alternative in which the BPP sensor was tested for its responsiveness and trackability to perform HRV analysis compared with the ECG waveform.

PPG sensors have been widely applied both in intensive care units and GP clinics. Researchers have aimed to extract multiple streams of information from this sensor. PPG is very common in the wearable ambulatory setting, measuring HR and related parameters. PPG sensors perform very poorly in some situations, such as when the sensor makes poor contact with the skin due to excessive body movements, and in older patients and patients with low blood perfusion in the arteries. The BPP sensor can overcome many of these shortcomings but is also prone to motion artefacts, due to its high sensitivity.

This study focused on various fiducial B2BI locations on arterial waveforms, such as the systolic peak, the first derivative peak, and the second derivative peak, which have neither been compared simultaneously across different sensing methodologies. This novel dataset has unique advantages because all arterial waveform signals are processed using the same algorithms, presenting ideal conditions for true comparisons.

This study only focused on comparisons in young, healthy subjects, measured with the subject in a static sitting posture because the arterial flow waveforms are detected well in these situations and have been known to serve as surrogates for the ECG R-peak B2BI for HRV analyses [1]. The results of this study highly correspond to previously researched outcomes published found in the literature, for both regression analyses and agreement analyses, as stated in a review article by Schafer et al. [1].

In future studies, motion artefact removal, the validation of waveforms across both healthy and unhealthy subjects, and during exercise conditions will greatly add to the body of biomedical research knowledge.

During this comparative study, the BPP second derivative peak B2BI and the PPG peak B2BI were found to serve as surrogates for the ECG R-peak B2BI for accumulative HRV analysis parameters. These results verify the responsiveness and effectiveness of BPP waveforms compared with the state-of-the-art PPG waveforms. These results provide confidence for the performance of further investigations that rely on arterial waveform morphological analyses.

5.2 Results for the Experimental Study Comparing Arterial Indexes

Comparisons were performed for the AIx, AI, SI, RI, EEI, and DRI, on a cohort of 11 healthy subjects, aged 36 $\pm$ 6 years, who were all male. The agreement analysis was performed via Bland-Altman analysis, comparing 1) PPG waveform arterial indexes with SPH waveform arterial indexes, and 2) BPP waveform arterial indexes with SPH waveform arterial indexes, individually, as shown in Figure 5.3, arranged in ascending order with respect to LoA scores and tabulated in Table 5.5. The indexes calculated from the BPP waveforms demonstrated a narrower/closer limit of agreement (LoA) than indexes calculated from the PPG waveform, compared to the SPH waveform, individually. The index comparison, based on LoA, highlighted the increased accuracy

of the BPP waveform compared with that of the PPG waveform, with RI and AIx presenting the closest/narrowest LoA and EEI showing the highest LoA.

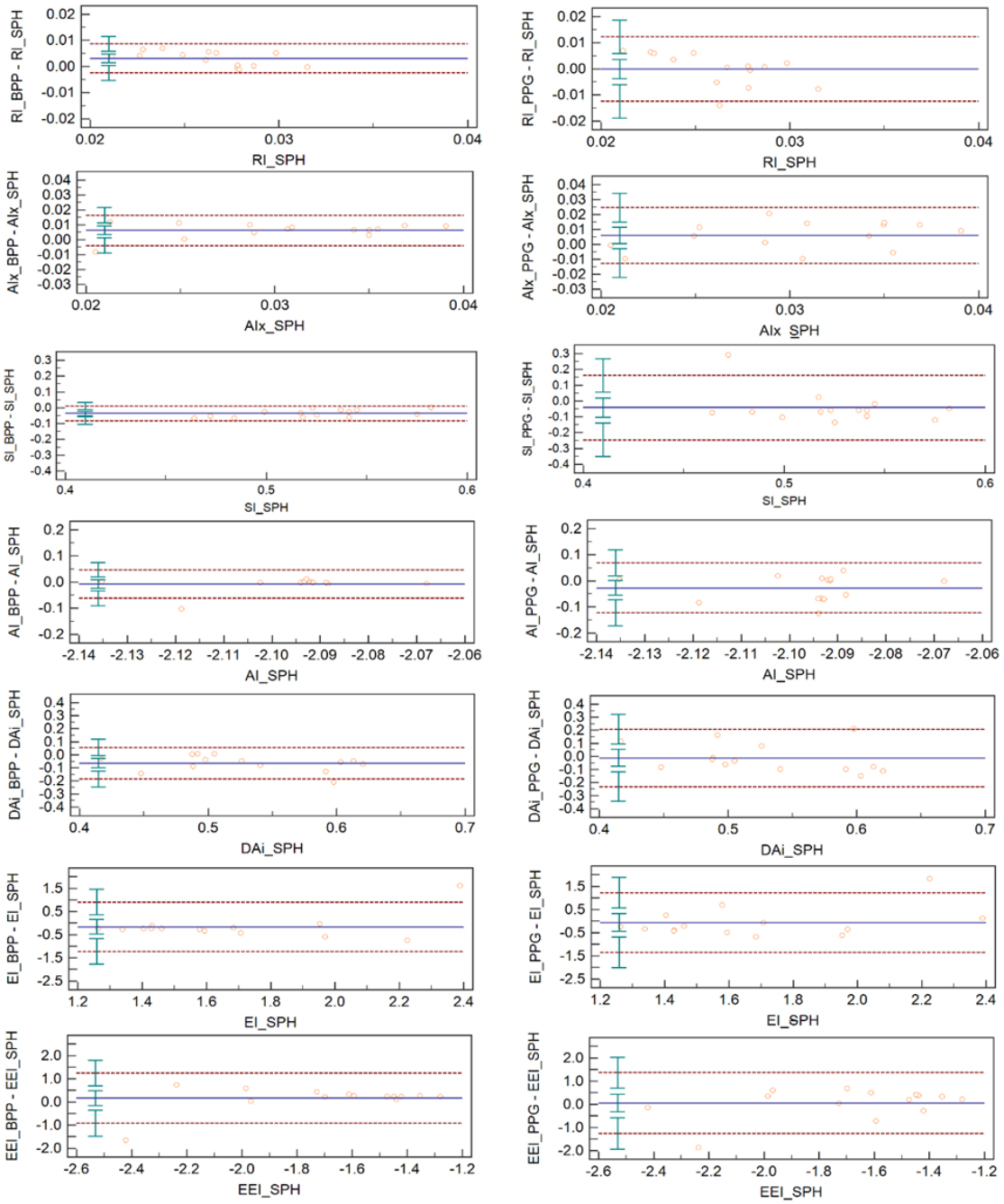

Figure 5.3: The Bland-Altman Analysis of Indexes, BPP vs SPH (on left) and PPG vs SPH (on right)

TABLE 5.5: The parameters for Bland-Altman and Kappa analysis between SPH waveform to BPP waveform (left) and SPH waveform to PPG waveform (right)

BPP Indexes Vs SPH Indexes

Ind	Kappa	Systematic Difference			Limit of Agreement			**PPG Indexes Vs SPH Indexes** Kappa	Systematic Difference			Limit of Agreement		
		LoA	Mean	SD	Lower limit	95% CI	Upper limit	95% CI	LoA	Mean	SD	Lower limit	95% CI	Upper limit	95% CI
AI	0.5596	0.1089	-0.0074	0.0278	-0.0619	-0.0899 to -0.0338	0.0470	0.0189 to 0.0751	0.2394	0.1906	0.0486	-0.0264	-0.1217	-0.1709 to -0.0725	0.0689	0.0197 to 0.1181
SI	0.3950	0.0923	-0.0356	0.0236	-0.0817	-0.1056 to -0.0579	0.0106	-0.0133 to 0.0344	-0.0445	0.4082	0.1041	-0.0413	-0.2453	-0.3507 to -0.1400	0.1628	0.0575 to 0.2682
DRI	0.2705	0.2415	-0.0635	0.0616	-0.1842	-0.2465 to -0.1219	0.0573	-0.0050 to 0.1196	0.0539	0.4389	0.1120	-0.0111	-0.2306	-0.3438 to -0.1173	0.2083	0.0951 to 0.3216
AIx	0.2425	0.0203	0.0063	0.0052	-0.0038	-0.0091 to 0.0014	0.0164	0.0112 to 0.0216	0.2543	0.0374	0.0095	0.0061	-0.0126	-0.0222 to -0.0029	0.0247	0.0151 to 0.0343
EEI	0.2425	2.1539	0.1631	0.5495	-0.9138	-1.4695 to -0.3581	1.2401	0.6843 to 1.7958	0.2394	2.6108	0.6660	0.0544	-1.251	-1.9246 to -0.5774	1.3598	0.6862 to 2.0334
EI	0.2425	2.1303	-0.1618	0.5435	-1.227	-1.7766 to -0.6773	0.9034	0.3537 to 1.4530	0.2394	2.5695	0.6555	-0.0609	-1.3457	-2.0087 to -0.6828	1.2238	0.5608 to 1.8867
RI	0.1407	0.0111	0.0032	0.0028	-0.0023	-0.0052 to 0.0005	0.0087	0.0059 to 0.0116	-0.0496	0.0247	0.0063	-0.0001	-0.0124	-0.0188 to -0.0060	0.0123	0.0059 to 0.0187

*Ascending order based on weighted Kappa values among the indexes

To validate the trends shown by the Bland-Altman analysis, a weighted Kappa analysis (WKA) was used. In the WKA, among the various indexes, compared between SPH

waveforms and BPP waveforms, the AI and SI indexes (at the top, in ascending order) showed moderate relationships, whereas the remaining indexes showed fair relationships, except for RI which showed only a slight relationship. The WKA among various indexes, compared between the SPH waveform and the PPG waveform, showed that AIx, AI, EI, and EEI showed fair relationships, whereas the remaining indexes showed no relationship (none < 0. 2> slight < 0.4 > fair < 0.6 > moderate < 0.8 > perfect < 1).

Table 5.6: The regression and Spearman's rank analyses for arterial indexes. SPH against BPP is shown on the left and SPH against PPG is shown on the right

SPH Indexes Vs							
	Spearman's Rank Correlation		Linear Regression		Spearman's Rank Correlation		Linear Regression
Indexes	**Significance level**	**rho**	**r^2**	**Indexes**	**Significance level**	**rho**	**r^2**
AIx BPP[1]	P < 0.0001	0.925	0.702	**AIx PPG[7]**	P = 0.0093	0.666	0.5125
EI BPP[2]	P < 0.0001	0.903	0.5625	**EI PPG[9]**	P = 0.0138	0.64	0.5041
SI BPP[3]	P < 0.0001	0.895	0.8628	**SI PPG[4]**	P < 0.0001	0.895	0.00418
EEI BPP[5]	P < 0.0001	0.881	0.5705	**EEI PPG[10]**	P = 0.0246	0.596	0.499
AI BPP[6]	P = 0.0012	0.771	0.4959	**AI PPG[11]**	P = 0.0666	0.503	0.1318
DRI BPP[8]	P = 0.0138	0.64	0.3746	**DRI PPG[13]**	P = 0.9346	0.0242	0.0788
RI BPP[12]	P = 0.2269	0.345	0.2347	**RI PPG[14]**	P = 0.8286	-0.0637	0.01566

*Ascending order, based on the rho values among the Indexes

Individual regression analyses were performed to identify correlations among the indexes associated with the BPP and PPG waveforms and those for the SPH waveform. The plots are shown in Figure 5.4. Similar results were observed for the regression analyses as were observed for the Bland-Altman analysis, with BPP waveform indexes showing stronger correlations with the SPH waveform indexes than the PPG waveform indexes. When the regression values were arranged in ascending order, the SI, AIx, EEI, and EI of the BPP waveforms showed the strongest correlations. Spearman's rank correlation was used to validate the trends identified by the regression analysis. The Spearman's rank correlation between the indexes of the BPP waveform and those of the SPH waveform showed that AIx, EI, SI (in ascending order), and EEI showed very strong positive correlations, whereas AI and DRI showed a strong correlation, and RI showed moderate correlation. In the Spearman's

correlation between the indexes of the PPG waveform and those of the SPH waveform, SI showed a strong positive correlation, whereas AIx, EI, EEI, and AI showed moderate positive correlations, and the remaining indexes showed very weak correlations, as shown in Table 5.6.

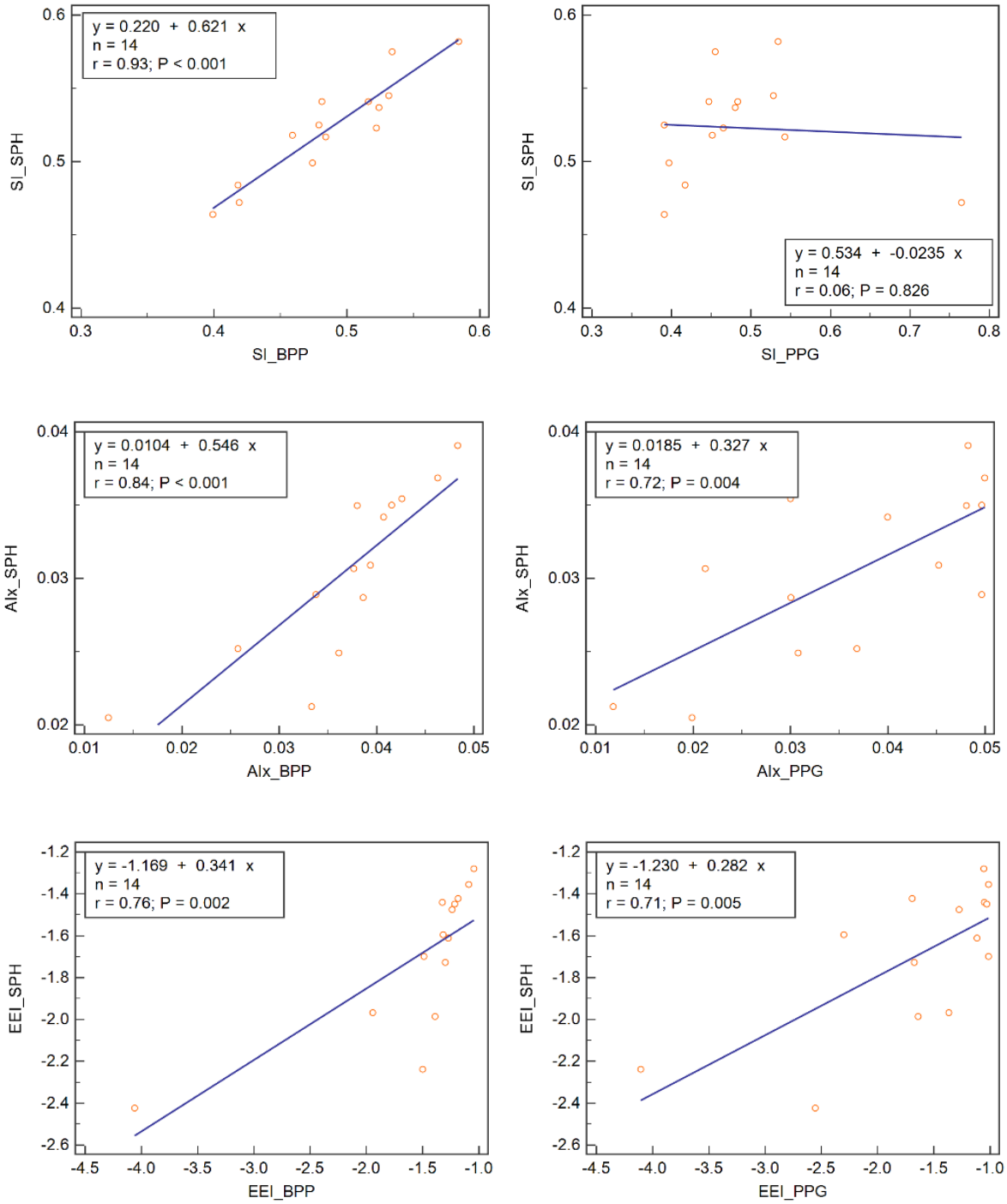

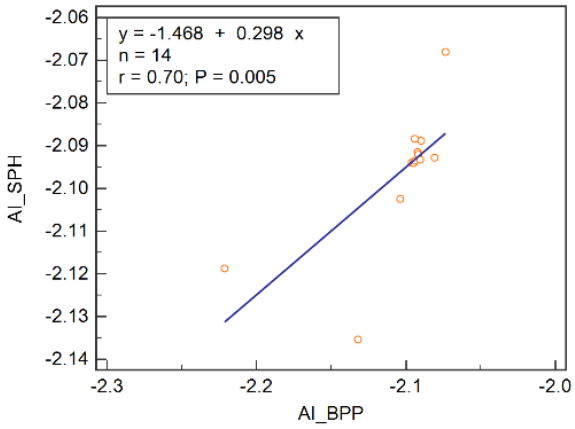
y = -1.468 + 0.298 x
n = 14
r = 0.70; P = 0.005
AI_SPH
AI_BPP

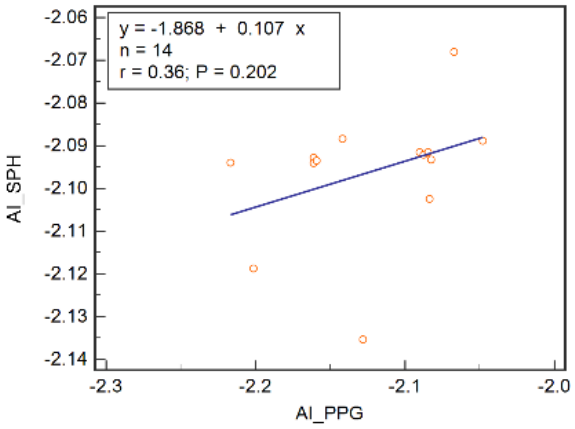
y = -1.868 + 0.107 x
n = 14
r = 0.36; P = 0.202
AI_SPH
AI_PPG

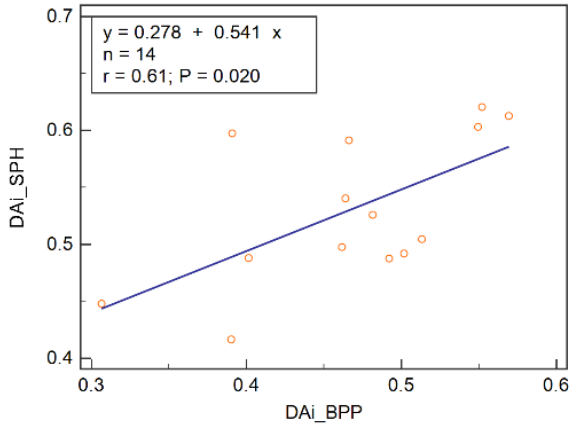
y = 0.278 + 0.541 x
n = 14
r = 0.61; P = 0.020
DAi_SPH
DAi_BPP

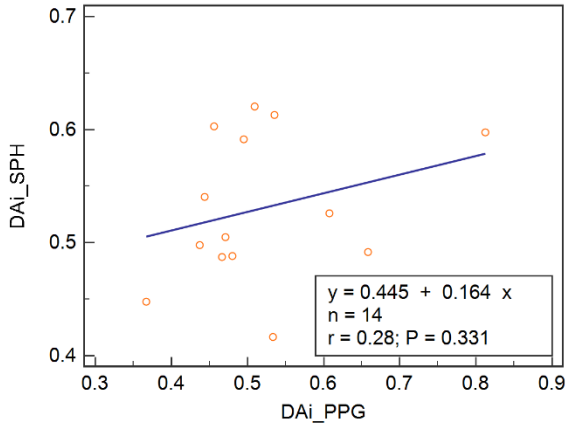
y = 0.445 + 0.164 x
n = 14
r = 0.28; P = 0.331
DAi_SPH
DAi_PPG

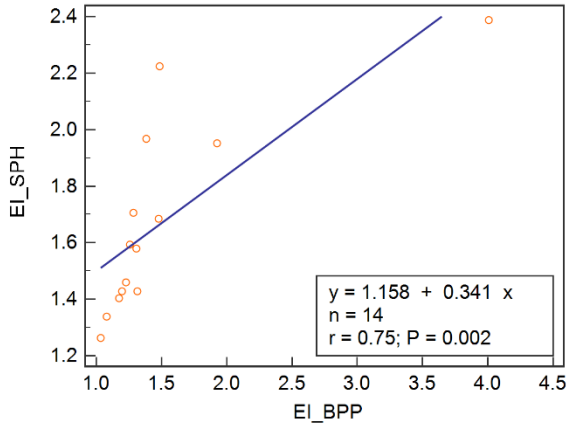
y = 1.158 + 0.341 x
n = 14
r = 0.75; P = 0.002
EI_SPH
EI_BPP

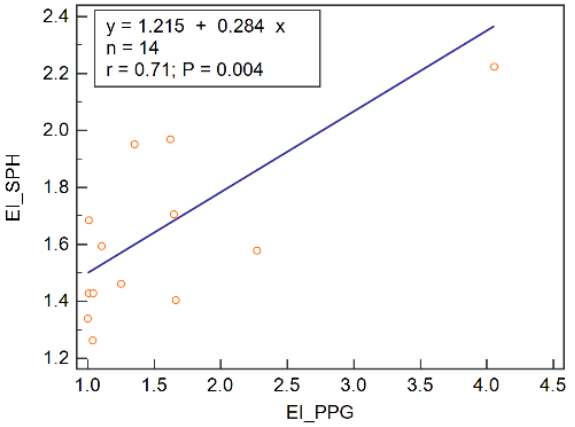
y = 1.215 + 0.284 x
n = 14
r = 0.71; P = 0.004
EI_SPH
EI_PPG

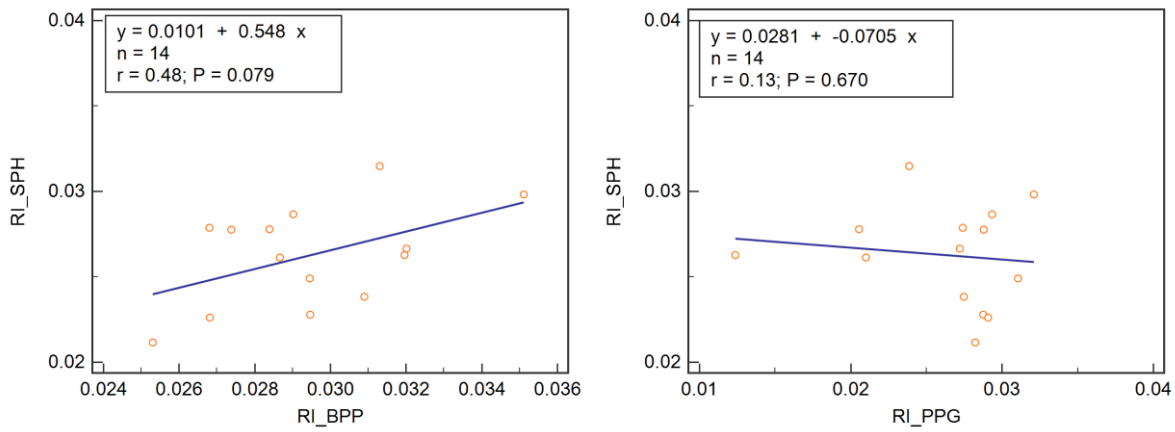

Figure 5.4. The regression analyses of arterial indexes, comparing the SPH waveform against the BPP waveform (left) and the PPG waveform (right)

5.2.1 The 2- and 4-element Windkessel (WK) Transfer Functions

For the radial artery, which branches from wrist to the distal phalanx in the index finger, the 2- and 4-element WK models were estimated for transforming the BPP waveform into an SPH waveform, using the MATLAB system identification toolbox. The parametric mean and standard deviation for the cohort is shown in Table 5.7. The accuracies of the individual transfer functions for the 2-element WK model were all higher than 85%, and the accuracies of the individual transfer functions for the 4-element WK model were all higher than 98%, as shown in Table 5.8.

Table 5.7: The 2- and 4- element WK model transfer functions and their parametric average values, for all subjects in the trial

2-element WK model	**4-element WK model**
$\frac{\boldsymbol{\alpha}}{\boldsymbol{s+\beta}}$	$\frac{\alpha_n s^2+\beta_n s+\gamma_n}{\alpha_d s^2+\beta_d s+\gamma_d}$
$\frac{(\mathbf{82.17})\pm\mathbf{37.13}}{\boldsymbol{s}+(\mathbf{75.90})\pm\mathbf{37.13}}$	$\frac{(0.90)\pm(0.1)s^2+(7.77)\pm(2.47)s+(66.89)\pm(29.46)}{s^2+(6.97)\pm(2.91)s+(61.02)\pm(24.57)}$

Table 5.8: Estimation accuracies of the 2- and 4-element WK models, for personalised transfer functions

Subjects	4-element WK accuracy (%)	2-element WK accuracy (%)
1	98.43	88.94
2	96.76	88.87
3	98.33	88.22
4	96.07	77.64
5	97.62	76.76
6	98.1	83.26
7	98.18	88.09
8	96.96	77.57
9	98.18	83.76
10	98.91	87.78
11	96.94	83.9

5.2.2 Discussion

The BPP AIx index performed the best compared with the SPH waveform, for all parameters examined. The overall best performances were obtained for the AI, EEI, and SI indexes for the BPP waveform, which agrees with the parametric results reported by Wowern et al. [2]. However, in our study, BPP outperformed PPG for all indexes, both individual and overall. The DRI showed a weak but significant relationship, whereas RI showed almost no significant relationship among the examined BPP parameters.

The APG demarcation of the fiducial wave is mathematically complex and intensive and becomes even more difficult for the PPG waveform, as the tidal wave is not very visible. In contrast, for the BPP waveform, the tidal wave was visible in all subjects. This inconsistency has also been reported elsewhere [3]. The dicrotic notch and the tidal wave are both consistently visible in the BPP waveform, as observed in this study, which makes the BPP waveform superior to the PPG waveform.

The clinical associations have been well-established in the literature for the AIx and AI indexes [2][4] and their relationships with CVD; however, the reverification or establishment of any such relationships among healthy and diseased groups was outside of the scope of this study.

Due to the high sensitivity of the PVDF sensor to mechanical vibration, BPP waveform sensing may be limited to stable postures, to avoid motion artefacts. Identifying a method that allows the BPP measurement to be measured and signal information to be extracted even in the presence of motion artefacts remains an important developmental goal.

The 2-element WK model represents a simple function and can be easier to interpret for person-specific parameters, which may make adaptive tracking possible (which is suggested for future work), as has been suggested by Mukkamala et al. [5].

BPP is independent of the subject's skin colour and cosmetic effects on the skin surface, unlike the PPG waveform. BPP can also be performed in an operator-less manner, which makes it an attractive method compared with the SPH waveform.

In conclusion, the BPP waveform measurement technique is advantageous because it can be performed unaided and is cheaper and easier to use than conventional tonometric devices. BPP waveforms also outperform the conventional PPG waveform for all indexes. As it can be incorporated into wearable technologies, thus the better assessment of arterial indexes, the BPP waveform may facilitate the early detection and prevention of CVD.

5.3 Results for the Experimental Study Comparing the Pulse Transit Time

The PTT-PPG, PTT-BPP, and their trend plots, using the 9^{th} order polynomial, are shown in Figure 5.5. The cohort data obtained on 7 subjects, aged 32 ± 4 years, who were all male, showed higher average PTT-BPP valuesan increase of 11 ms, compared with that for PTT-PPG. The data from three subjects were discarded from the analysis as their PTT-PPG waveforms showed cross-over with the PTT-BPP waveforms with no observable physiological changes were observed in the subject's mood or stated in the questionnaire response.

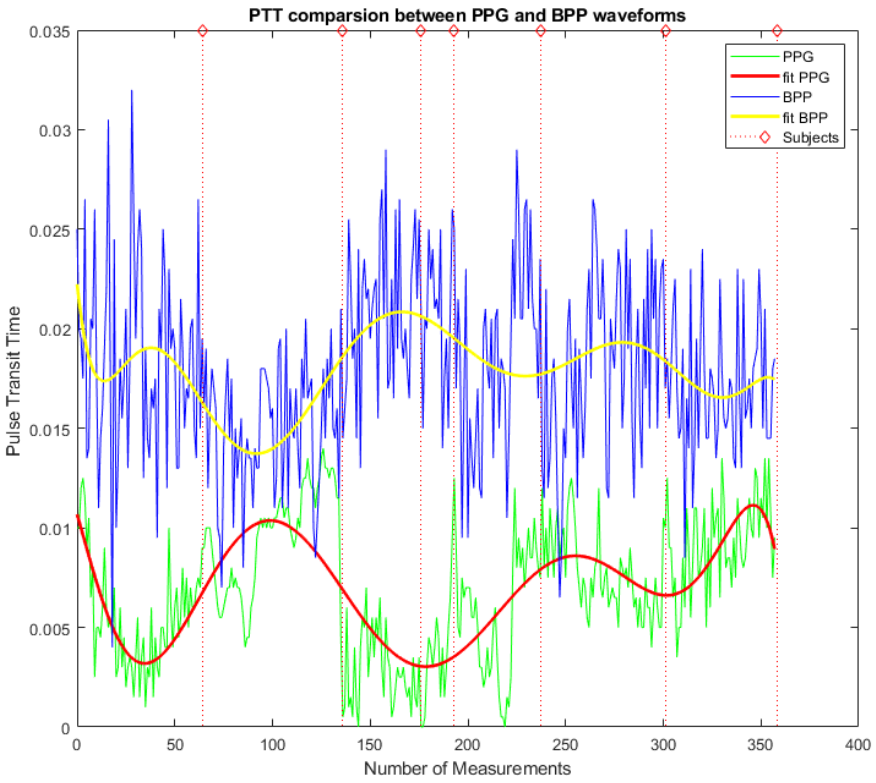

Figure 5.5: PTT-PPG and PTT-BPP values of the cohort, and their data trends

The histograms for PTT-BPP and PTT-PPG are calculated, as shown in Figures 5.6 and 5.7, respectively. Both waveforms showed normal distributions, as can be observed in the dotted waveform on the plots. The data were tested for skewness and none was found, for either the PTT-BPP or the PTT-PPG cohort datasets.

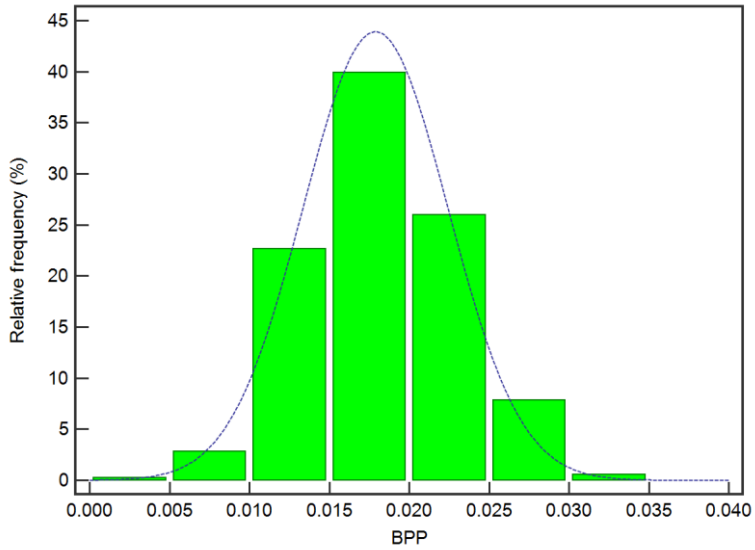

Figure 5.6: Histogram of PTT-BPP and its normal distribution

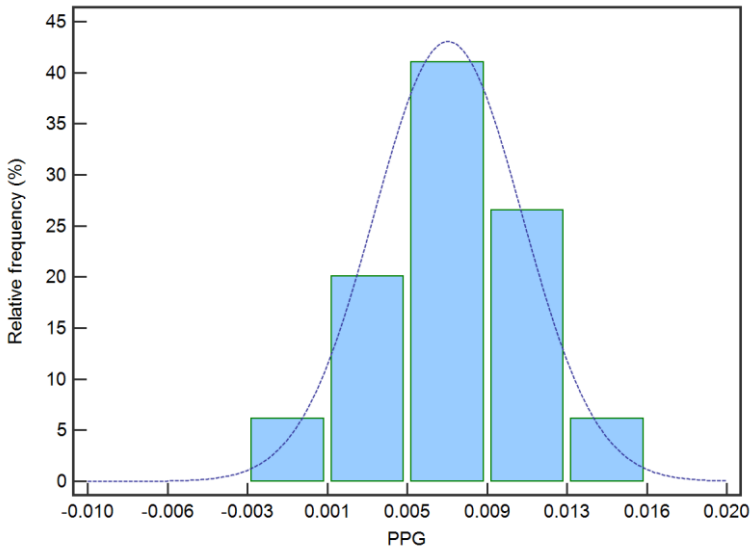

Figure 5.7: Histogram of PTT-PPG and its normal distribution

The PTT-PPG and PTT-BPP cohort datasets were tested using a repeated-measures ANOVA, and tests between subjects showed low p-values for both groups ($p < 0.05$), as shown in Table 5.10. Based on the p-values, there is a significant difference between the groups. A plot of the means, clustered by groups, is shown in Figure 5.8. The PTT-BPP waveform showed consistent behaviour, with a low standard deviation, for mean values, indicating that the measurement of the arterial waveform, based on the distension waveform, was consistent. Plotting the PTT-PPG against the persistent PTT-BPP plots showed intermittent behaviour for the PTT-PPG intervals, indicating weakness in tracking the waveform compared with the PTT-BPP.

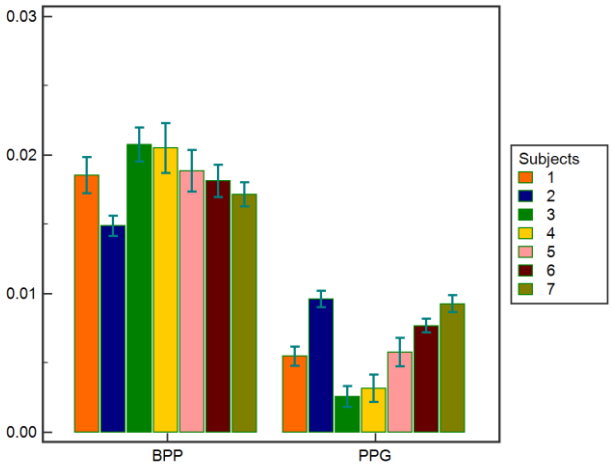

Figure 5.8: Repeated measures ANOVA plot between PTT-PPG and PTT-BPP

Table 5.9: Repeated-measures ANOVA

Source of variation	Sum of Squares	Degree of Freedom	Mean Square	F	p-value
Groups (Subjects)	0.000185	6	0.0000309	2.27	0.037
Residual	0.00478	351	0.0000136		

An agreement analysis was performed using a Bland-Altman analysis, as shown in Figure 5.9. The value of the LoA and the systematic differences are tabulated in Tables 5.11 and 5.12, respectively. Most of the dataset remains within the 95% confidence interval, although some outliers can be observed. No biases were detected in the dataset, as the systematic mean difference was near-zero, at 0.01097.

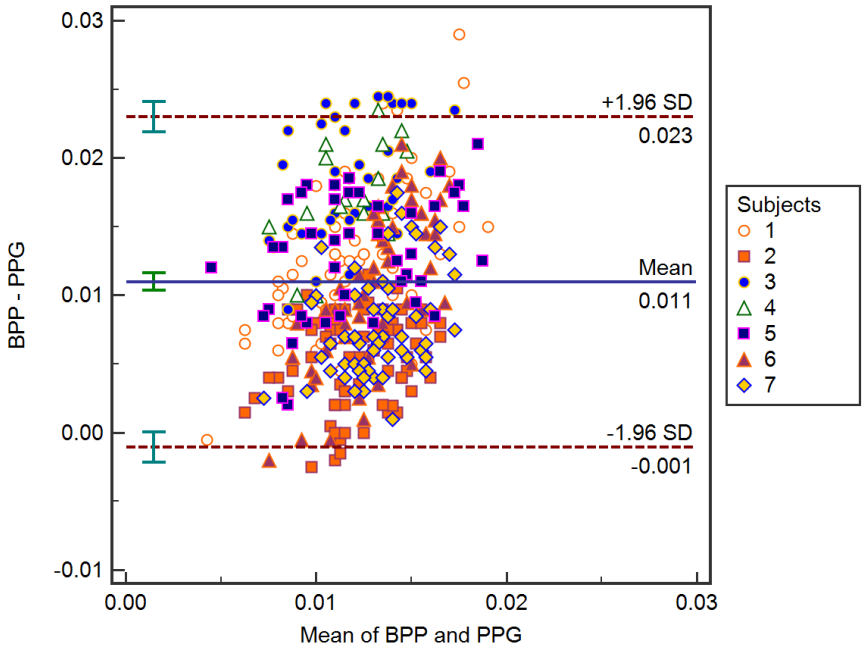

Figure 5.9: Bland-Altman analysis comparing PTT-BPP vs PTT-PPG for the cohort

Table 5.10: The Bland-Altman limit of agreement

Bland-Altman analysis Limits of agreement			
Lower limit	95% Confidence interval	Upper limit	95% Confidence interval
-0.001050	-0.002140 to 0.00004064	0.02299	0.02190 to 0.02408

Table 5.11: The Bland-Altman systematic difference

Bland-Altman analysis differences (%)		
Mean	**SD**	**95%** Confidence interval
0.01097	0.006132	0.01033 to 0.01161

To examine the relationship between the PTT-PPG and the PTT-BPP, regression analysis was performed, as shown in Figure 5.10. The regression analysis biases were tested using Spearman's rank correlation. Both analyses showed a very weak relationship, as expected, based on the non-consistent behaviours shown between the subjects' PTT-PPG and PTT-BPP.

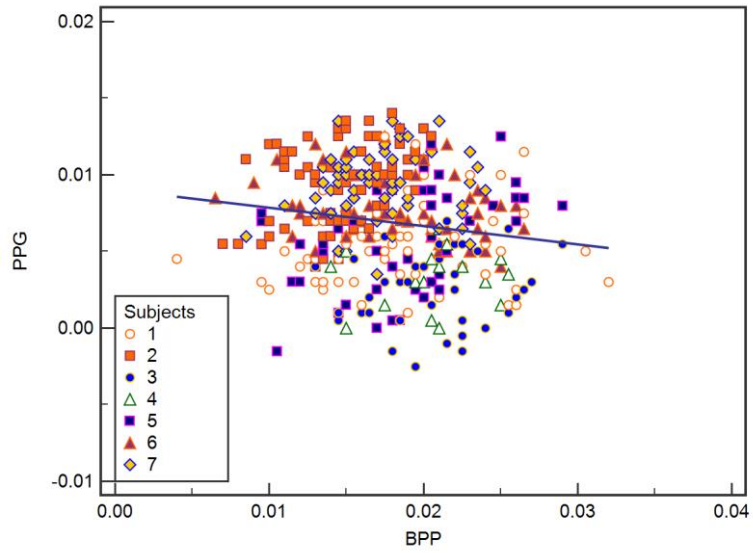

Figure 5.10: The regression analysis for PTT-PPG vs PTT-BPP

Table 5.12: The regression analysis and Spearman's rank correlation

PPG vs BPP for all subjects			
	Regression	**Spearman's Rank Correlation**	
Sample size	r^2	rho	Significance level
358	0.02405	-0.160	P = 0.0024

5.3.1 Discussion

The development of a non-invasive assessment for arterial stiffness has been of great interest during the last decade, especially with the rise of wearable technologies. The

PTT has shown higher estimation accuracies for the assessment of both SBP and DBP values. Research has focused on optical sensing, but no comparisons have been performed across different sensing methodologies, as researched in this study. A unique and novel comparison of PTT measurements has been presented, which may represent the first attempt to compare PTT between PPG and BPP sensing methodologies.

According to Womersley's arterial flow [6], the flow waveform lags the pressure wave by 90° in larger arteries. The BPP waveform sensing of distension waveforms can be directly associated with the pressure waveforms [7], which improves the assessment of PTT and reduces estimation errors. According to the results shown in Figure 5.8, the PTT-BPP has a steadier and faster response than the conventional PTT-PPG, which may improve the BP estimation accuracy based on PTT [8][9][10].

No viable source of cross-validation was available for these measurements, but the results can be supported by the experimental study of arterial indexes. The BPP waveform was validated against the SphygmoCor waveform and outperformed the PPG for the measurement of haemodynamic indexes, including the AIx, the AI, and the SI.

The PPG sensor measures the volumetric blood flow waveform, based on the oxygenation absorption of haemoglobin, which can vary, even for similar blood volumes. In this comparison, the IR wavelength used to measure the PPG waveform was less sensitive to oxygenation [11] levels but was not free from related artefacts. In contrast, the BPP waveform relies on the distension waveform, which does not produce artefacts associated with the oxygenation level of the blood, making it a superior investigation method.

The PTT-PPG graph showed cross-over with the PTT-BPP graph in three excluded subjects, which highlights the inconsistency of tracking PTT using the PPG waveform, whereas the PTT-BPP showed steadier behaviour. In the absence of any interventions intended to change BP, the existence of cross-over raises issues regarding the credibility of using PPG technology for the measurement of PAT/PTT-like parameters.

In conclusion, the higher precision and accuracy of the BPP waveform for sensing the morphology of the arterial waveform encouraged the comparison between BPP and

PTT measured using current state-of-the-art technology. A significant difference was observed between PTT-PPG and PTT-BPP, and higher consistency was found for the PTT-BPP values. Interestingly a very weak correlation was found among the dataset, and no biases were found in the agreement analysis.

5.4 Results for the Experimental Study Comparing PWV and AIx - Data Fusion

In the first section of this study, data was collated from 6 subjects, aged 34 $\pm$ 4 years (all male), and their absolute, unitless PWVs were calculated using PU-loop plots. The signal processing algorithm was applied to extract the ensemble averages of the arterial waveforms (BPP and PPG) and normalised PU-loop plots. An example of signal processing performed for subject 3 is shown in Figure 5.11. The slope was calculated based on 20%–30% systole for the BPP waveform on the PU-loop plot, resulting in the PWV, which is tabulated in Table 5.13. The normalised PU-loops for all subjects are shown in Figure 5.11. An increasing trend was observed for PWV with increasing BP. This absolute, unitless PWV measurement was derived from the normalisation of the ensembled arterial waveforms, which can predict changes in BP, based on PU-loop morphology.

Table 5.13: Dataset parameter and normalised PWV results

BP 1≥ BP 2	Age	H(cm)/W(kg) BMI	PWV (unitless)
139/98 ≥ 137/96	45	175/85 ≥ 27.76	2.89
118/77 ≥ 125/77	29	177/80 ≥ 25.54	2.00
116/71 ≥ 116/73	32	174/78 ≥ 25.76	1.75
121/71 ≥ 127/72	30	180/83 ≥ 25.62	1.28
119/66 ≥ 115/73	27	188/73 ≥ 20.65	1.11
117/67 ≥ 122/68	29	179/84 ≥ 26.22	1.24

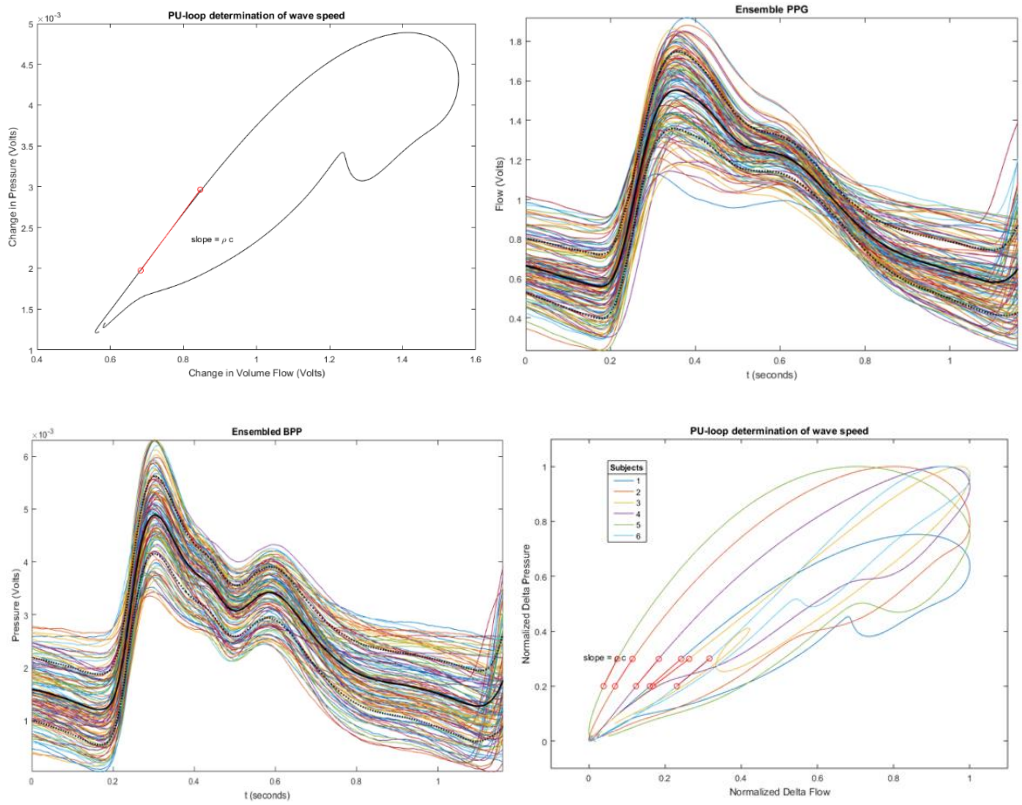

Figure 5.11: The ensembled average for subject 3, PPG signals (top right), BPP signals (bottom left), PWV slope (top left), and cohort PU-loop and local PWV (bottom right)

In the second part of the study, the phase lag between the BPP waveform and the PPG waveform was calculated, using a Lissajous figure plot, on cohort data from 12 healthy subjects, aged 36 $\pm$ 4 years (all male). The phase lag was normalised at an HR of 75 bpm, to confirm it with the value of the aortic AIx (adjusted at an HR of 75 bpm), taken from the SphygmoCor system, as shown in Figure 5.12.

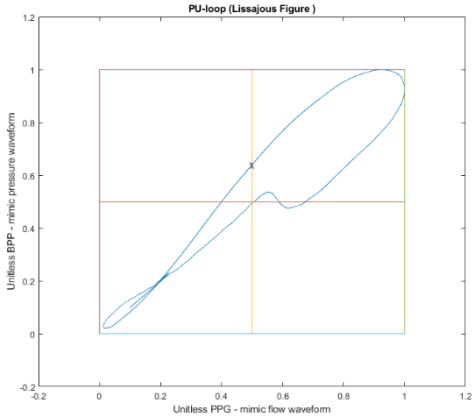

Figure 5.12: Lissajous Figure of the BPP and PPG waveform

The regression analysis showed a significant association with an 'r²' value of 0.71 between the phase-lag and the aortic AIx. The lack of bias was tested using Spearman's rank correlation, which showed stronger strength in a positive direction. The results are tabulated in Table 5.14, and the linear fit of the regression parameter is shown in Table 5.15.

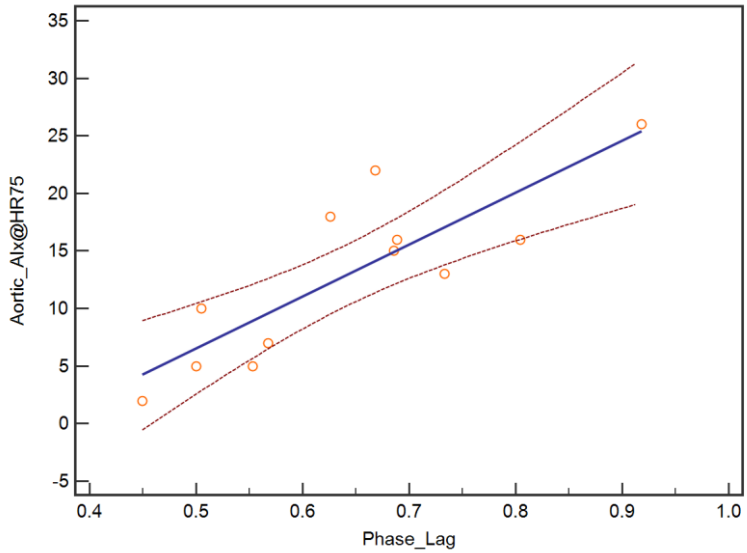

Figure 5.13: The regression analysis between Phase Lag and Aortic AIx

Table 5.14: The regression analysis and Spearman's rank correlation

Aortic AIx Vs Phase Lag - @ HR 75 bpm			
	Regression	**Spearman's Rank Correlation**	
Sample size	r^2	rho	Significance level
12	0.7099	0.779	P = 0.0028

Table 5.15: The regression line equation and parameters

Regression Equation					
y = -16.0993 + 45.2304 x					
Parameter	Coefficient	Std. Error	95% Confidence interval	t	P
Intercept	-16.0993	5.9860	-29.4369 to -2.7617	-2.6895	0.0227
Slope	45.2304	9.1431	24.8582 to 65.6026	4.9469	0.0006

The Bland-Altman agreement analysis was performed, and the plot is shown in Figure 5.14. The LoA and systemic difference values are tabulated in Tables 5.16 and 5.17, respectively. In the agreement analysis, bias was observed in the dataset, as the mean difference did not equal zero, which is the ideal value. To resolve this bias, the data difference was regressed around the mean of the groups, and the linear fit parameters are shown in Table 5.18.

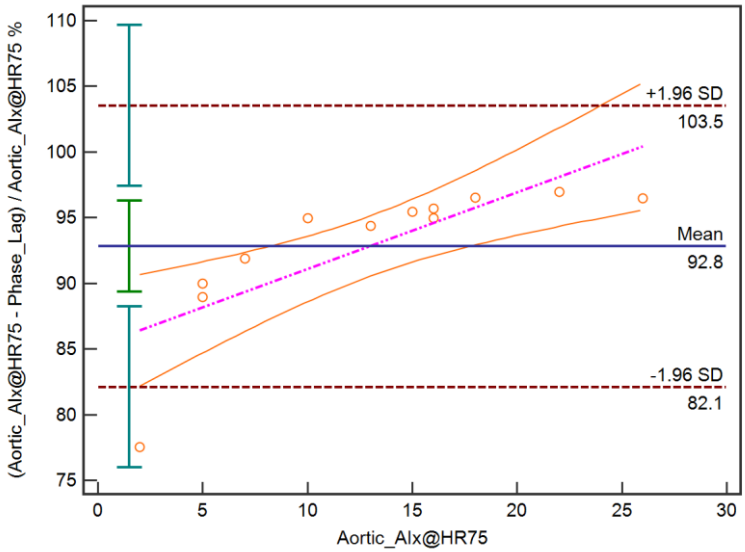

Figure 5.14: The Bland-Altman analysis between Aortic AIx and Phase Lag

Table 5.16: The Bland-Altman limits of agreement

Bland-Altman analysis- Limits of agreement			
Lower limit	95% Confidence interval	Upper limit	95% Confidence interval
82.0960	88.2066 to 75.9853	103.5243	109.6350 to 97.4136

Table 5.17: The Bland-Altman systematic differences

Bland-Altman analysis- Differences (%)		
Mean	**SD**	**95%** Confidence interval
92.8101	5.4664	96.2833 to 89.3369

Table 5.18: The Bland Altman analysis regression line parameters

Bland-Altman analysis - Regression line					
Regression Equation			y = 85.2774 + 0.5832 x		
Parameter	**Coefficient**	**SE**	**t**	**P**	**95%** Confidence interval
Intercept	85.2774	2.1612	39.4588	<0.0001	80.4620 to 90.0928
Slope	0.5832	0.1470	3.9666	0.0027	0.2556 to 0.9108

5.4.1 Discussion

The non-invasive assessment of BP, using PAT or PTT techniques, shows a close relationship with BP, often fails to track sudden changes in BP. The current methodology of cuffless BP monitoring requires frequent brachial BP inputs to calibrate the measurement. This work attempted to contextualise the calibration requirement by using PWV and/or phase-lag for the PTT estimation of BP. These results will provide adaptive feedback for the correcting factor in the Moen-Korteweg PWV equation, as suggested by the author [12].

The mandate of the study was to explore the feasibility of formulating a PU-loop and phase-lag calculation, to act as a calibration mechanism. The quantisation of the BPP and PPG waveforms is necessary to obtain greater insights into the biomechanical markers. In the current method, the normalised waveforms were used to evaluate the morphology of the PU-loop among the subjects (suggested future work should compare hypertensive and normotensive groups). The hydrostatic and gravitational effects were neglected in these experiments, based on the assumption of similar sitting postures in an armchair, for all subjects. The BPP sensor scalability and repeatability of the experiment were very encouraging.

This method is advantageous because it can estimate the AIx from a single location, noninvasively, compared with the conventional measurement using the SphygmoCor system. This method is operator-independent, cheaper and well-suited for development based on wearable applications.

The non-invasive measurement of phase-lag at a distal artery highly correlates with the results reported by Womersley et al. [6], which also implies the superiority of the BPP waveform compared with the PPG waveform.

In conclusion, a novel, non-invasive, single-location assessment method for PWV and phase lag has been developed. The results successfully demonstrated that the phase-lag between the BPP and PPG waveforms was strongly correlated, with an *'r^2'* value of 0.71, with the aortic Aix, as measured using the SphygmoCor tonometric device.

5.5 Summary

In summary, a novel dataset was collated containing arterial waveforms detected using various sensing methodologies. The sensing methodologies were based on the volumetric waveform, the distension waveform, and the tonometric waveform of arterial waveforms, facilitating a unique, cross-methodology comparison and validation. A novel sensor, the BPP, was compared against the state-of-the-art PPG sensor and validated against various gold standards. The results of experimental studies comparing HRV evaluation methods laid the foundation for this present research study, which validated the responsiveness and trackability of a BPP sensor against the gold-standard ECG waveform. The results of the experimental study comparing arterial indexes demonstrated the higher accuracy and precision of the BPP sensor waveform compared with the state-of-the-art PPG sensor waveform. The BPP sensor waveform was validated against the gold standard tonometric device waveform. Furthermore, this study established the feasibility of developing an operator-independent and wearable surrogate for the tonometric device. The results of the experimental study comparing PTT values highlighted the shortcomings of the current state-of-the-art PPG sensor and showed the superiority, stability, and consistency of the BPP sensor waveform for the assessment of PTT. Finally, the results of the experimental study comparing PWV and AIx values were used to devise and verify a novel data fusion method, for the single-location assessment of arterial stiffness, which may help track sudden changes in BP using PTT techniques. These results will assist with the prognosis and diagnosis of CVD, using a cuffless BP measurement, especially arterial stiffness, and hypertension.

5.6 References

[1] A. Schäfer and J. Vagedes, “How accurate is pulse rate variability as an estimate of heart rate variability?: A review on studies comparing photoplethysmographic technology with an electrocardiogram,” International Journal of Cardiology, vol. 166, no. 1. pp. 15–29, 2013.

[2] E. von Wowern, G. Östling, P. M. Nilsson, and P. Olofsson, “Digital Photoplethysmography for Assessment of Arterial Stiffness: Repeatability and Comparison with Applanation Tonometry,” PLoS One, vol. 10, no. 8, p. e0135659, 2015.

[3] S. C. Millasseau, J. M. Ritter, K. Takazawa, and P. J. Chowienczyk, “Contour analysis of the photoplethysmographic pulse measured at the finger,” J. Hypertens., vol. 24, no. 8, pp. 1449–1456, Aug. 2006.

[4] M. F. O’Rourke and D. E. Gallahger, “Pulse wave analysis,” J. Hypertens., vol. 14, pp. 147–157, 1996.

[5] R. Mukkamala, “Toward Ubiquitous Blood Pressure Monitoring via Pulse Transit Time: Theory and Practice,” IEEE Trans. Biomed. Eng., vol. 62, no. 8, pp. 1879–1901, Aug. 2015.

[6] J. R. Womersley, “Method for the calculation of velocity, rate of flow and viscous drag in arteries when the pressure gradient is known.,” J. Physiol., vol. 127, no. 3, pp. 553–63, Mar. 1955.

[7] C. Stefanadis, “Pressure-diameter relation of the human aorta. A new method of determination by the application of a special ultrasonic dimension catheter.,” Circulation, vol. 92, no. 8, pp. 2210–9, Oct. 1995.

[8] Qing Liu, B. P. Yan, Cheuk-Man Yu, Yuan-Ting Zhang, and C. C. Y. Poon, “Attenuation of Systolic Blood Pressure and Pulse Transit Time Hysteresis During Exercise and Recovery in Cardiovascular Patients,” IEEE Trans. Biomed. Eng., vol. 61, no. 2, pp. 346–352, Feb. 2014.

[9] D. H. Bergel, “The dynamic elastic properties of the arterial wall.,” J. Physiol.,

vol. 156, no. 3, pp. 458–69, May 1961.

[10] B. M. Learoyd and M. G. Taylor, “Alterations with age in the viscoelastic properties of human arterial walls.,” Circ. Res., vol. 18, no. 3, pp. 278–92, Mar. 1966.

[11] R. Mukkamala, “Towards Ubiquitous Blood Pressure Monitoring via Pulse Transit Time: Theory and Practice,” IEEE Trans Biomed Eng., vol. 62, no. 8, pp. 1879–1901, Aug. 2015.

[12] D. Finlay, D. Guldenring, G. Janjua, and J. McLaughlin, “Independent measurement of high blood pressure changes in cuff-less blood pressure monitoring,” J. Electrocardiol., vol. 50, no. 6, p. 866, Nov. 2017.

Chapter 6

Conclusion and Future work

6.1 Conclusion

This study compared and validated a novel, non-invasive sensing system for the assessment of arterial stiffness, an indicator of hypertension, and has contributed significantly towards improving the conventional techniques for cuffless BP estimation used for early detection of hypertension. Furthermore, this study verified and highlighted the advantages of mechanical sensing for the arterial distension waveform, demonstrating that BPP is superior to the current state-of-the-art optical PPG assessment of arterial waveforms. This study also explored pathways for collating a novel, state-of-the-art dataset that simultaneously captured various modalities of the arterial waveform signals, such as PPG, BPP, SPH, and ECG. The BPP and PPG arterial waveforms were compared and validated against various gold-standard waveforms and techniques. 1) HRV techniques, precursor to hypertension, were used to compare the arterial waveforms, to determine their trackability and responsiveness in the arterial tree and were validated against ECG waveforms. 2) The spatial-temporal indexes, predictor of hypertension, of arterial waveforms were used to compare waveform morphologies and were validated against the SPH waveform. 3) The inter- and intra-methodology comparisons of PTT measurements were used to compare the consistency and stability of using arterial waveforms for arterial stiffness measurements. Finally, 4) The fusion of PPG and BPP waveforms was tested, using phase-lag and PU-loop techniques, which were validated against the SphygmoCor aortic AIx.

This study developed a novel acquisition platform, which was able to integrate various state-of-the-art sensors, for the simultaneous acquisition of arterial waveforms with different morphologies, such as the PVDF sensor system (using the BPP sensor) to obtain a BPP waveform, an SPH device to obtain the arterial tonometric waveform, and a PPG sensor, to obtain a volumetric flow waveform, using the Biopac MP36R research platform. This study developed a processing algorithm, to eliminate artefacts

and unknowns associated with processing, during the comparison of and validation of arterial waveforms, which may be unavoidable if different software is used.

One of the key advantages of the BPP sensing technique is that it is not influenced by blood rheology and/or changes in blood rheology, compared with conventional techniques, such as PPG. In addition, BPP operates independently of the subject's skin colour and is free from artefacts caused by for example, the use of cosmetics, unlike the PPG sensor. These advantages make BPP more appropriate method for the assessment of arterial waveforms compared with PPG.

The BPP sensor can be used as a surrogate for the gold standard for HRV, ECG R-peak, during the assessment of the HRV. The peak of the first derivative and the peak of the second derivative of the PPG and BPP waveforms showed satisfactory accuracies (r^2 >0.9) compared with the ECG R-peak HRV parameters. The peak of the second derivative of the BPP arterial waveforms proved to be the most resilient against arterial tree artefacts, with the highest *'r^2'* value when correlated with the ECG R-peak for HRV. This result established the trackability and responsiveness of BPP arterial waveforms, which can produce a similar efficiency and performance for the measurement of HRV parameters against the gold-standard ECG waveform. The fiducial point on the BPP arterial waveform did not alter haemodynamic parameters in response to artefacts from the arterial tree.

The BPP sensor can be used as a low-cost, tonometer, prognosticator of hypertension, alternative because the BPP waveform showed high accuracy for the assessment of arterial indexes, including the SI, RI, AI, AIx, EI, EEI, and DRI, compared with PPG waveform indexes, which were validated against the SPH tonometric waveform indexes. The dicrotic notch plays a vital role in the assessment of these indexes, which were not present in the PPG arterial waveforms. In contrast, the BPP-sensed waveform was successfully able to capture the dicrotic notch in all the subjects in the study. The use of the 4-element WK personalised transfer function on the BPP waveform increased the accuracy of the indexes to 98% compared with the SPH tonometric waveform indexes. Additionally, the BPP sensor is an operator-less, lightweight, wearable, and low-cost sensor that can be used for the accurate assessment of arterial stiffness, as a low-cost alternative to tonometric devices.

Novel inter- and intra-group comparisons of PTT were performed between inline BPP sensors and inline PPG sensors. This study is the first to compare methodologies for the detection of the arterial waveform. The BPP waveforms showed an improved consistency and stability for PTT measurements on the arterial branch compared with the PPG waveforms. PTT-BPP showed higher transit time values compared with PTT-PPG, with an average mean value of 11.5 milliseconds. The ANOVA identified a significant difference between PTT-PPG and PTT-BPP values, which supports and verifies the comparisons among the spatial-temporal indexes. The higher consistency of PTT-BPP may improve BP estimation accuracy, which can help to independently predict sudden changes in BP measurements.

Finally, the fusion between the BPP and PPG waveform was examined, producing a PU-loop and a phase-lag measurement between the waveforms, which was validated against the SPH carotid AIx. The phase-lag between the BPP and PPG waveforms is highly correlated with the SPH carotid AIx, which has great prognostic value. The fusion method resulted in the development of a novel, single-location, non-invasive arterial stiffness assessment method, which has enormous potential for the future development of compact wearable devices for early detection of hypertension.

6.2 Future Directions

This work can be further improved and would be beneficial for designing emerging and novel devices in the future for prognosis of hypertension. The following recommendations are based on the experience gained during this research study.

1- Motion artefact removal would be the most attractive research area, which is necessary to make the PVDF piezoelectric sensor truly wearable. Enormous research is focused on motion artefact removal for the PPG waveform [1], which can also be applied to the BPP waveform.
2- The personal or general adaptive tracking function has been the focus of research, due to the dynamic nature of BP waveforms, as reported by Mukkamala et al. [2], and has the potential to transform the PVDF piezoelectric sensor into a tonometric device that can dynamically track haemodynamic parameters related to hypertension.
3- The quantisation of the PVDF piezoelectric sensor would provide insights into BP variations, in mmHg, which would add value to the morphological waveform.

4- The comparison between hypertensive subjects and same-aged healthy subjects may improve the stratification between these two categories.
5- BPP waveform validation, using BP intervention techniques, such as the Valsalva and Muller's manoeuvres, have the potential to improve estimates of dynamic BP changes in hypertensive subjects [2].

6.3 References

[1] F. Peng, Z. Zhang, X. Gou, H. Liu, and W. Wang, “Motion artifact removal from photoplethysmographic signals by combining temporally constrained independent component analysis and adaptive filter,” *Biomed. Eng. Online*, vol. 13, p. 50, Apr. 2014.

[2] R. Mukkamala, “Toward Ubiquitous Blood Pressure Monitoring via Pulse Transit Time: Theory and Practice,” IEEE Trans. Biomed. Eng., vol. 62, no. 8, pp. 1879–1901, Aug. 2015.

Appendix A

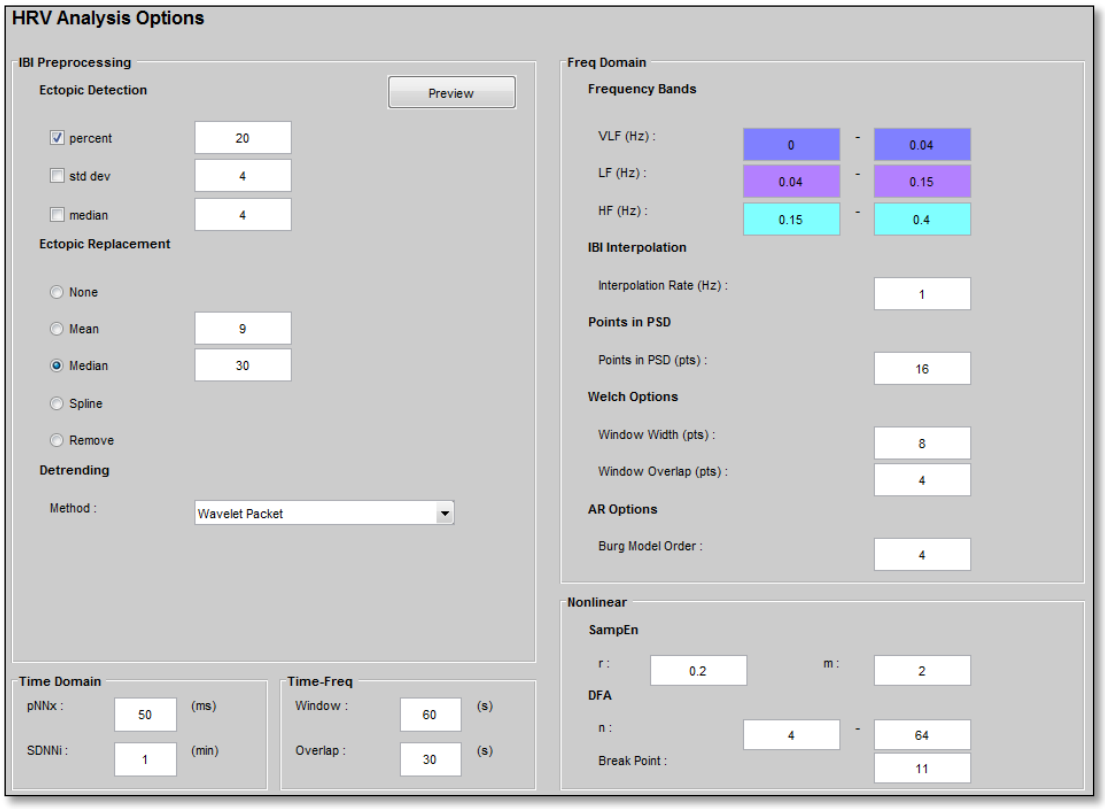

Figure 5.1A: Parameter setting of HRVAS

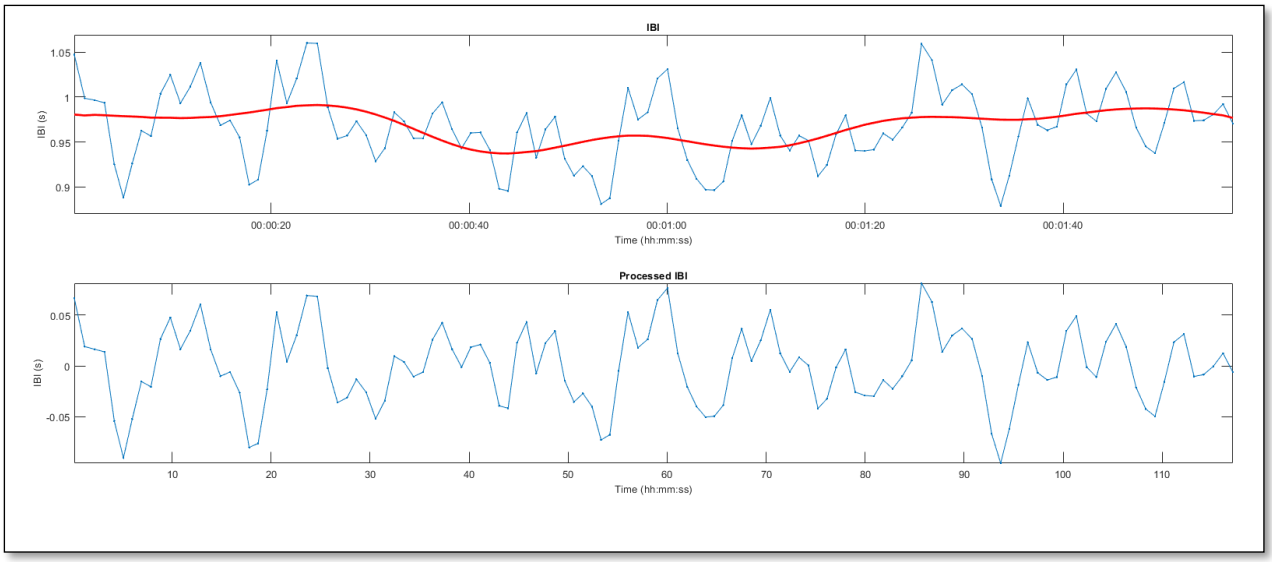

Figure 5.2A: Baseline removal in beat-to-beat interval of the subject 3

Time Domain

Variable	Units	Value
MeanIBI	(ms)	966.9
SDNN	(ms)	40.6
MeanHR	(bpm)	62.2
SDHR	(bpm)	2.6
RMSSD	ms	32.3
NNx	(count)	11
pNNx	(%)	9.1
SDNNi	(ms)	684.0
Geometric Measures		
HRV Triangular Index		12.2
TINN	(ms)	169.7

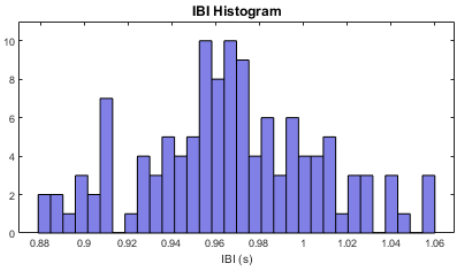

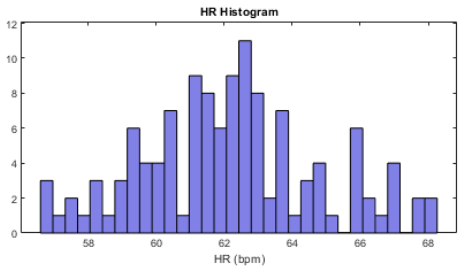

Figure 5.3A: The parameters for HRV in the time domain

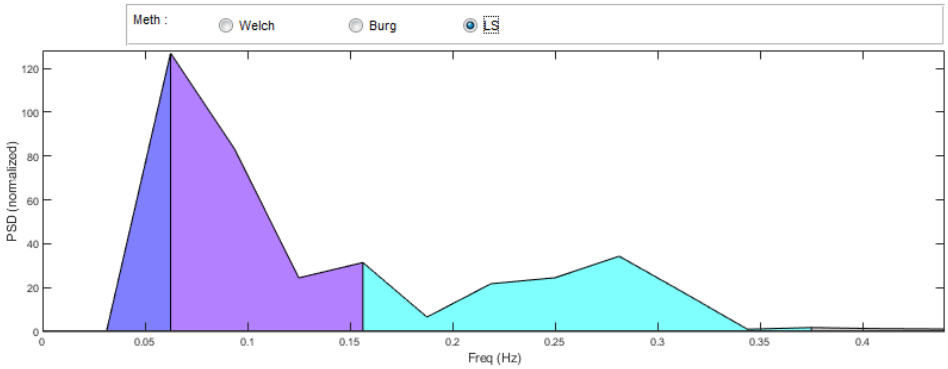

Frequency Band	Peak (Hz)	Power (ms^2)	Power (%)	Power (n.u.)	LF/HF (ratio)
Welch PSD					
VLF	0.03	123.4	13.6		0.734
LF	0.06	332.9	36.6	0.423	
HF	0.16	453.5	49.8	0.577	
Burg PSD					
VLF	0.03	25.6	6.2		1.962
LF	0.10	256.2	62.1	0.662	
HF	0.29	130.6	31.7	0.338	
Lomb-Scargle PSD (norm)					
VLF	0.03	0.0	0.0		1.298
LF	0.06	0.0	56.5	0.565	
HF	0.28	0.0	43.5	0.435	

Figure 5.4A: The parameter of HRV in the frequency domain

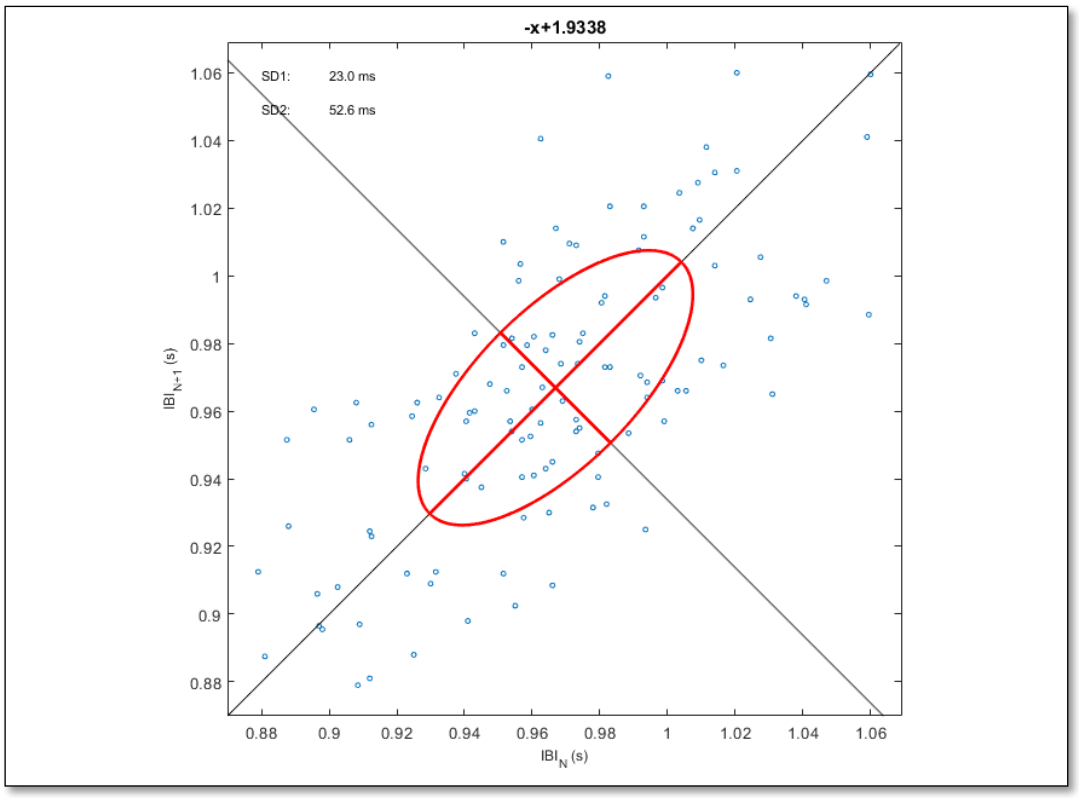

Figure 5.5A: The Poincare plot of HRV

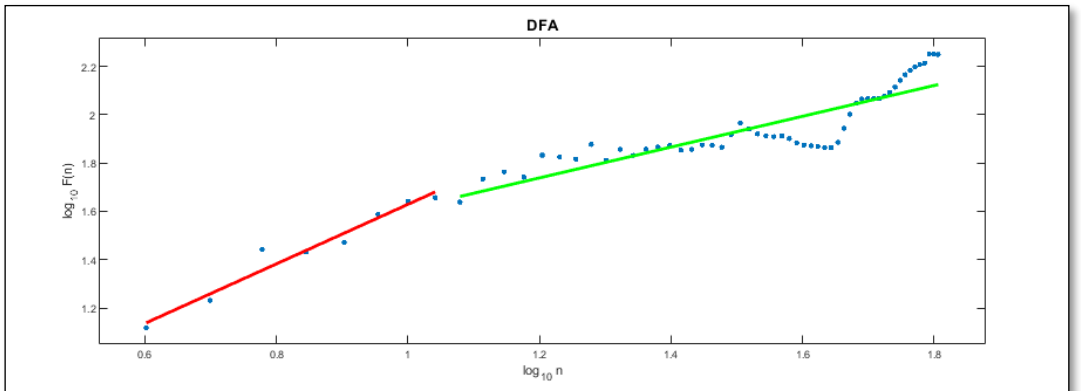

Nonlinear Statistics

Variable	Units	Value
Entropy		
SampEn	-	1.980
DFA		
α_{all}	-	0.714
α_1	-	1.232
α_2	-	0.637

Figure 5.6A: The HRV parameter in the nonlinear domain

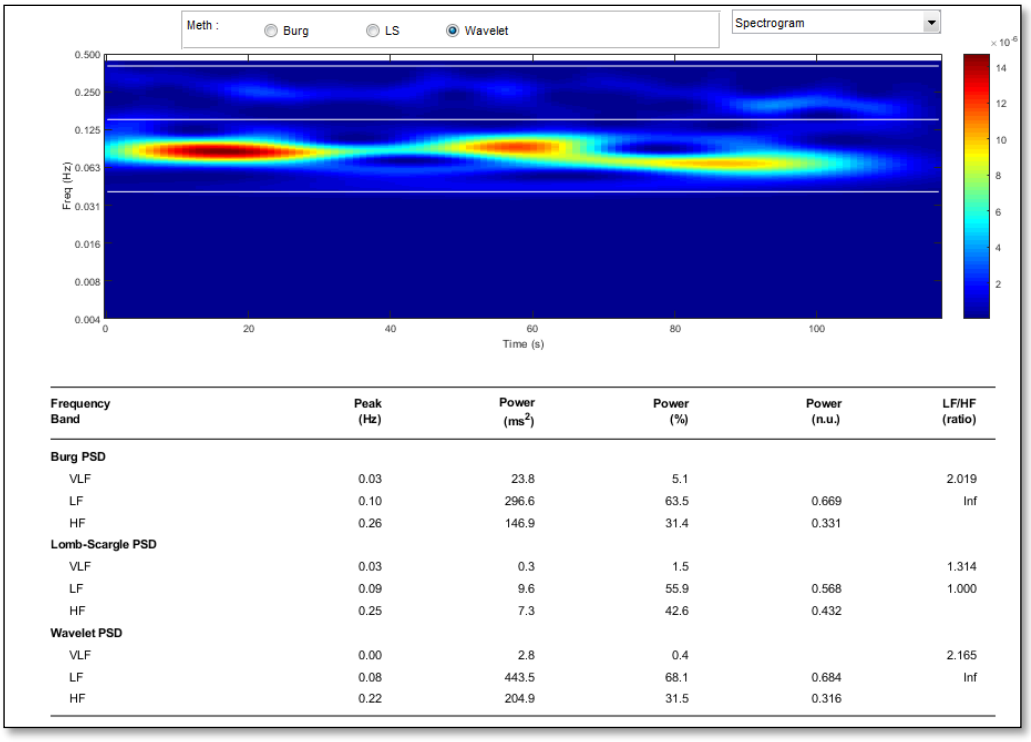

Frequency Band	Peak (Hz)	Power (ms^2)	Power (%)	Power (n.u.)	LF/HF (ratio)
Burg PSD					
VLF	0.03	23.8	5.1		2.019
LF	0.10	296.6	63.5	0.669	Inf
HF	0.26	146.9	31.4	0.331	
Lomb-Scargle PSD					
VLF	0.03	0.3	1.5		1.314
LF	0.09	9.6	55.9	0.568	1.000
HF	0.25	7.3	42.6	0.432	
Wavelet PSD					
VLF	0.00	2.8	0.4		2.165
LF	0.08	443.5	68.1	0.684	Inf
HF	0.22	204.9	31.5	0.316	

o

Figure 5.7A: The HRV analysis in the frequency domain based on different PSD